Title

Magnetic Reconnection on the Earth's Magnetopause: Identification, Magnetic Flux Transport and Magnetic Entanglement

Permalink

https://escholarship.org/uc/item/0c87m9vm

Author

Qi, Yi

Publication Date

2021

Peer reviewed|Thesis/dissertation

UNIVERSITY OF CALIFORNIA

Los Angeles

Magnetic Reconnection on the Earth's Magnetopause:

Identification, Magnetic Flux Transport and Magnetic Entanglement

A dissertation submitted in partial satisfaction

of the requirements for the degree

Doctor of Philosophy in Geophysics and Space Physics

by

Yi Qi

2021

ABSTRACT OF THE DISSERTATION

Magnetic Reconnection on the Earth's Magnetopause:

Identification, Magnetic Flux Transport and Magnetic Entanglement

by

Yi Qi

Doctor of Philosophy in Geophysics and Space Physics

University of California, Los Angeles, 2021

Professor Christopher Russell, Chair

Magnetic reconnection is a fundamental physical process that happens between anti-parallel magnetic field components. This process is ubiquitous and can be found in both laboratory and space plasma. At the same time, it modifies the field topology and converts energy explosively from field to plasma. With its universality and capability, magnetic reconnection has been an important subject for decades, and with improving observation/modeling techniques, we are able to keep advancing our knowledge on this topic.

In this dissertation we utilize in-situ measurements from the Magnetospheric Multiscale (MMS) and numeric modeling. We first investigate the heart of magnetic reconnection, the X-line. Then we focus on the Flux Transfer Events (FTEs) which are products of magnetic reconnection on the Earth's magnetopause and the interactions between flux ropes that carry the reconnected magnetic flux. We apply magnetic curvature analysis to the electron diffusion region (EDR) crossings and x-line crossings. We find highly increased magnetic curvature. The radius of curvature can decrease to the order of electron gyro-radius, which is consistent with the small scale nature of the center of magnetic reconnection. Another essential property of magnetic reconnection is the magnetic flux transport during the annihilation and reformation of magnetic field lines. We develop a new method to quantitatively describe the magnetic flux transport (MFT) characteristics and test it in both simulations

and observations. We find bidirectional Alfvenic inflow and outflow of magnetic flux in a specially limited region around the X-line. This transport pattern defines reconnection and produces a new quadrupolar pattern in the divergence of the magnetic flux transport velocity. As the reconnected magnetic flux is carried away from the initial reconnection site in the FTE, we discover magnetic entanglement and new pairs of flux ropes are born through the disentanglement enabled by the reconnection between two entangled flux tubes. We further identify three temporal evolutionary stages of magnetic entanglement. Three-dimensional Hall Magnetohydrodynamic (MHD) simulation verifies the feasibility of this process and shows it is mainly driven by the momentum of the ambient converging plasma.

The dissertation of Yi Qi is approved.

Marco Velli

Jacob Bortnik

Raymond Walker

Christopher Russell, Committee Chair

University of California, Los Angeles

2021

In dedication to my parents

TABLE OF CONTENTS

LIST OF FIGURES

List of Tables

ACKNOWLEDGEMENTS

Dylan Dempster, as well as graduate students of my same year, including Colin Wilkins, Fekireselassie Beyene, Ashley Schoenfeld, and my officemate Dr. Emily Hawkins for their help in my research and my life here as an international student.

I have received a lot of support from scientists in the MMS and HERMES community, including Dr. Jason Shuster, Dr. Rungployphan Kieokaew, Dr. Yu Lin, Dr. Shan Wang, Dr. Li-jen Chen, and Dr. Yi-Hsin Liu. They selflessly shared what they know when I asked them questions and offered me great opportunities to advertise my work during workshops and conferences.

I want to thank my parents, Zhiling Qi and Zhaohui Chen, for their love and support over the years. I also want to express my sincere thanks to my boyfriend, Erik Sonnenberg. He stood by my side when I faced challenges, comforted me when I had difficult times, and shared the joy with me when I made any progress, no matter how small it is. His love, understanding, and encouragement have helped me more than he himself recognized. I would like to thank my decade-old friends, Yao Fu, Jingying Peng, and Xuezi Li, as they believed in me and support me anytime, anywhere. It has been my luck to have all these people in my life.

Curriculum Vitae

2012 – 2016	B.S. in Space Physics, University of Science and Technology of China, Hefei, China.
2016 – Present	Ph.D. student in Geophysics and Space Physics, University of California, Los Angeles.

Publications

Jia, Y., **Qi, Y.**, Lu, S. & Russell, C. T., "Temporal evolution of flux rope/tube entanglement in 3-D Hall MHD simulations", J Geophys Res Space Phys, (2018) doi:10.1029/2020ja028698.

M. Hubbert, **Yi Qi**, C.T. Russell, J.L. Burch, B.L. Giles, T.E. Moore, "Electron-Only Tail Current Sheets and Their Temporal Evolution", Geophys Res Lett, (2021) doi:10.1029/2020gl091364

Qi, Y., Russell, C. T., Jia, Y.-D., & Hubbert, M., "Temporal Evolution of Flux Tube Entanglement at the Magnetopause as Observed by the MMS Satellites", Geophys Res Lett, (2020),, 47, e2020GL090314. https://doi.org/10.1029/2020GL090314

Tak Chu Li, Yi-Hsin Liu, & **Yi Qi**. "Identification of active reconnection x-points using magnetic flux transport in kinetic turbulent plasmas", Astrophysical J Lett 909, L28 (2021)

Yi Qi, Tak Chu Li, C.T. Russell, Ying-dong Jia, "Magnetic Flux Transport Identification of Active Reconnection: MMS Observation in the Earth's Magnetosphere ", Manuscript in preparation.

CHAPTER 1

Introduction

In this chapter we introduce the basic concepts associated with magnetic reconnection and Earth's magnetopause. In section 1.2, 1.1, and 1.3 we briefly review different regions and corresponding properties of the Earth's magnetosphere, together with the background of the Sun and the solar wind, and how solar wind interacts with the Earth's magnetosphere. In section 1.4 we review the frozen-in condition and the diffusion of magnetic field, the fluid model of magnetic reconnection and later theories on the kinetic aspect of magnetic reconnection. In section 1.5 we introduce the Magnetospheric Multiscale (MMS) mission and how it assists with targeting the reconnection problem. In section 1.6 we will overview the organization of the remaining part of this dissertation.

1.1   The Sun and the Solar Wind

The Sun, even though it may be a normal star, is the closest star to Earth and is able to be observed by us most clearly. The heat and light from the Sun have a significant impact on our living environment. More than that, despite the seemingly empty void between the Sun and planets in solar system, there are continuous flows of particles and magnetic flux spreading out from the Sun. They interact with the Earth and planets, becoming the most important external driver of magnetospheric dynamics. As these particles and field lines are extensions of the solar atmosphere, the particles' composition and distribution, the field lines' structure, and topology, are all associated with activity on the Sun and in the solar atmosphere.

Figure 1.1 shows the structure of the sun. The center of the Sun is the core where

nuclear reactions keep releasing energy. Outside the core, in the radiation zone, energy is transported outward by radiation. The outer layer of the solar interior is the convection zone, where energy is transported outward through convection currents.
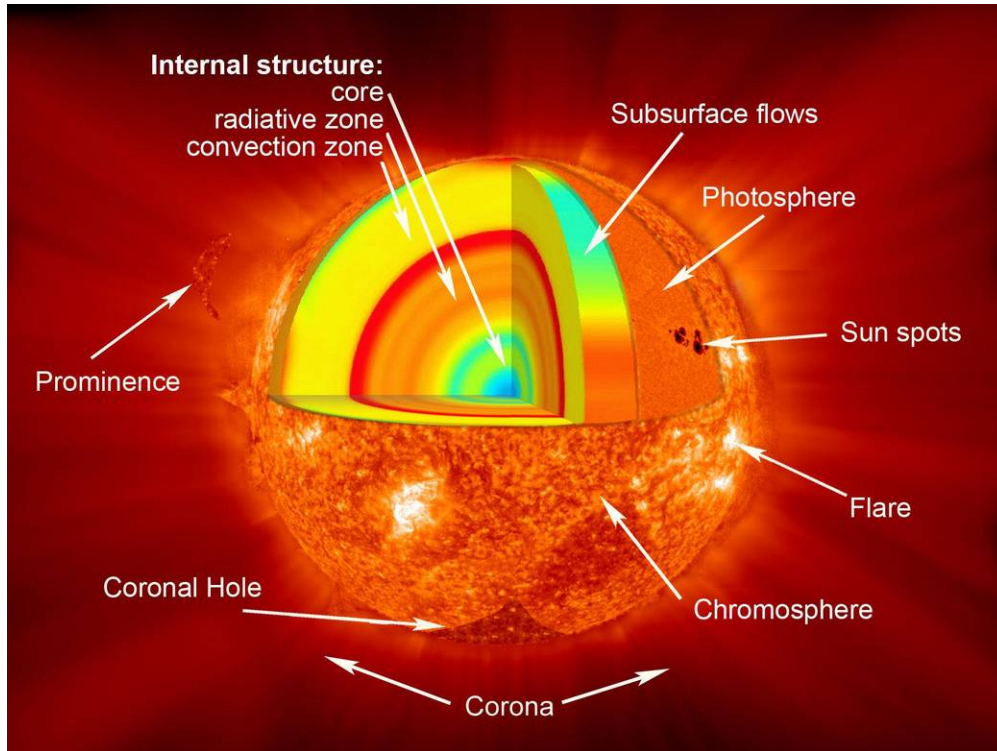
Figure 1.1: The structure of the Sun. Image from: NASA

Outside the convection zone this outward flow becomes solar atmosphere. The bottom of the solar atmosphere is a thin layer known as the photosphere. Granules and super granules caused by the motion in the convection zone can be seen at this height. The center of granules consists of hotter rising plasma, and the edge are cooler descending plasma. The photosphere is obove the chromosphere. In this layer, temperature rises with height. The outer layer is the solar corona. Its temperature increases sharply compared to the chromosphere through a transition region, and the plasma density decreases at the same time. The solar corona can be seen during a total solar eclipse or through a coronagraph which can block the sun as the moon does during the eclipse. As shown in Figure 1.2 there are regions of arching magnetic flux tubes forming helmet streamers and pseudo helmet streamers, as well as regions where field lines are "open" which are known as coronal holes.

Figure 1.2: A photo of the solar corona taken during the total eclipse on Aug. 21, 2017. Image from SciTechDaily

Beyond the solar corona is the solar wind, which is the extension of the corona and is accelerated to be supersonic. Solar wind originating from the streamers is denser and tends to flow relatively slowly at around $250 - 450 \ km \ s^{-1}$, while solar wind coming from the open field line region is tenuous and moves faster at around $500 - 800 \ km \ s^{-1}$ (Cranmer & Winebarger, 2019). Magnetic field lines also stretch out. The rotation of the sun itself gives the Interplanetary Magnetic Field (IMF) a spiral geometry, and the fast stream solar wind will eventually catch up with the slow stream, generating Corotating Interaction Regions (CIR).

Figure 1.3 gives a sketch of CIRs and the profile of several solar wind parameters along a circle with radius of R in the solar equatorial plane. Crossing a CIR from slow stream to
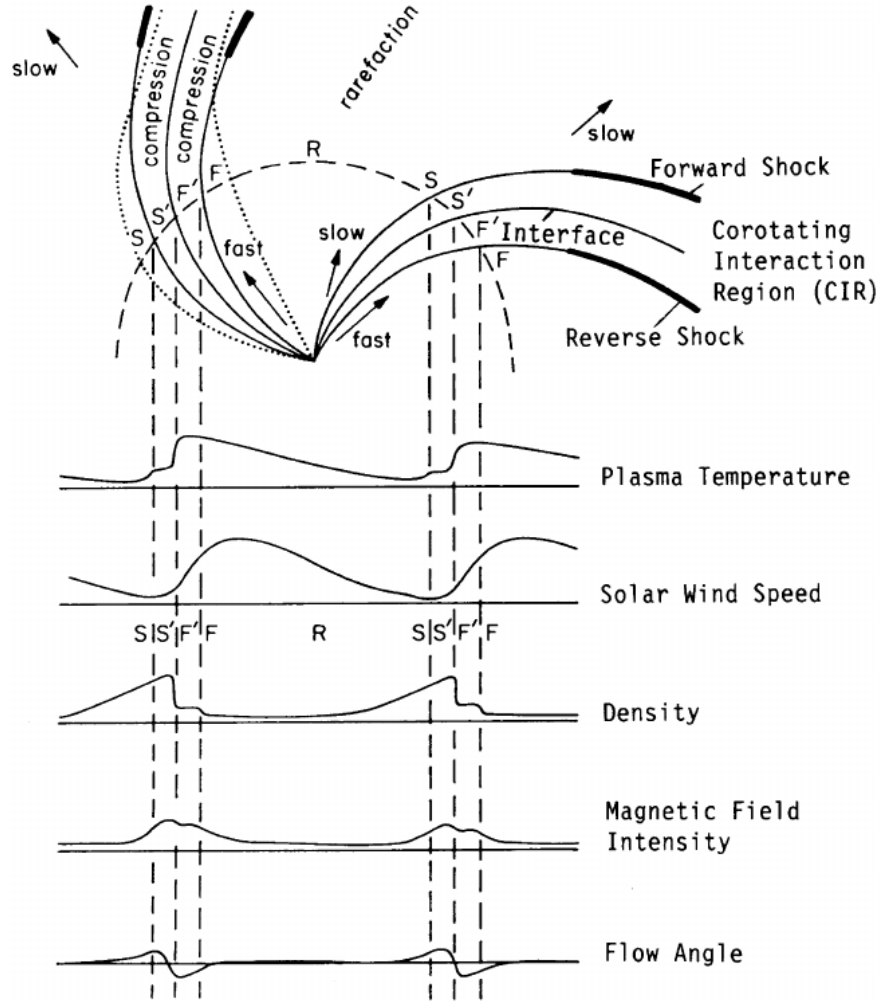
Figure 1.3: The sketch of the Corotating Interaction Regions and the variations in the solar wind parameters including: plasma temperature, solar wind speed, density, magnetic field intensity and flow angle. Figure from Richardson (2004)

fast stream, the magnetic field intensity is built up at the stream interface indicating the compression of the flows originating from different regions on the Sun. Consistent with this, the plasma temperature rises while the density drops.

In addition to the flow velocity, fast and slow solar wind also differ in plasma and magnetic field properties. Considering that the slow wind is associated with helmet streamers in the corona and at the edge of coronal holes, the plasma composition also resembles the solar corona. Since the fast wind comes from the center of opened coronal holes, its composition

4

Property	Fast solar wind	Slow solar wind
Density at 1 AU	$\sim$ 1–7 cm^{-3}	$\sim$ 7–15 cm^{-3}
Proton temperatures	$\sim 2 \times 10^5$ K	$\sim 4 \times 10^4$ K
Electron temperatures	$\sim 1 \times 10^5$ K	$\sim 1 \times 10^5$ K
Composition	higher He^{++} ($\sim$ 4%)	higher O^{+7}/O^{+6}, Fe/O
Field structure	Alfven waves	current sheet(s), rotational discontinuity

Table 1.1: Fast and slow solar-wind properties. Adapted from Russell et al. (2016)

is more like Sun's photosphere. Table 5.1 from Russell et al. (2016) compares and records the differences clearly:

There are more structures in the solar wind that are of great importance and in which we are interested. One example is the Heliospheric Current Sheet (HCS), which is the boundary encircling the Sun that separates oppositely directed magnetic fields that originate on the Sun and are "open" (Smith, 2001). The heliospheric current sheet separate sectors in which the interplanetary magnetic fields alternate between inward and outward. Crossing this boundary, the signs of the radial and azimuthal field components change from positive to negative or negative to positive. At the heliospheric current sheet the proton density is high while the speed, proton temperature, and helium-proton ratio are low compared with the ambient plasma. The increased plasma density and decreased magnetic field give an increase in plasma β, defined as the ratio of the plasma thermal pressure ($P_{ther} = nkT$, where n is the plasma number density, k is the Boltzmann constant, and T is the plasma temperature) to magnetic pressure ($P_B = B^2/(2\rho\mu_0)$), where B is the magnitude of the magnetic field, ρ is the plasma density, and μ_0 is the vacuum magnetic permeability).

Another example of large scale structures in the solar wind that can cause strong space weather effects on the Earth is the Coronal Mass Ejection (CME) or Interplanetary Coronal Mass Ejection (ICME). Sudden and explosive energy releases occur on the Sun and expel

plasma together with magnetic field into the heliosphere. The outward moving magnetic field lines usually wind into a rope like structure, i.e. a flux rope. Plasma carried away with the magnetic field mainly comes from the corona, but can also involve transport from the lower altitudes such as the chromosphere and photosphere where the plasma can be cooler and denser (Webb & Howard, 2012). White-light observations of CMEs usually show classic "three-part" structure (Illing & Hundhausen, 1985). In-situ observations of ICMEs also inspire a model of an outward moving magnetic cloud with a sheath region and shock in its front.

1.2   The Terrestrial Magnetosphere

Earth has an intrinsic magnetic field and the terrestrial magnetosphere is like a bubble surrounding Earth where the geomagnetic field dominates the interplanetary field.

Earth's intrinsic magnetic field is approximately a magnetic dipole (example shown in panel (a) of Figure 1.5). The dipole moment is about $0.30 \times 10^{-4} T \cdot R_E{}^3$ and is tilted slightly relative to the Earth's rotation axis. This dipole moment produces a magnetic field strength at the equator on the Earth's surface of about 30,000 nT, and at 10 Earth radii, of about 30 nT (Russell, 2000). However, the terrestrial magnetosphere has a much different shape than a dipole field. The solar wind blows against the magnetosphere, and the dayside magnetosphere is compressed, while the nightside is dragged away (as shown in panel (b) of Figure 1.5). As shown in the sketch, important regions in the magnetosphere include the magnetopause, polar cusp, magnetotail north and south lobe and plasma sheet.

The magnetopause is the interface where shocked solar wind interacts with the terrestrial magnetosphere. It is the outer boundary of magnetosphere. We will discuss the coupling between solar wind and magnetosphere in detail in the next section. Typically plasma is dense (~ 30 cm $^{-3}$) and cool (100 eV) on the magnetosheath side and is hot (~ 1 keV) and tenuous (~ 0.3 cm $^{-3}$) on the magnetospheric side (Walsh, 2017). At high latitudes there is a small region called polar cusp. In this region the field lines are opened by magnetic reconnection
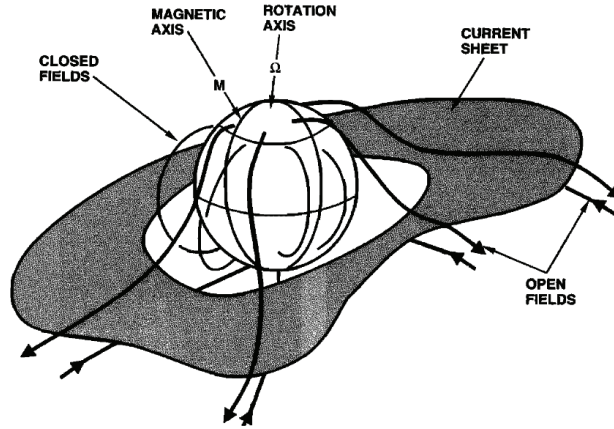
(a) sketch of Heliospheric Current Sheet
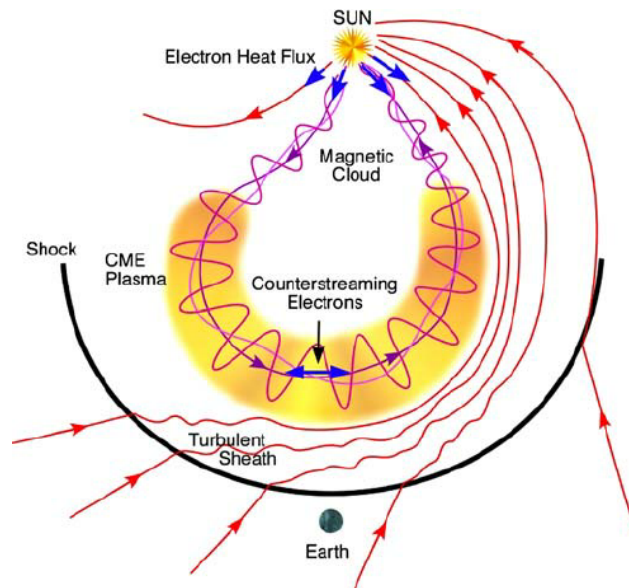
(b) sketch of Interplanetary Coronal Mass Ejection

Figure 1.4: panel a: figure from Smith (2001); Panel b: figure from Zurbuchen & Richardson (2005)

and enables the plasma originating in the magnetosheath to enter the ionosphere.

While the magnetopause on the dayside extends to about 10 Earth radii away, the magnetotail stretches out much further and could extend over 100 Earth Radii behind the Earth. In the magnetotail, there is a cross-tail current sheet flowing in the relatively hot plasma sheet. A boundary between the plasma sheet and the lobe is the Plasma-Sheet Boundary
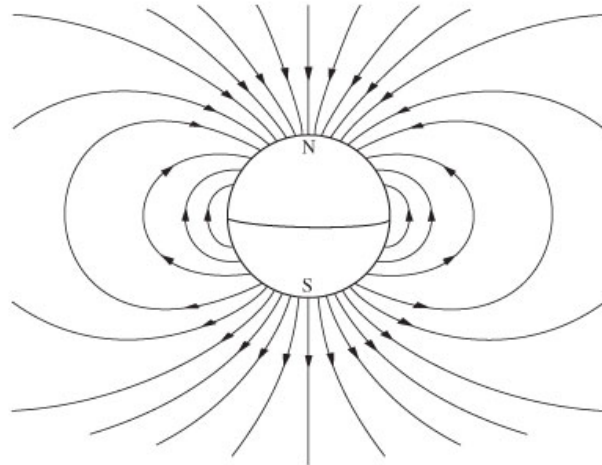
(a) Magnetic dipole
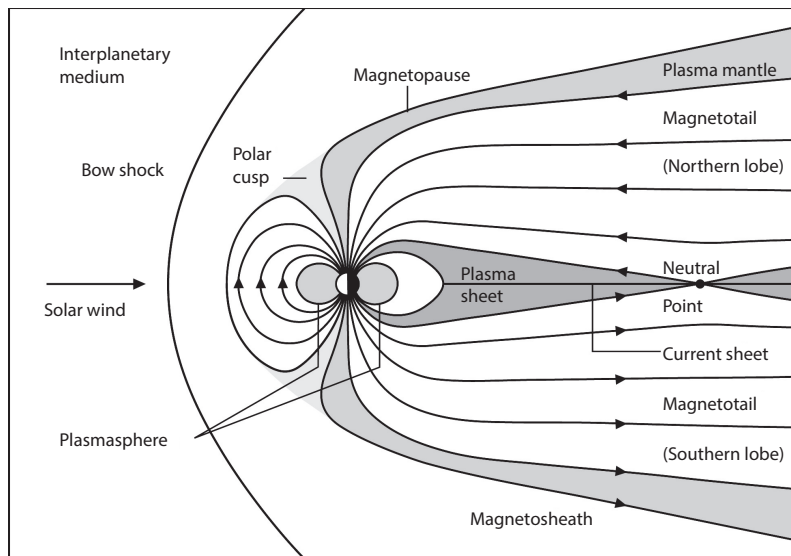
(b) The structure of the terrestrial magnetosphere

Figure 1.5: Panel a: Magnetic dipole. Image from New World Encyclopedia; Panel b: The structure of the terrestrial magnetosphere. Image from Russell et al. (2016)

Layer where counter streaming ion beams are usually observed. To the North of the plasma sheet, magnetic field lines are towards the Earth, and to the south, they point away from the Earth. The plasma density in the lobe is much thinner. Table 1.2 adapted from Kivelson & Russell (1995) summarizes the typical parameters in the tail region.

Properties	Tail Lobe	Plasma Sheet Boundary Layer	Central Plasma Sheet
Number density (cm^{-3})	0.01	0.1	0.3
Ion Temperature (eV)	300	1000	4200
Electron Temperature (eV)	50	150	600
Magnetic field strength (nT)	20	20	10
Plasma beta (β)	3×10^{-3}	10^{-1}	6

Table 1.2: Typical near-tail plasma and field parameters. adapted from Kivelson & Russell (1995)

1.3 Solar Wind and Magnetosphere Coupling

Even though we have learned the typical characteristics of the different regions in the terrestrial magnetosphere, it is important to realize that the magnetosphere is always changing and is always dynamic. The key external driver of these activities, the supersonic solar wind, comes from the Sun. It keeps blowing toward Earth, modifies the size and shape of the terrestrial magnetosphere with its varying plasma and magnetic field conditions.

The plasma that directly interacts with the terrestrial magnetosphere has different properties compared to plasma in the solar wind. The reason is that the solar wind flows faster than the velocity of the compressional wave so when it encounters the Earth, it cannot be diverted around the Earth without forming a steepened bow shock wave that alters the properties of the plasma and slows down the flow. Crossing the shock wave, plasma's dynamic pressure (nmU^2, where n is the number density, m is the mass and U is the bulk flow velocity) is transformed into thermal pressure (nkT, where k is the Boltzmann constant and T is the temperature). The slowed subsonic flow now can be diverted around the Earth.

The region downstream the bow shock is the magnetosheath which is hotter and denser,
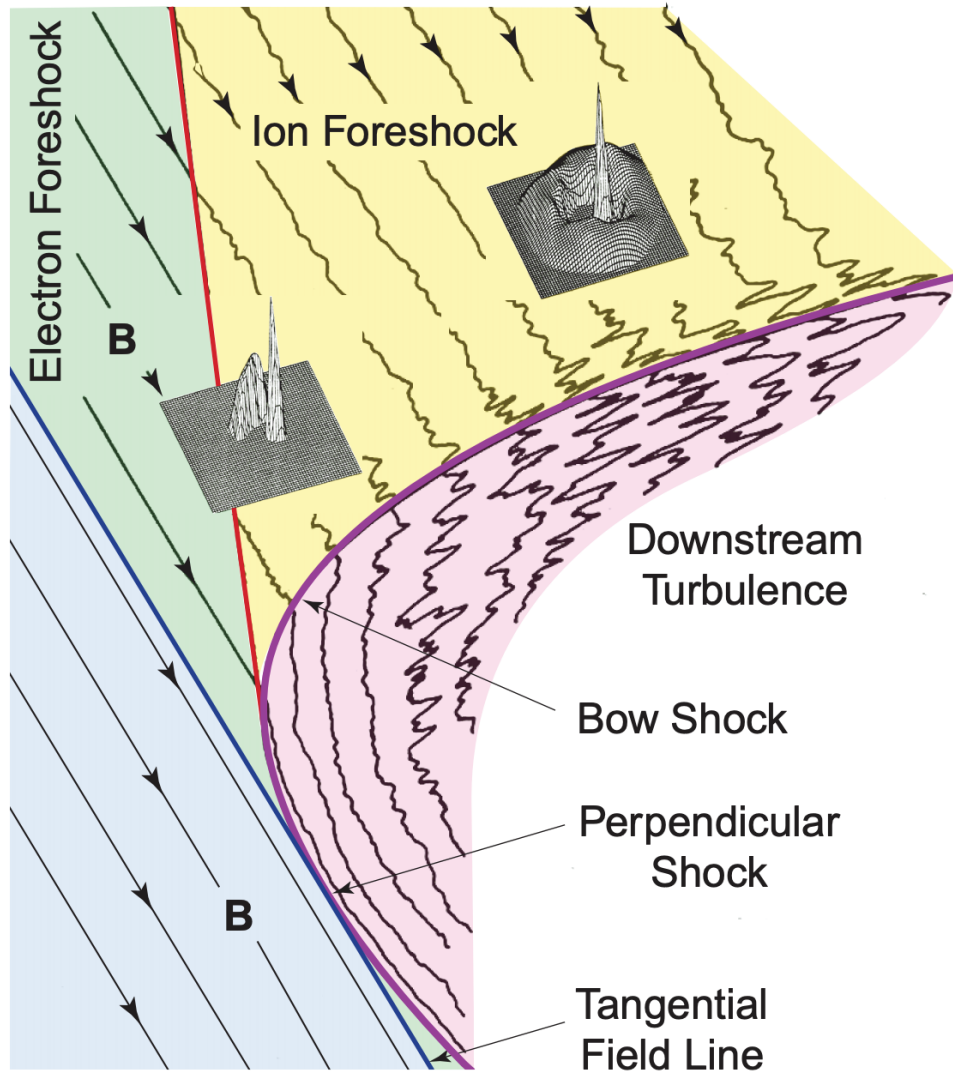
Figure 1.6: Schematic plot of quasi-parallel shock and quasi-perpendicular shock. Image from Eastwood et al. (2005)

usually turbulent. The shock parameters can be influenced by the shock Mach number (defined as the ratio of the solar wind speed to the speed of the compressional wave which in our case is the fast magnetosonic wave), and the IMF orientation. With a high Mach number the shock compresses the plasma more, and the orientation of the IMF determines whether it is a quasi-parallel (the angle between the field and the shock surface normal is within 45°) or a quasi-perpendicular shock (the angle between the field and the shock surface normal is larger 45°). A quasi-parallel shock is more complex than the quasi-perpendicular

shock. It can reflect the particles back into the solar wind and form a foreshock. In addition, downstream of a quasi-parallel shock is usually more turbulent compared to the downstream of a perpendicular shock.

Where the shocked solar wind interacts directly with the Earth's magnetosphere is the magnetopause. Magnetopause is a boundary that separates the dense (the order of 10 $\#/cm^3$) magnetosheath and the tenuous (the order of 1 $\#/cm^3$) magnetosphere. The plasma in the magnetosheath is colder (Te $\sim$ 10 eV, Ti $\sim$ 100 eV), while in the magnetosphere it's hotter (Te $\sim$ 100 eV, Ti $\sim$ 1000 eV). The temperature of a certain group of particle can vary based on their origin. The bulk flow velocity in also relatively faster and more turbulent before entering the magnetosphere.
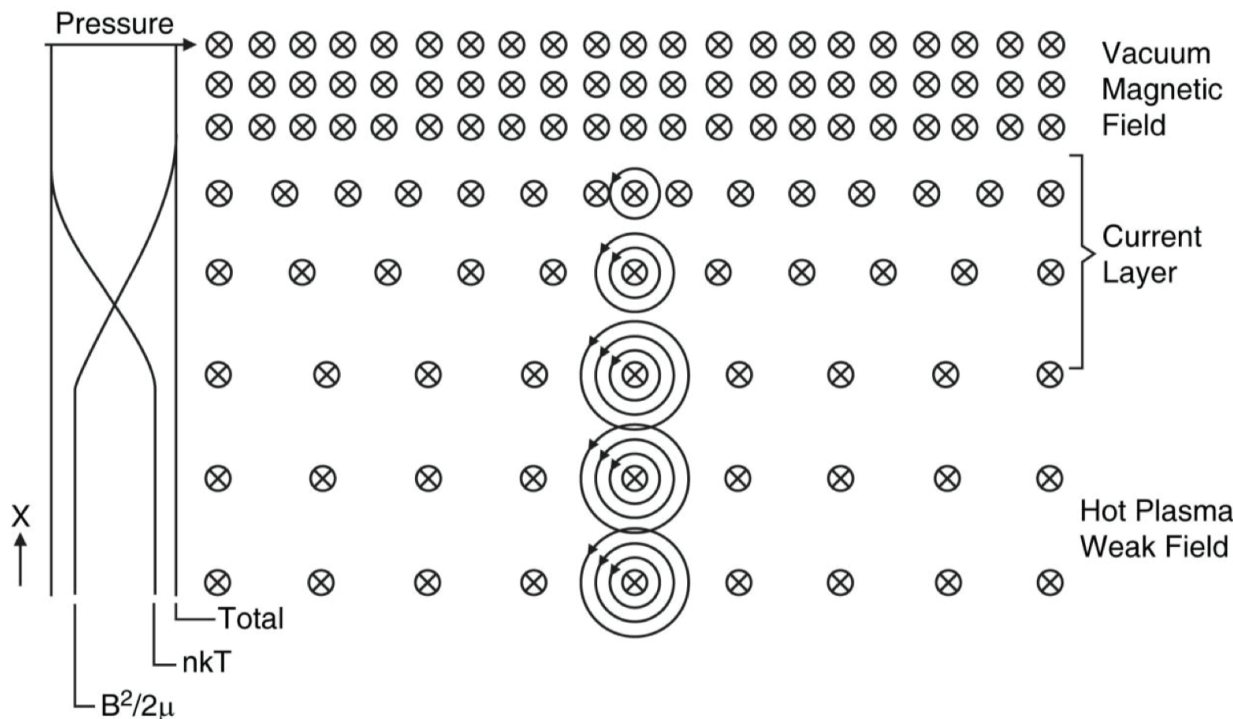
Figure 1.7: The pressure balance and current formation at the magnetopause. Image from Russell et al. (2016)

The nose of the magnetopause usually sits at around 10 R_E from Earth. This distance will be shorter if the solar wind dynamic pressure is stronger and compresses the magnetosphere

harder. As we have introduced in 1.2, Earth's intrinsic magnetic field is about 30nT at this location and points northward. The magnetic field in the magnetosheath does not have a constant orientation and is weaker than the magnetospheric field strength. Thus crossing the magnetopause from the magnetosheath side to the magnetosphere side, the plasma thermal pressure decreases mainly due to the decreasing number density, and the magnetic pressure increases with enhanced field strength. This gradient of the field strength results in smaller gyro-radii of the particles which eventually leads to the separation between particles and the formation of a current flowing from dawn side to dusk side. The total pressure which is a sum of the plasma thermal pressure and magnetic pressure remains constant under most circumstances, as shown in Figure 1.7.

The magnetopause is not always this quiet. When magnetic field lines of opposite direction contact with each other, magnetic reconnection can happen and change the connectivity of the field lines. During this process not only the magnetic field geometry changes, but the magnetic energy is also converted and used to heat or accelerate particles. Magnetic reconnection was first proposed to explain the explosive energy conversion and bursty momentum transport during solar flare and similar events. We will explain the model and basic concepts of magnetic reconnection in detail in the following section. One important application of this model is to explain the circulation of the plasma in the magnetosphere. This circulation has been discovered in early aurora research that found features in the polar cap that flowed in an anti-sunward pattern with consistent magnetic fields disturbances in the auroral zone. A picture of the global magnetic convection enabled by magnetic reconnection was first drawn by J. W. Dungey (Dungey, 1961), as shown in Figure 1.8

When solar wind is southward like in panel (a) of Figure 1.8, magnetic reconnection happens at low latitude dayside magnetopause. Newly reconnected and opened field lines are dragged towards magnetotail and the foot points of these field lines will move anti-sunward in the polar cap. These field lines will add to the tail lobe and eventually reconnection in the tail neutral sheet takes place to release some of the accumulated flux on the tail side and add closed field lines toward the earth. These closed field lines are transported towards

Interplanetary Field Southward
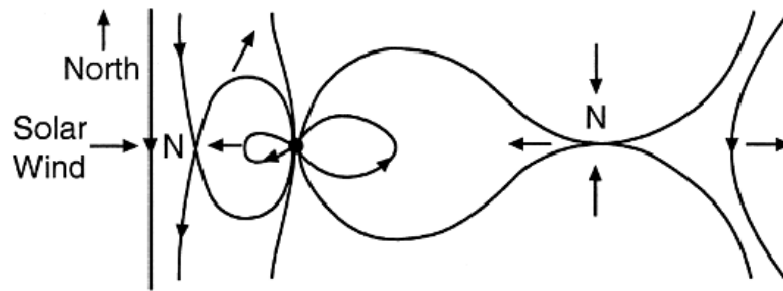
(a)

Interplanetary Field Northward
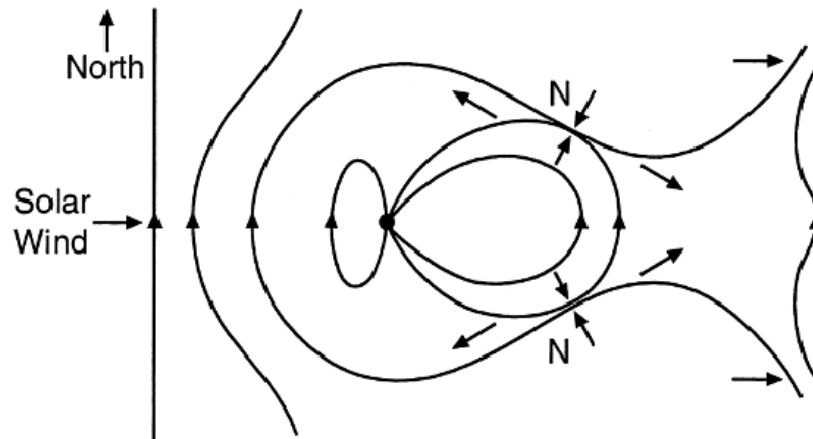
(b)

Figure 1.8: Sketch of Dungey Cycle under different IMF orientations; image from Nishida et al. (2009) after Dungey (1961)

the earth and dipolarized as they approach the earth. On the other hand, when the solar wind is due northward, it is hard to have magnetic reconnection in low-latitude areas at the dayside magnetopause, instead like demonstrated in panel (b) of Figure 1.8, magnetic reconnection takes place at higher latitudes at nightside which enables less magnetic flux from the solar wind enter the terrestrial magnetosphere and accordingly cause weaker geomagnetic

responses.

1.4 Magnetic Reconnection

Before we start to discuss magnetic reconnection, there are a couple of basic concepts we would like to review.

First, a magnetic field line, which is a curve that is tangential to the magnetic field $B_i(x_k)$ everywhere, can be described as:

$$\frac{dx_i}{ds} = \frac{B_i}{B}, \tag{1.1}$$

where ds is the length of the arc along the field, and B is the strength of the magnetic field. A single magnetic field line does not have end. But if there is another field line that is anti-parallel to it, there is a chance that these two magnetic field lines may "break".

The temporal variation of magnetic field can be described by Faraday's law and Ampere's law:

$$\frac{\partial \mathbf{B}}{\partial t} = -\nabla \times \mathbf{E} \tag{1.2}$$

Replace the Electric field $\mathbf{E}$ with the current density $\mathbf{J}$ using Ohm's law $\mathbf{J} = \sigma_0(\mathbf{E} + \mathbf{U} \times \mathbf{B})$:

$$\frac{\partial \mathbf{B}}{\partial t} = \nabla \times (\mathbf{U} \times \mathbf{B} - \frac{1}{\sigma_0}\mathbf{J}), \tag{1.3}$$

where σ_0 is the conductivity of the plasma caused by coulomb or neutral collision. To eliminate the current density $\mathbf{J}$ in the equation 1.3, consider Ampere's law:

$$\nabla \times \mathbf{B} = \mu_0(\mathbf{J} + \epsilon_0\frac{\partial \mathbf{E}}{\partial t}), \tag{1.4}$$

where μ_0 is the vacuum permeability. Take the curl of equation 1.4, noting that $\nabla \cdot \mathbf{B} = 0$, and replace the $\mathbf{J}$ in equation 1.3. We can ignore the term with $\partial \mathbf{E}/\partial t$ because its effect is only negligible unless the process is relativistic. Then we have the induction equation:

$$\frac{\partial \mathbf{B}}{\partial t} = \nabla \times (\mathbf{U} \times \mathbf{B}) + \frac{1}{\sigma_0\mu_0}\nabla^2\mathbf{B} \tag{1.5}$$

14

The variation of magnetic field at a point can be describe as the combination of two parts: the convection, i.e. the motion of the plasma, which is represented by the first term on the right-hand side, and the diffusion which is represented by the second term on the right-hand side. The convection term varies on a timescale of $\tau_c = \mathcal{L}/\mathcal{U}$ and the diffusion term varies on a timescale of $\tau_d = \sigma_0\mu_0\mathcal{L}^2$. The $\mathcal{L}$ is the global length scale of magnetic field variation, and the $\mathcal{U}$ is the fluid velocity. The magnetic Reynolds number $\mathcal{R}_m$ is defined as:

$$\mathcal{R}_m \equiv \frac{\tau_d}{\tau_c} = \sigma_0\mu_0\mathcal{U}\mathcal{L} \tag{1.6}$$

When the magnetic Reynolds number is large, the convection term dominates. When magnetic Reynolds number is small, the diffusion term dominates. If we choose $\mathcal{U}$ to be the Alfven speed, the magnetic Reynolds number becomes the Lundquist number $\mathcal{S}$. And it is apparent that the spatial scale of the magnetic field variation will largely influence whether the system is dominated by convection or diffusion.

When convection term dominates and the diffusion term is negligible, the induction equation becomes:

$$\frac{\partial \mathbf{B}}{\partial t} = \nabla \times (\mathbf{U} \times \mathbf{B}) \tag{1.7}$$

The magnetic field is frozen to the plasma and the magnetic flux through a closed line which moves with the fluid will remain constant. Replace $\partial \mathbf{B}/\partial t$ with $\nabla \times \mathbf{E}$ (Faraday's law), equation 1.7 gives $\mathbf{E} + \mathbf{U} \times \mathbf{B} = 0$, i.e. frozen-in, or magnetized fluid moves at the velocity of $\mathbf{E} \times \mathbf{B}/B^2$.

The frozen-in condition is not always valid. When the fluid velocity $\mathbf{U}$ is zero or purely parallel to the magnetic field, or the curl of $\mathbf{U} \times \mathbf{B}$ becomes zero, the diffusion term is no longer negligible and the induction equation is now:

$$\frac{\partial \mathbf{B}}{\partial t} = \frac{1}{\sigma_0\mu_0}\nabla^2\mathbf{B} \tag{1.8}$$

Under this situation, the magnetic Reynolds number is much smaller than 1. Thus it is rational to expect the diffusion of magnetic field to likely happen at locations where magnetic field varies on a small spatial scale $\mathcal{L}$. For ions, when the frozen-in condition is violated, $\mathbf{E} + \mathbf{U}_i \times \mathbf{B} \neq 0$; and for electrons, when $\mathbf{E} + \mathbf{U}_e \times \mathbf{B} \neq 0$ they are no longer fully magnetized.

Consider magnetic field lines that are anti-parallel and move towards each other. When the magnetic Reynolds number becomes small at a point, magnetic diffusion takes place and the magnetic field annihilates forming a magnetic neutral point, also referred to as the X-point due to the geometry as shown in Figure 1.9. Magnetic reconnection reconstructs the field lines and thrusts the reconnected flux away from the X-point.
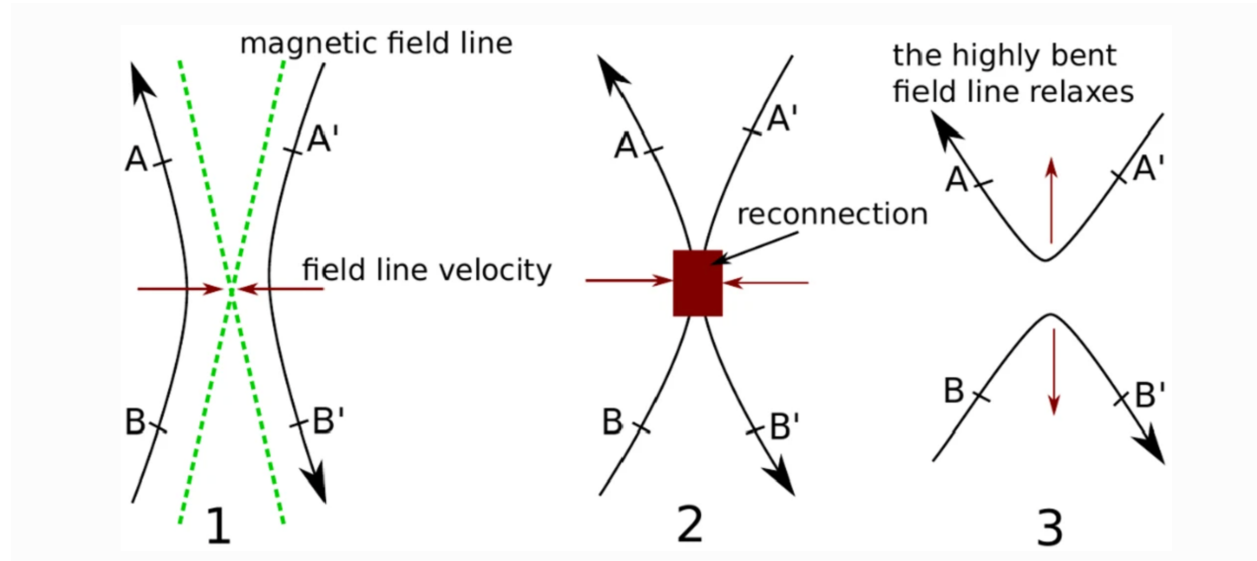
Figure 1.9: Anti-parallel field lines move toward each other and form a neutral point. Magnetic reconnection takes place. Image from Marcowith et al. (2020)

The earliest model of magnetic reconnection describes this process in the fluid frame and is known as Sweet-Parker reconnection (Parker, 1957; Sweet, 1958). It considered the conservation of mass, momentum, energy and magnetic flux that goes in and out of the X-point. A sketch of this model is shown in Figure 1.10. Thus there is a simple relation between ingoing magnetic field strength and outgoing magnetic field strength:

$$\frac{B_o}{B_i} = \frac{\delta}{L} \tag{1.9}$$

The reconnection rate, as can be seen from equation 1.9, is limited by the aspect ratio of the current sheet. To make this process faster a later model constrained the diffusion in a more localized region and enabled a shorter L. This is known as the Petschek reconnection model (Petschek, 1964) and a sketch of this later model is shown in Figure 1.11
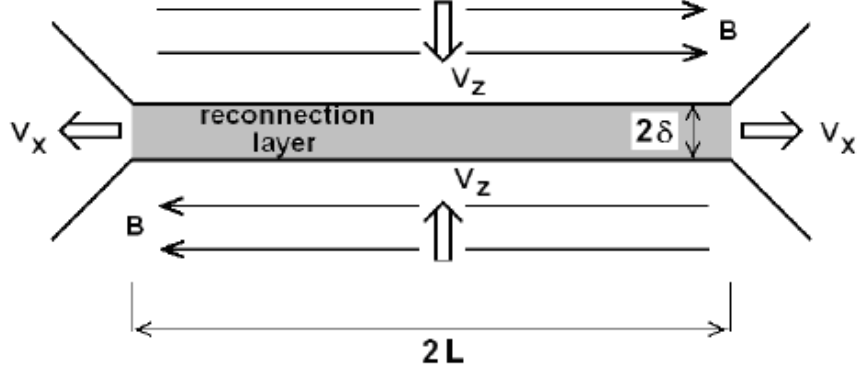
Figure 1.10: A sketch of Sweet-Parker model. The reconnection region is a current sheet with finite width (2δ) and length (2L). Image from Lyatsky & Goldstein (2013)

In the Petschek model, the reconnecting current sheet becomes shorter. Thus it has a higher reconnection rate. To achieve this, the model requires that not all plasma goes through the diffusion region. Instead, most plasma changes flow direction before reaching the X-line and forms two pairs of slow mode shock. It is a steepened slow magnetosonic wave and can convert the upstream magnetic energy to accelerate as well as heat the plasma.

The nature of magnetic reconnection is much more complicated than the fluid description. It is a process that couples multiple scales. Smaller than the fluid scale, when we investigate the reconnecting current sheet or the diffusion region, there are more scales. When we get down to the scale that is comparable to the ion gyro-radius we notice that ions become decoupled from the magnetic field line. This region is referred as ion diffusion region (IDR). The Hall term in the generalized Ohm's law (the second term in the right-hand-side of equation 1.10) is no longer negligible. In a even smaller region embedded in IDR, electrons become decoupled and this smaller region is known as electron diffusion region (EDR). Here, the electron pressure gradient is more important. A sketch of the ion and electron diffusion region is shown in Figure 1.12

$$\mathbf{E} + \mathbf{v_e} \times \mathbf{B} = \eta\mathbf{J} + \frac{1}{ne}\nabla \cdot \mathsf{P}_e + \frac{m_e}{ne^2}\frac{\partial\mathbf{J}}{\partial t} \tag{1.10}$$

17
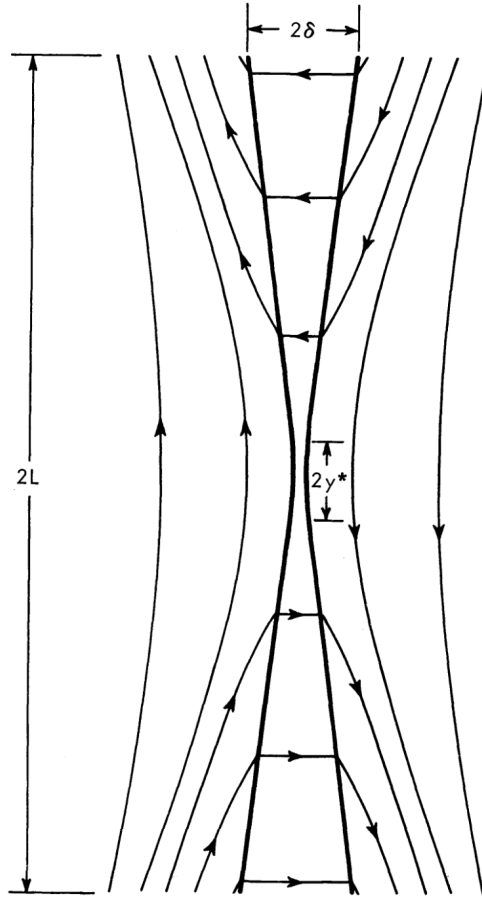
Figure 1.11: A sketch of Petschek model from Petschek (1964)
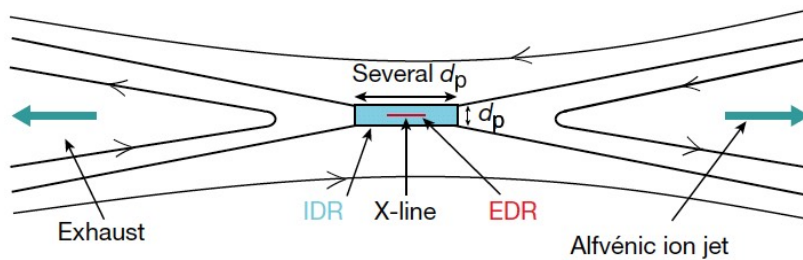
Figure 1.12: Schematic plot of the ion diffusion region and electron diffusion region. Adapted from Verscharen et al. (2021)

1.5 Magnetospheric Multiscale Mission

Magnetic reconnection can occur in various environments. Besides at the magnetopause and in the magnetotail, magnetic reconnection is also found in the laboratory plasma, in

planetary magnetospheres, at the edge of the heliosphere, and on the Sun as in solar flares, CMEs, and prominence eruptions.
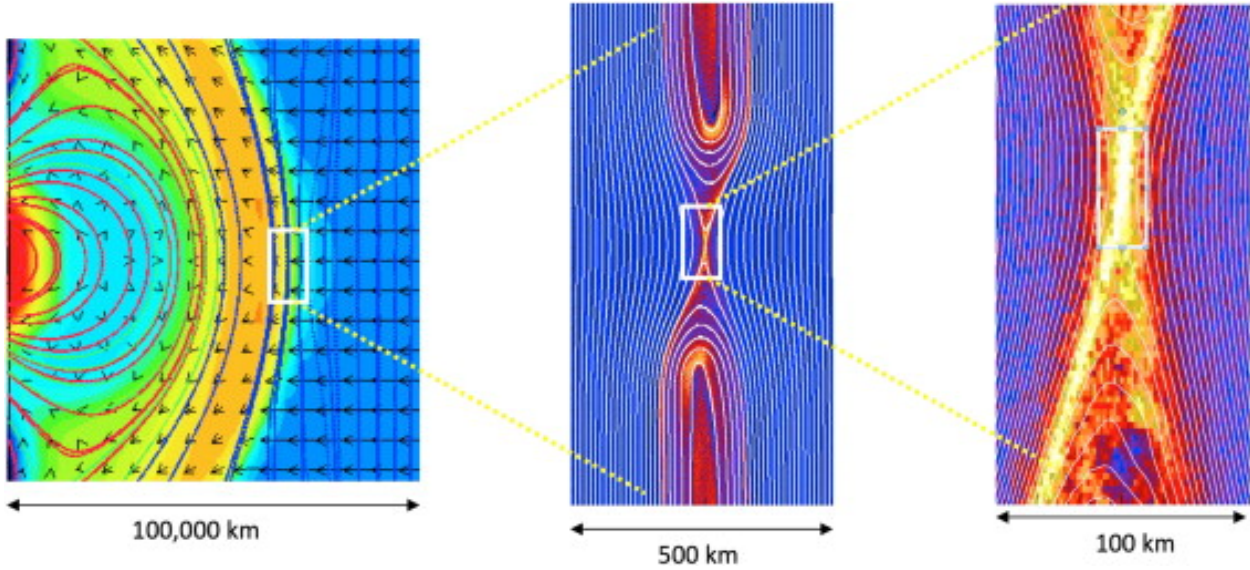
Figure 1.13: Illustration of multiple scales coupling in magnetic reconnection at the magnetopause. Image from Moore et al. (2013)

We have introduced the multi-scale nature of magnetic reconnection, and in different environments, the value of the multiple scales that are involved in the process of magnetic reconnection is also different. In the region of interest in this study, i.e. the magnetopause, the fluid scale is on the order of several Earth Radii (RE), the ion scale is associated with the ion inertial length ($d_i = c/\omega_{pi}$, where c is the speed of light, ω_{pi} is the ion plasma frequency defined as $\omega_{pi} = ZeB/m_ic$ where Z is the charge state, e is the elementary charge, B is the magnetic field strength, and m_i is the ion mass) or the gyro-radius ($r_i = Zm_iv_{Ti}/eB = v_{Ti}/\omega_{ci}$, where v_{Ti} is the ion thermal velocity). It is usually a couple of hundred km. The smallest scale is the electron scale which is associated with the electron inertial length ($d_e = c/\omega_{pe}$, where ω_{pe} is the electron plasma frequency defined as $\omega_{pe} = eB/m_ec$ and m_e is the ion mass) or the gyro-radius ($r_e = m_ev_{Te}/eB = v_{Te}/\omega_{ce}$, where v_{Ti} is the electron thermal velocity). It is usually at the order of 10 km. An illustration of these different scales coupling together is shown in Figure 1.13

To investigate magnetic reconnection in detail, we not only need high enough resolution
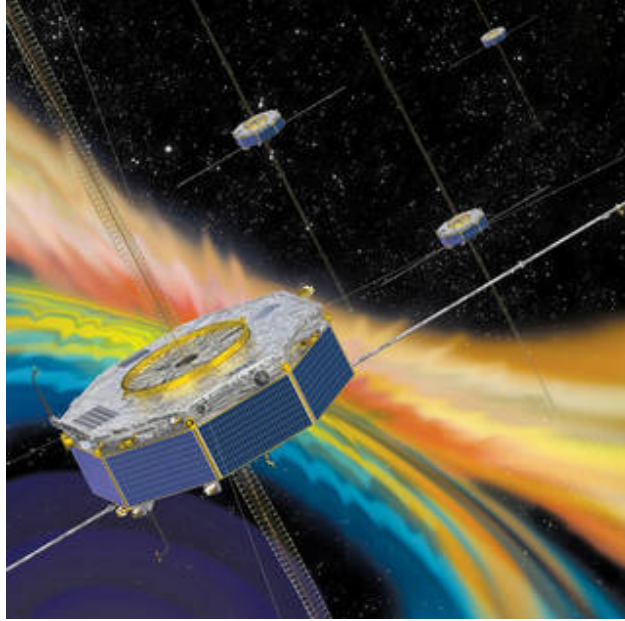
(a) MMS in space.
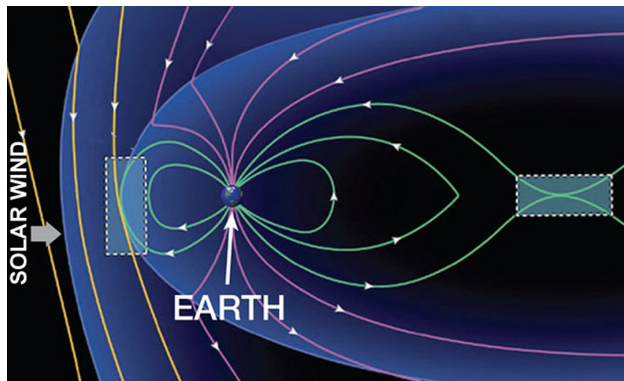
(b) MMS study areas.

Figure 1.14: Panel (a): illustration of MMS spacecraft in space. Panel (b): sketch of the MMS study areas. Image from: NASA MMS mission overview

to solve the physics at the smallest electron scale, but also need three-dimensional spatial observations to reveal the complexity of reconnection sites in addition to a simplified two-dimensional model. The Magnetospheric Multiscale mission (MMS) (Burch et al., 2015) was designed for this.

This four-spacecraft constellation was launched on March 12, 2015 and was designed to

investigate magnetic reconnection in the boundary regions of the Earth's magnetosphere, particularly along its dayside boundary with the solar wind and the neutral sheet in the magnetic tail. After the launch, the spacecraft stayed in a low-inclination elliptical orbit with an initial perigee of 1.08 RE and an apogee of 12 RE (Fuselier et al., 2016). Phase 1a started on September 1, 2015 and lasted approximately 180 days. During this phase, the spacecraft targeted the dayside magnetopause.

The orbit remained at a low inclination around 20 degrees. Following Phase 1a, the nightside transition phase started on March 8, 2016. The apogee remained at 12 RE. The latitude constraint of the orbit was relaxed but remains within 25 degrees. As the orbit precessed, the second dayside phase started on September 12, 2016 (apogee at 10:00 GSE local time). On January 31, 2017, the apogee started to rise and marked the beginning of phase 2a. By the end of commissioning phase, the spacecraft had been put into a tetrahedral formation that was maintained for the following phase. Since the actual width of the diffusion region is unclear, the spacecraft separation is flexible. For the first two months of each phase, the separations are changed every 15 days. For example, in phase 1a, the separation ranges from 160 km to 10 km. Then based on a vote of the science team, the separation remained at the median scale size of 30km for phase one.

The magnetic field is measured by the Fluxgate Magnetometers (FGM) which include an Analog Fluxgate Magnetometer (AFG) and Digital Fluxgate Magnetometer (DFG) (Russell et al., 2014). The burst mode resolution is 128 samples/second. The plasma is observed by the Fast Plasma Investigation (FPI) (Pollock et al., 2016). Electrons and ions are measured separately by eight dual 180-degree top hat spectrometers around the periphery of each identical spacecraft. The 4π sr field-of-view is offered with 11.25-degree sample spacing, and an energy range from 10 eV to 30 keV. The burst mode temporal resolution is 30 ms for electrons and 150 ms for ions.

Both the spatial resolution of the constellation and temporal resolution of the instruments onboard were sufficient to solve the electron-scale structures.
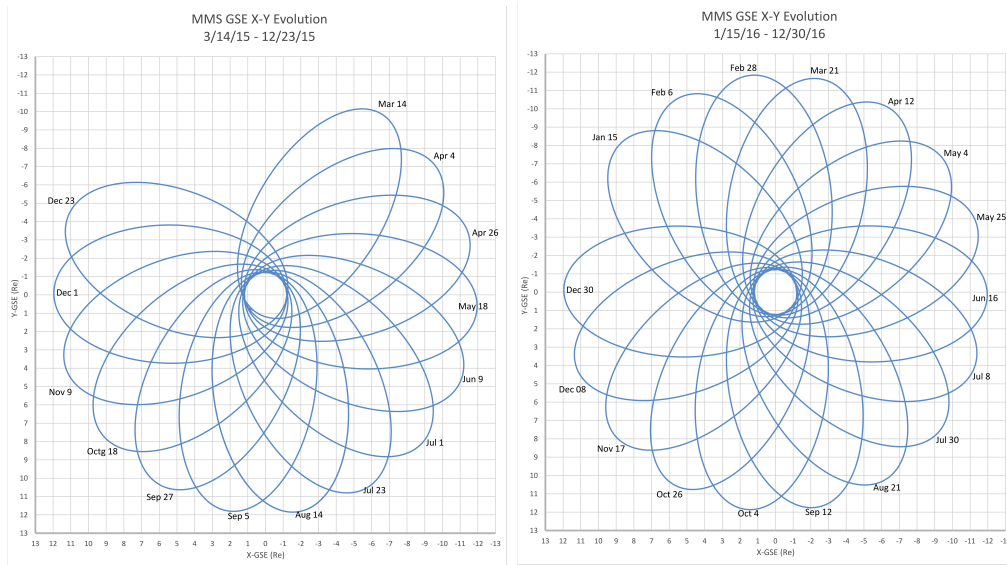
(a)   (b)
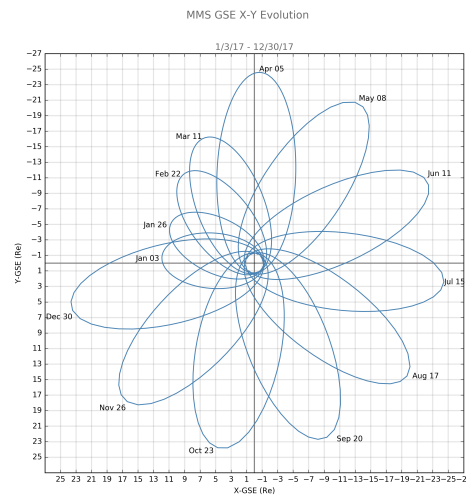
(c)

Figure 1.15: MMS orbits in 2015 – 2017. Image from MMS Science Team Working Home

1.6   Outline

This dissertation is organized as follows: in Chapter 2 we introduce the observational characteristics of magnetic reconnection. Starting from there, we present the results of applying magnetic curvature analysis on the EDR crossings. In addition we introduce a newly
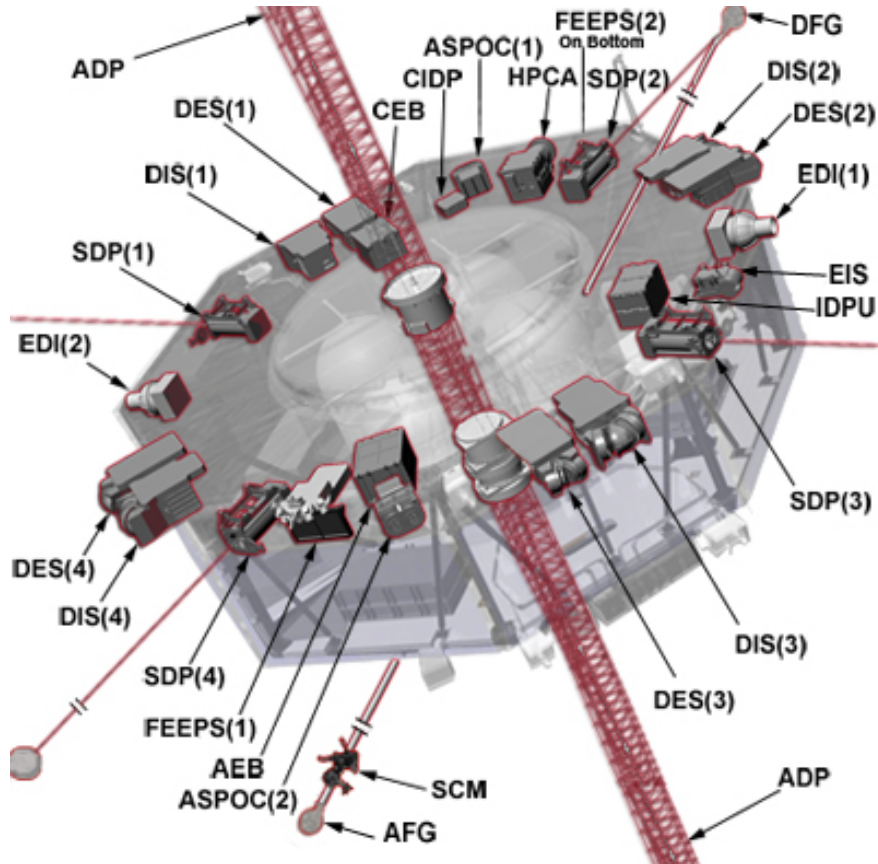
Figure 1.16: Instruments onboard MMS. Image from NASA

developed method to identify active magnetic reconnection which relies on the properties in the Magnetic Flux Transport (MFT). We first show the results in numerical simulations and summarize the desired characteristics. Then we use MMS observations to test and validate the MFT method. In Chapter 3, we focus on the Flux Transfer Events which is the outcome of magnetic reconnection at the magnetopause. We first explain a possible scenario where flux ropes are born in pairs through a Magnetic Entanglement (ME) process where reconnection occurs at the interface of two entangled flux tube and simplifies the geometry by generating two new flux ropes with different connectivities compared with their initial stage. Then we analyze magnetic entanglement events observed by MMS and identified three evolutionary stages of this process. In the last part of Chapter 3 we use a three-dimensional Hall MHD simulation to further examine magnetic entanglement including the feasibility, temporal evolution, and external driver of entanglement. In Chapter 4 we summarize the

dissertation, and propose possible future work.

CHAPTER 2

The Identification of Magnetic Reconnection at the Earth's Magnetopause

In this section we present studies on identifying active reconnection. In Section 2.1, we review the signatures that have been discovered in the past and have been used to identify active reconnection and diffusion regions. In Section 2.2, we show the results of applying magnetic curvature analysis to EDR crossings and the ability of curvature signatures to reveal the existence of reconnecting current sheet. In Section 2.3[1], we introduce a newly developed identification technique, Magnetic Flux Transport (MFT), and present the results from numerical modeling. In Section 2.4[2], we examine the MFT characteristics in reconnection events and test its validity.

2.1 Observational Characteristics of active reconnection

Magnetic reconnection is a fundamental plasma process. During reconnection, the magnetic field lines change connectivity (Dungey, 1961) and facilitate explosive energy conversion from magnetic to particle kinetic and thermal energy resulting in significant heating and acceleration (Treumann & Baumjohann, 2013). Magnetic reconnection is ubiquitous in the universe and occurs under various circumstances such as symmetric and asymmetric upstream conditions, varied guide-field strengths, in relatively quiet and dynamic environments with strong plasma flows. Magnetic reconnection has been seen in laboratory plasmas

---

[1]This section is a version of Li et al. (2021).

[2]This section is a version of Qi et al., "Magnetic Flux Transport Identification of Active Reconnection: MMS Observation in the Earth's Magnetosphere" (manuscript in preparation)

(Dorfman et al., 2013; Ji et al., 1998; Yamada et al., 1990), in the solar corona (Smartt et al., 1993; Xue et al., 2016), and in the solar wind (Fargette et al., 2020a; Phan et al., 2020). At the Earth, the Magnetospheric Multiscale (MMS) mission has detected reconnection events on the dayside magnetopause (Burch et al., 2016; Lavraud et al., 2016; Russell et al., 2017), in the magnetotail (Chen et al., 2019; Hwang et al., 2019; Torbert et al., 2018) and downstream from the bow shock (Phan et al., 2018; Wang et al., 2019)

Magnetic reconnection can couple multiple scales (Hesse & Cassak, 2020). The center of reconnection is the topological X-point/X-line where the magnetic field annihilates and reconnects. Around this site there is a region on the electron scale known as the electron diffusion region (EDR) where both electrons and ions violate the frozen-in condition and are no longer dynamically controlled by the magnetic field (Bessho et al., 2014; Ng et al., 2011; Shay et al., 2016). Signatures of this region include deviation of the electron and ion bulk flow speed from the $\mathbf{E} \times \mathbf{B}$ drift, strong current carried mainly by electrons, electron energization, finite energy conversion ($\mathbf{j} \cdot \mathbf{E}'$, where $\mathbf{j}$ is the current density and $\mathbf{E}' = \mathbf{E} + \mathbf{V}_e \times \mathbf{B}$ is the electric field in the electron frame), the crescent-shaped agyrotropic electron velocity phase space distribution, and a small radius of curvature of the magnetic field (Büchner & Zelenyi, 1989; Le et al., 2013; Tang et al., 2019; Webster et al., 2018) The larger region in which the EDR is embedded in is the ion diffusion region (IDR) where ions are decoupled from the magnetic field while the electrons remain coupled. Here ions are energized, and electrons form a super-alfvenic outflow jet. The separation between ions and electrons results in Hall electric and magnetic fields (Genestreti et al., 2020; Graham et al., 2016). Outside the ion diffusion region, ion outflow becomes super-alfvenic (Phan et al., 2000). We will explain these in more detail in the following subsections.

2.1.1 Ion Outflow Jets and Distribution Function

Outflow jets are one of the most recognizable features of reconnection. The ion outflow jet is generated by the contraction of reconnected magnetic field lines which are highly curved and relax due to the tension force (Haggerty et al., 2018). The magnetic energy is converted

to heat and accelerate the ions, and the speed of the ion outflow jet is expected to be on the order of ion Alfvén speed regarding to the reconnection upstream conditions.

The existence of high-speed ion bulk flow is usually used as an indicator of active reconnection. However, in both observation and simulations, sometimes it is noticed that the ion bulk flow jets are not able to reach the Alfvén speed (for example: (Paschmann et al., 1986),(Liu et al., 2012) and (Phan et al., 1996)). The possible reason is that the firehose instability criterion is reached in the exhaust region and reduces the outflow velocity (Haggerty et al., 2018). Another difficulty of using the ion outflow as the reconnection indicator is that only a bipolar outflow (i.e. flow reversal) can point out the reconnection line with little ambiguity. And this requires a spacecraft trajectory crossing the reconnection site along the L direction (the direction of the anti-parallel reconnecting magnetic field, or the magentic field maximum variance direction). If the spacecraft trajectory is along the N direction (the direction perpendicular to L, but still in the reconnection plane as sketched in Chapter 1 section 1.4), only one ion outflow jet can be observed.

For asymmetric magnetopause reconnection, the largest plasma flow acceleration occurs across the rotational discontinuity (RD) located on the magnetosheath edge of the magnetopause (Levy et al., 2012). Crossing the RD, the plasma flow velocity is described by Walén relation(Hudson, 1970; Paschmann et al., 1986):

$$\Delta \mathbf{v_{predicted}} = \mathbf{v_2} - \mathbf{v_1} = \pm(1-\alpha_1)^{1/2}(\mu_0\rho_1)^{-1/2}\left[\mathbf{B_2}(1-\alpha_2)/(1-\alpha_1) - \mathbf{B_1}\right] \qquad (2.1)$$

where $\mathbf{v}$, $\mathbf{B}$, and ρ are the ion bulk velocity, magnetic field, and proton mass density. $\alpha = (p_\parallel - p_\perp)\mu_0/\mathbf{B_2}$ is the anisotropy factor where $p_\parallel$ and $p_\perp$ are the plasma pressures parallel and perpendicular to magnetic field. The subscription 1 represents the inflow region and 2 represents the outflow region. The Walén relation predicts the correlated or anti-correlated change of the tangential velocity and magnetic field components across the magnetosheath edge of the magnetopause (Phan et al., 2013).

There is strong evidence for reconnection obtained from kinetic effects as well. These effects can be seen from the particles' distribution function. As for ions, the signature is the D-shape 2D distribution (Paschmann et al., 2013; Cowley, 1982). D-shaped ion distributions
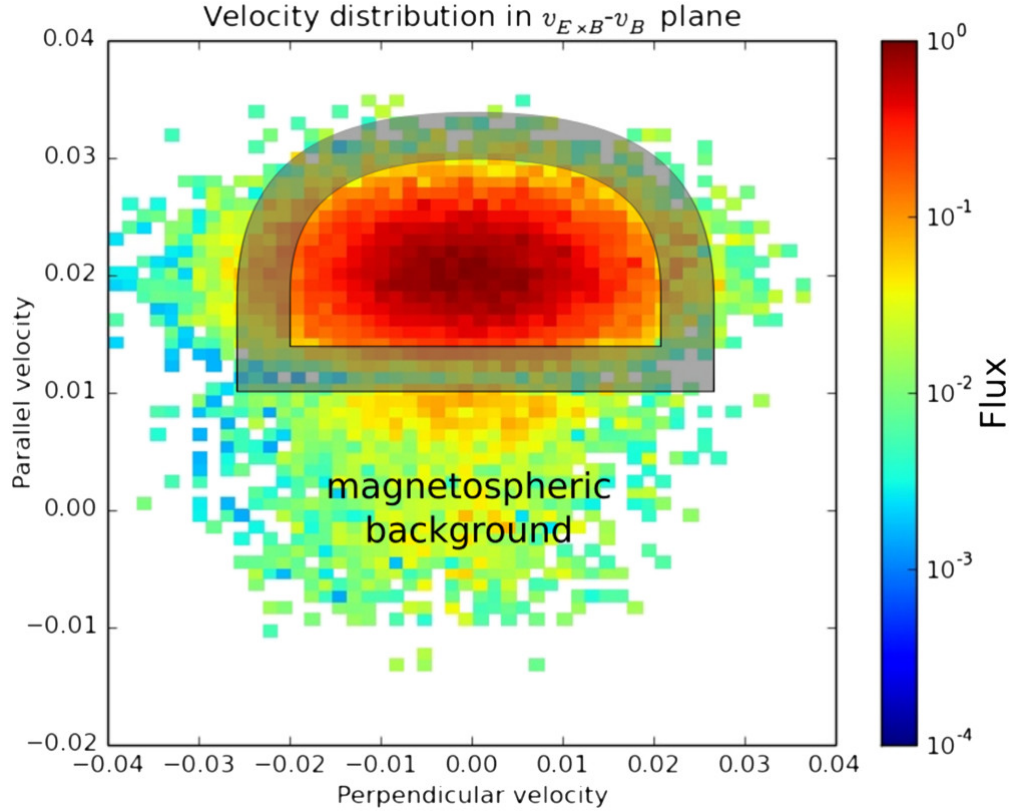
Figure 2.1: Model D-shaped reconnection exhaust distribution. (Figure 2 of Broll et al. (2017))

are a result of heating and acceleration of the entering magnetosheath plasma which lead to a parallel velocity cutoff of ion distribution. An example is shown in Figure 2.1

2.1.2 Hall Effect

At a smaller scale, the ions become unmagnetized while the electrons are magnetized in the current layer. Ions are no longer guided by the magnetic field while electrons are still moving into the reconnection line with the field lines. Sonnerup (1979) first pointed out the importance of this separation between ions and electrons which leads to the formation of a current system flowing antiparallel to the inward convection of the electrons and perpendicular to both the convection electric and the lobe magnetic fields (Treumann et al., 2006)

Figure 2.2 demonstrates the schematics of the Hall currents and magnetic field. The pink large circle represents the ion inertial domain of radius λ_i, and the inner blue circle represents the electron inertial domain. The red arrows indicate the slow inflow convected into the reconnection point and the fast outflow accelerated by the reconnection. Electron motion follows the red arrows and the blue arrows that are opposite to the electron motion indicate the Hall current due to the separation between the electron and ion motion. The existence of the Hall currents generate quadrupolar Hall magnetic and electric fields.
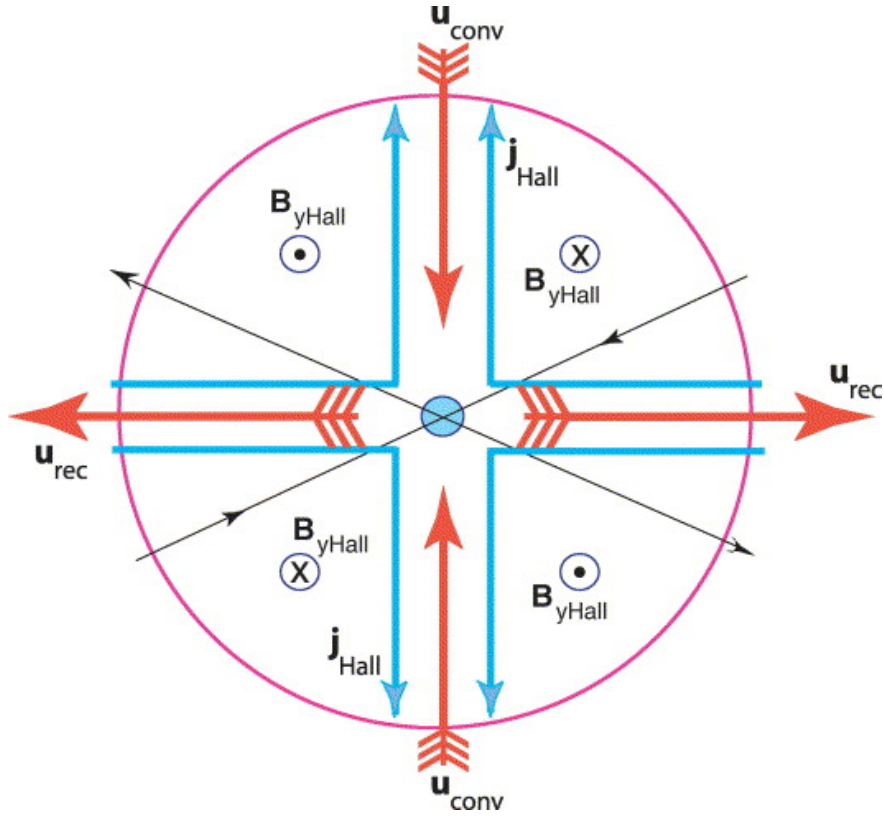
Figure 2.2: The Hall current system schematics. Figure 1 of Treumann et al. (2006)

2.1.3 Reconnection Electric field and Energy Conversion

At the center of reconnection, the scale of the current layer is even smaller and becomes electron-scale. The electric field in this region is referred as the reconnection electric field. This electric field is essential to convert energy and transport magnetic flux from the

upstream region to the reconnection exhaust.

From the generalized Ohm's law we can briefly analyze what supports the reconnection electric field.

$$\mathbf{E} = -\mathbf{v} \times \mathbf{B} + \frac{1}{ne}\mathbf{J} \times \mathbf{B} + \frac{1}{ne}\nabla \cdot \mathsf{P}_e - \frac{m_e}{e}\left(\frac{\partial \mathbf{v_e}}{\partial t} + \mathbf{v_e} \cdot \nabla \mathbf{v_e}\right) \tag{2.2}$$

Ideally in magnetized plasma, the electric field corresponds to the convection of the plasma flow. And the first two terms on the right hand side of Equation 2.2 are equivalent to $-\mathbf{v_e} \times \mathbf{B}$. Move these first two terms to the left hand side and we have that the non-ideal electric field ($\mathbf{E}'$) comes from the remaining terms on the right hand side. The two major contributors of electric field within the electron-scale reconnecting current layer are the pressure term and the inertial term. In regions of sufficiently small magnetic field, the pressure term depends on nongyrotropies of the distribution function (Vasyliunas, 1975; Hesse & Winske, 1993; Lyons & Pridmore-Brown, 1990), and if the inertial term is neglectable, the reconnection electric field becomes:

$$E_y = -\frac{1}{ne}\left(\frac{\partial P_{xye}}{\partial x} + \frac{\partial P_{yze}}{\partial z}\right) \tag{2.3}$$

The anisotropy of the electron pressure gradient is important to support the reconnection electric field.

The asymmetric upstream conditions of dayside magnetopause reconnection will cause the flow stagnation point to deviate away from the reconnection point. In this case, the inertial term plays an important role at the neutral point while the pressure term dominates at the stagnation point (Hesse et al., 2016).

The existence of the reconnection electric field indicates the localized energy conversion. This energy conversion rate is often expressed as the work done by the non-ideal electric field, or $\mathbf{j} \cdot (\mathbf{E} + \mathbf{v}_e \times \mathbf{B}) = \mathbf{j} \cdot \mathbf{E}'$ (Zenitani et al., 2011). A finite energy conversion rate is expected to appear within the EDR (Chen et al., 2017; Burch & Phan, 2016). A positive $\mathbf{j} \cdot \mathbf{E}'$ indicates that the energy is converted from magnetic field to plasma, and a negative $\mathbf{j} \cdot \mathbf{E}'$ indicates that the energy is transferred to the field. Burch et al. (2018) reported oscillatory energy conversion which is associated with an oscillatory electric field pattern that shows

characteristics of both a spatial structure and a propagating wave.

2.1.4 Electron kinetics

In the electron diffusion region, electrons are heated and accelerated (Øieroset et al., 2002). The strong into-the-plane electron jet is a key characteristic of the inner electron diffusion region. Considering the large velocity difference between electrons and ions, even though the quasi-neutrality of plasma still holds, it is reasonable to say that the reconnecting current sheet is mainly supported by electrons. The acceleration or heating of electron can also take place in the reconnection exhaust when the fast reconnection outflow jets collide with the pre-existing plasmas, during which betatron and/or Fermi acceleration can further accelerate electrons (Imada et al., 2007; Khotyaintsev et al., 2010).

The most remarkable signature of the electron kinetic effect is the asymmetric crescent-shaped 2D distribution. This signature was first predicted in simulation (Hesse et al., 2016) and then confirmed by MMS observations.

Figure 2.3 gives an example of the crescent distribution obtained in the numerical modeling. It is in the plane perpendicular to the reconnection geometry. The y and z directions can be viewed as the M and N directions. The distribution has two major parts: one gyrotropic distribution at lower energy and one crescent-shaped element for larger velocities. In the literature this portion is referred to as meandering particles.

With the launch of MMS, the electrons' crescent distribution were observed clearly for the first time. Burch et al. (2016) showed the electron distribution at a magnetopause EDR crossing and similar crescent-shaped distribution is seen on each of the four spacecraft. Figure 2.4 demonstrates electrons with velocities from 0 to 10^4 km/s carrying current out of the page on the left side of the X-line and then flowing upward and downward along the reconnected magnetic field on the right side (Burch et al., 2016). In addition to the predicted perpendicular crescent, a second type of parallel crescent was discovered. According to Egedal et al. (2016), the parallel streaming and the absence of electrons with $\mathcal{E} < \mathcal{E}_\mathcal{X}$ yields the parallel crescent-shaped distributions, where $\mathcal{E}_\mathcal{X}$ is the cutoff energy below which the
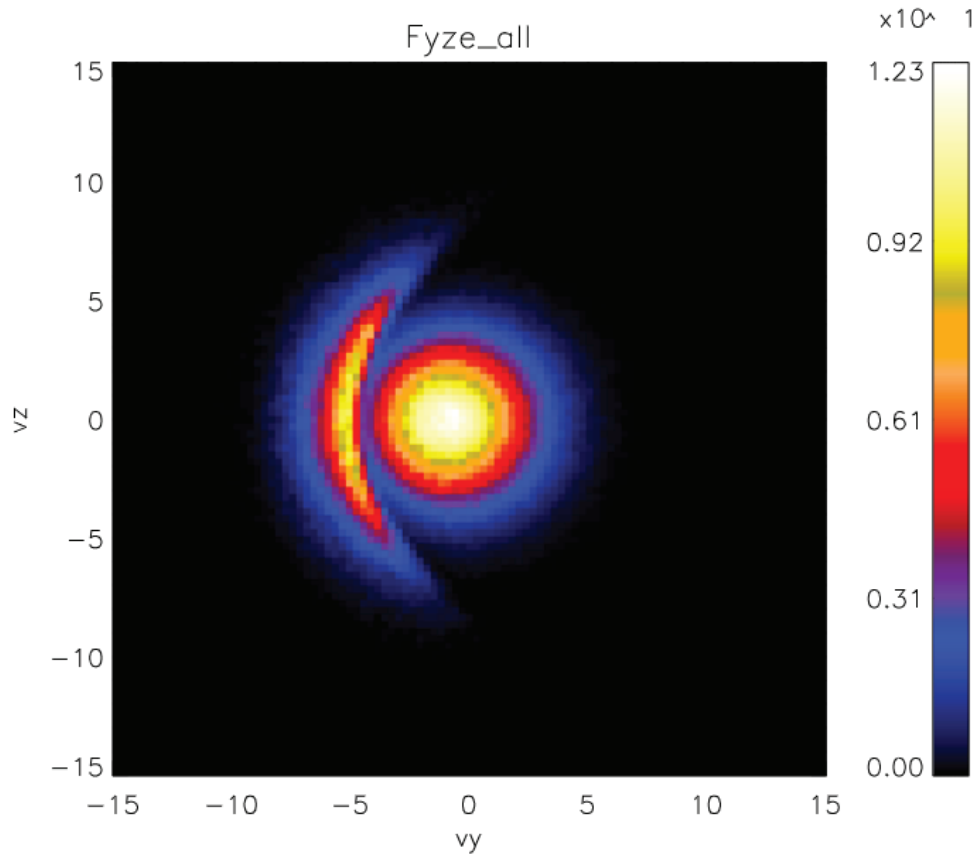
Figure 2.3: Electron crescent distribution in simulation. Reduced distribution $F(v_y, v_z)$ obtained by integrating the full distribution function over the x-component of the velocity. Velocities are in the simulation frame. Figure 4 of Hesse et al. (2016)

particle is not energetic enough to cross the diffusion region.
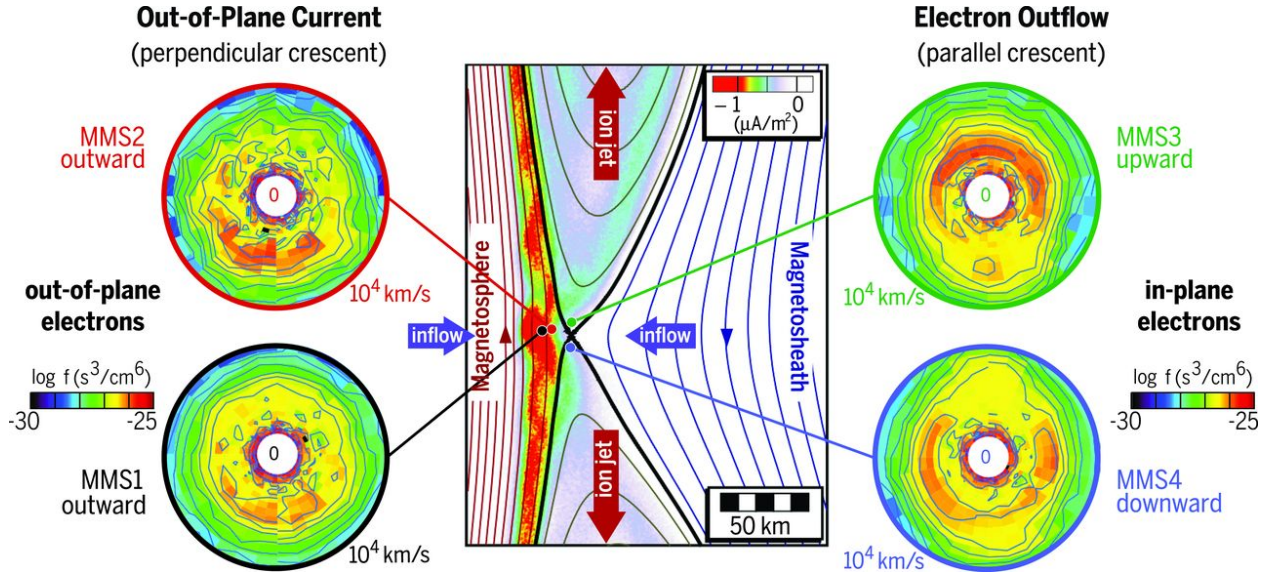
Figure 2.4: Electron crescent distribution in observation. Figure from Burch et al. (2016)

The existence of the electron crescent has become the smoking gun of the diffusion region after these discoveries. Together with the finite energy conversion rate $\mathbf{j} \cdot \mathbf{E}'$, the electron kinetic signature has been used as one of the most important microscopic indicator for later studies that aim at looking for active reconnection and EDRs (for example, (Webster et al., 2018; Lapenta et al., 2017)). A later study by Tang et al. (2019) reported electron crescent being observed at non-reconnecting current sheets due to curvature scattering at electron-scale boundaries. The creation of an electron crescent is not exclusive to reconnection EDRs. This adds complexity to using electron crescents to identify reconnection.

2.2   Magnetic Curvature Analysis

The identification of active reconnection has been challenging. With the high-resolution observations from MMS, we observe most of these mentioned signatures. However, these signatures may not be observed coherently. The trajectory of the spacecraft has a significant influence on the observational profile. In addition, the asymmetry of upstream conditions (Shay et al. 2016b), the existence of finite guide field (Bessho et al. 2019; Ng et al. 2011)

and the strong shear flow (Li et al. 2021; Liu et al. 2018) which is likely in turbulence may all distort the signatures, adding complexity to the active reconnection.

2.2.1 Method

The curvature of the magnetic field is a relatively simpler parameter as it depends only on the magnetic field which can be measured more efficiently than plasma parameters. The radius of curvature demonstrates the spatial scale of the magnetic field variations, and comparing it to the electron/ion scale can provide information about how "stable" the particle motion is in a current sheet. The curvature analysis has the potential to reveal the electron diffusion region in a straightforward way, and further to be used to identify active reconnection.

The curvature vector is defined by $\mathbf{C} = \mathbf{b} \cdot \nabla \mathbf{b}$, where $\mathbf{b}$ is the unit vector of the magnetic field, and accordingly the radius of curvature is given by $R_c = 1/|\mathbf{C}|$. The simplest case is a Harris current sheet with a constant small normal component Bn, which to the first order approximation can be written as $B_z = [B_0(z/L), 0, B_n]$ where B_0 is the reference magnetic field and L is the half-thickness of the current sheet. A scalar parameter κ is then defined by the ratio of the radius of curvature to the particle's gyro-radius (Büchner & Zelenyi, 1989):

$$\kappa = \sqrt{\frac{R_{c,min}}{\rho_{max}}} = \sqrt{b_n{}^2 \frac{L}{\rho_0}} = \frac{B_n}{B_0}\sqrt{\frac{L}{\rho_0}} \tag{2.4}$$

$R_{c,min}$ is the minimum radius of curvature at the center of the current sheet, and ρ_{max} is the maximum gyro-radius calculated by $(m \cdot v_0)/(e \cdot B_n)$ where m is the mass of the particle, v_0 is velocity directed perpendicular to the minimum field B_n. ρ_0 is the gyro-radius about the reference field. b_n is the n component of the magnetic field unit vector $\mathbf{b} = \mathbf{B}/B$. This kappa parameter is proportional to the current sheet half-thickness relative to its ambient plasma condition. Based on analysis in Büchner & Zelenyi (1989), when κ is much greater than 1, particle motion is adiabatic in this current sheet. And when κ is approaching unity, particle motion becomes stochastic. When κ is about 1, particle motion becomes highly chaotic.

The uncertainty of the curvature as well as the radius of curvature is on the order of

$1/6(L/2R_c)^2$ where L is the spacecraft separation. When L is significantly smaller than the radius of curvature, this error can be ignored. Take the MMS 2016 Oct 16 13:06:02 event (the most famous dayside reconnection event originally reported by Burch et al. (2016)) for example, the minimum R_c is $\sim$ 7 km while the spacecraft separation is 14 km. Even at this extreme condition, the error is smaller than 1.2km. When we plot this error bar on the figure, frequently it is not even visible. Also as we will show in later sections, the curvature signature is very localized. Thus, moving away from the minimum location, the radius of curvature increases rapidly, which leads to much smaller error.

2.2.2 Magnetic Curvature Signatures in the Magnetic Reconnection Observations

To investigate reconnection signatures with the MMS magnetometer data, we rotate the data into a boundary normal ("LMN") coordinate system where L aligns with the magnetic field in the magnetosphere, N is perpendicular to the boundary and points outward from the Earth, and the remaining direction is defined by M = N × L. Ideally, in this frame, the reconnecting field lines at the magnetopause should be in ±L, while the N and M components remain small but non-vanishing. The outflow electron and ion jets are both expected along the ±L direction. Other expected reconnection features include a significant parallel electric field at the current sheet and non-zero j · E' energization of the plasma. Here E' = E + Ve × B, where j is the current density. E is the electric field, Ve is the electron velocity, and B is the magnetic field. E' represents the electric field in the electron-steady frame. These processes can violate the electron frozen-in condition and lead to the magnetic-particle energy conversion. Figure 2.5 gives an example of identifying active reconnection sites for two previously identified events (Webster et al., 2018).

Figure 2.5 (a-h) illustrates Event 1 on Oct 16, 2015, and Figure 2.5 (i-p) demonstrates Event 2 on Dec 6, 2015. Major differences between these two events are in the L component of the ion bulk flow (Figure 2.5 panel e, m). Event 1 shows a bipolar flow signature, indicating an ion outflow reversal, while event 2 shows a unipolar flow signature, indicating the observer
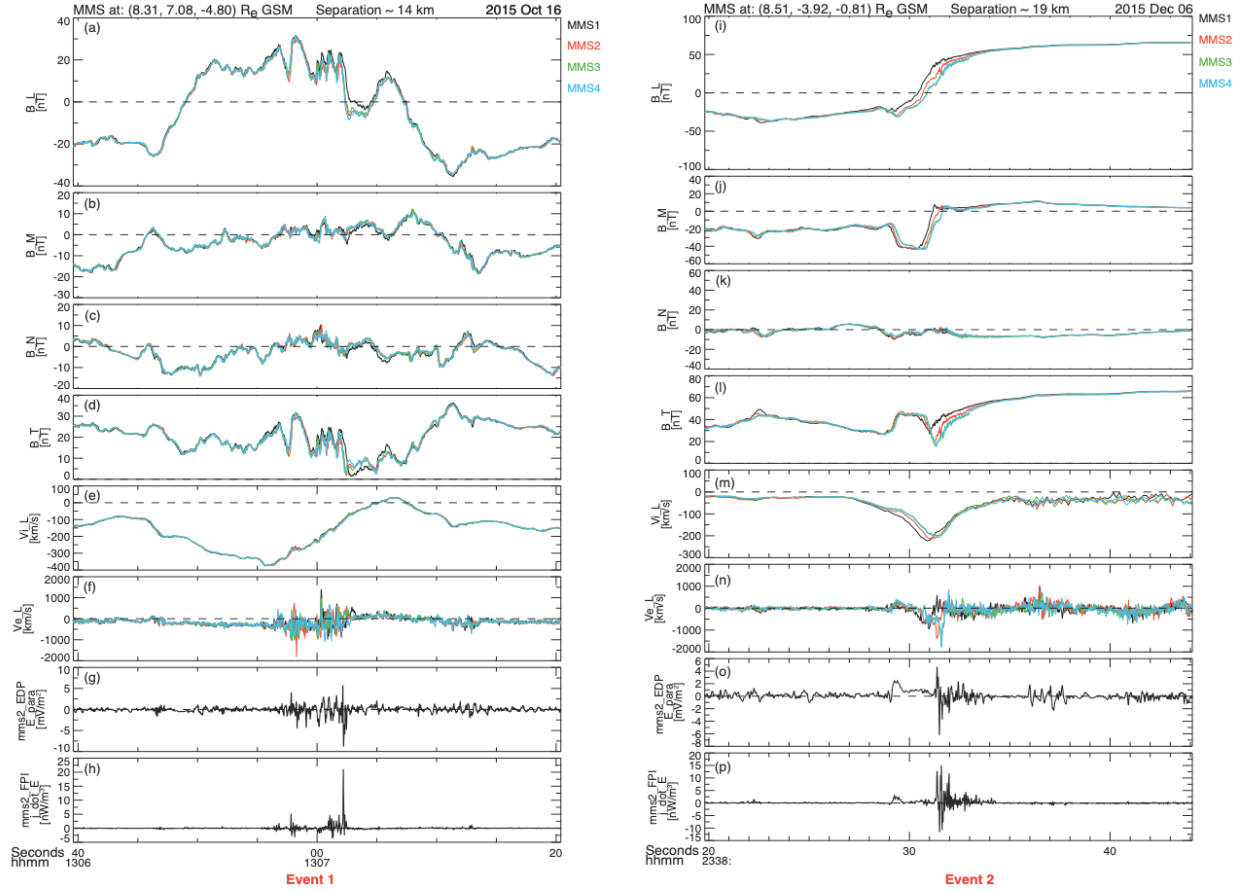
Figure 2.5: Example of identifying active reconnection sites for two previously identified events. The LMN coordinate system in Event 1 is defined by: L = (0.39, 0.46, 0.80)GSM, M = (-0.12, -0.83, 0.54)GSM, N = (0.91, -0.31, -0.27)GSM; in Event 2, it is defined by: L = (0.32 , 0.34, 0.89)GSM, M = (-0.61, -0.79, -0.081)GSM, N = (0.73, -0.51, -0.46)GSM. MMS2 data is used in g, h, o, p, and data from all four spacecraft are plotted simultaneously in other panels represented by different colors. (a-d), (i-l), the magnetic field components and magnitude. (e, m), L component of ion bulk flow velocity. (f, n), L component of electron bulk flow velocity. (g, o), Electric field parallel to the magnetic field. (h, p), the magnetic-particle energy conversion computed by $\mathbf{j} \cdot \mathbf{E}'(\mathbf{E}' = \mathbf{E} + \mathbf{v_e} \times \mathbf{B})$.

is always below the reconnection line (the ion flow leaving the reconnection line and measured by the spacecraft is toward the negative L direction). The other features, although prominent compared with their surroundings, do not clearly reveal the possible differences of the two events. The electron bulk flow (panel (f), (n)) reached a peak value larger than 1000 km/s, approaching 2000 km/s. The maximum parallel electric field (panel (g), (o)) both exceed 5 mV/m, but are less than 10 mV/m. The largest energy conversion (panel (h), (p)) calculated from high-resolution electric field data is also similar, both around $15 \sim 20 \ nW/m^3$. These values are indicative of active reconnection, but without appropriate normalization, they do not demonstrate the relative distance away from the reconnection line. This is where quantitative curvature identification becomes informative.

Figure 2.6 shows an analysis of the same two events using curvature identification. The top part of the figure (panel (a-d), (i-l)) covers the same time interval as in Figure 2.5. The bottom part (panel (e-h), (m-p) shows the enlargements of the orange shaded region containing the radius of curvature minima. The normalized radius of curvature is the ratio of the radius of curvature (R_c) to the ion gyroradius (ρ_i, blue lines in Figure 2.6 (a), (i), labeled as Ri_gyro) and the electron gyroradius (ρ_e, red lines in Figure 2.6 (a), (i), labeled as Re_gyro). This ratio mostly remains much larger than unity. Only when close to the estimated reconnection event time (13:07:02 UT in Event 1 and 23:38:31 UT in Event 2), does the radius of curvature start to decrease rapidly. In Event 1, R_c/ρ_i is very close to 0.01, and the R_c/ρ_e also approaches 10. This implies that in the vicinity of the Rc minima, the motion of electrons has already begun to be chaotic and eventually lead to diffusion. The diffusion regions of ions and electrons are on quite different scales, which can be seen from Figure 2.6 (a), (i), where small R_c/ρ_i occurs in a wider region compared to the small R_c/ρ_e region. Meanwhile, if we look at the normalized Rc in Event 2, it never decreases to a value as small as in Event 1. This tells us that in Event 2, it is less likely that the spacecraft crossed a strong diffusion region for either ions or electrons. The field lines are not sufficiently curved, and the particles can still maintain their gyro-motion around the field lines. Thus, the relative location of the MMS crossing is farther from the reconnection
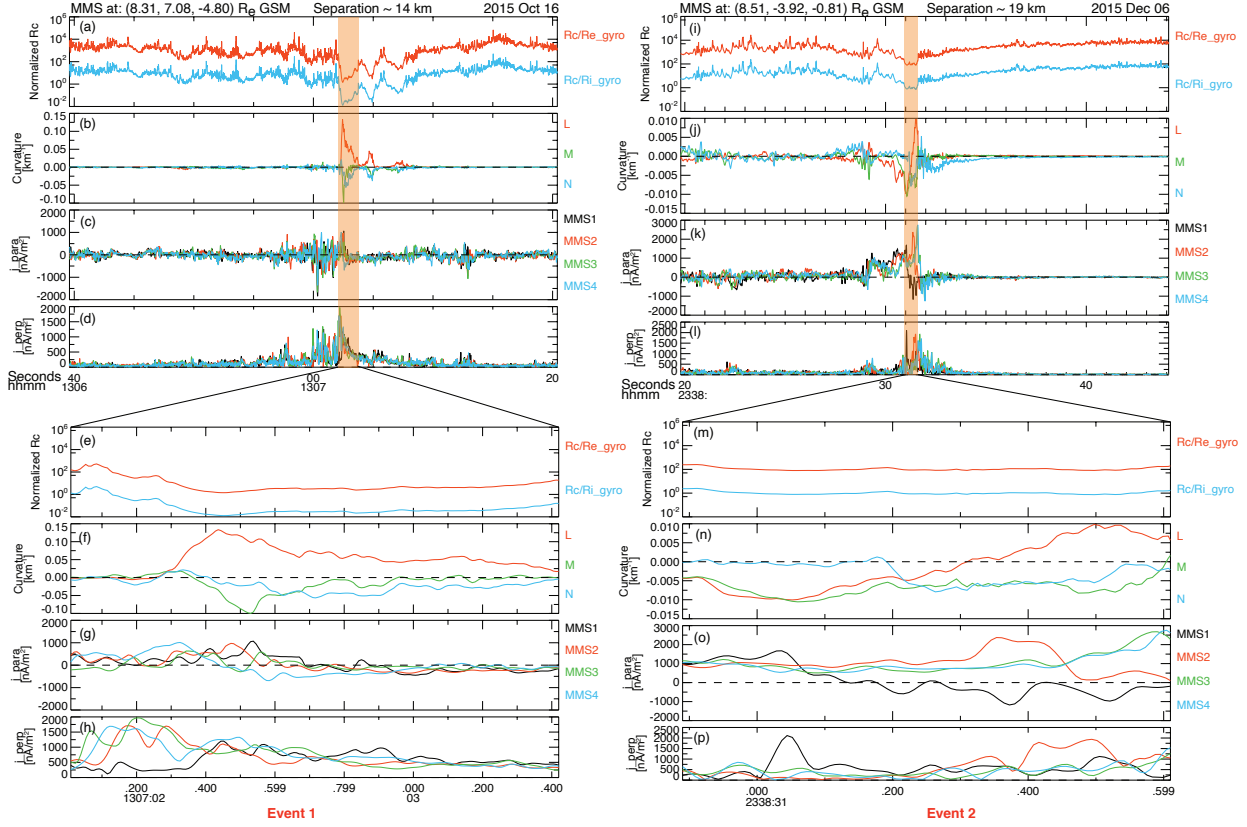
Figure 2.6: The curvature analysis of two reconnection events. The top half of the plot demonstrates the two events in the same time interval as in Figure 2.5, and the bottom half of the plot demonstrates the blowup of the orange shaded region where the radius of curvature decreased. (a, e, i, m), The normalized radius of curvature, the red (blue) lines represents the ratio of radius of curvature to the electron (ion) gyro-radius. (b, f, j, n), The curvature. (c, g, k, o), The parallel part of the current density computed by particle data ($\mathbf{j} = n_e e(\mathbf{v_i} - \mathbf{v_e})$) in GSM coordinates. (d, h, l, p), The perpendicular current density.

line in Event 2 than it is in Event 1.

In the exhaust region, the direction of the field-line curvature pulls away from the reconnection line. The tension force tries to straighten the field line and accelerate plasma from the diffusion region. The curvature changes its direction not only when crossing the reconnection line, but also when crossing the separatrices. In Event 1, the L component

of curvature (Figure 2.6f) remains positive, showing that the spacecraft is probing above the reconnection line in the exhaust. In contrast, in Event 2, the L component of curvature (Figure 2.6n) reverses near 23:38:31.310, indicating that MMS is crossing the separatrix. For both events, there are small-scale current structures embedded in the small Rc region (orange shade). In Event 1, MMS 4 measured anti-parallel currents (blue line in Figure 2.6g) from 13:07:02.450; MMS 1 observed different perpendicular currents (black line in Figure 2.6h) before 13:07:02.400. In Event 2, peak times of parallel (Figure 2.6o) and perpendicular (Figure 2.6o) currents are different at the four spacecraft. These features indicate that the scale of the current sheets here is even smaller than the spacecraft separation (about 3 electron gyro-radii in Event 1, and 16 electron gyroradius in Event 2). Since the curvature is calculated at the barycenter of the satellite, the existence of these small-scale currents indicates that the Rc of the magnetic field may be even smaller than our calculation, possibly even smaller than the electron gyroradius.

In Event 1, to the right of the orange shading, there are another two decreases (Figure 2.6a) in the radius of curvature. These are associated with the oscillation of the magnetopause. The reconnection site moves back and forth and encounters the MMS more than once. Considering the southward motion of the reconnection line (the negative L component offset of the ion flow velocity in Figure 2.5e), the second and third encounters are farther away from the reconnection line, compared with the first encounter. This is consistent with the growing Rc minima in 2.6a. This also indicates that the reconnection line can remain quasi-stationary between these two crossings and can extend in the M-N plane (the reconnection line also moves in the M-N plane, thus the three crossings are at different M locations).

Our findings confirm the hypothesis that the radius of curvature can quantitatively evaluate near-reconnection-line encounters. The smaller the Rc relative to the particle's gyroradius, the easier the particle can "escape" from its gyromotion around the field line. The varying Rc in our examples reflects the changing relative distance to the reconnection-line where Rc reaches minimum. The direction of the curvature also helps to diagnose whether the spacecraft passed the separatrices. With curvature identification, we also verify the

existence of an extended quasi-stationary reconnection line on the magnetopause. This micro-scale mechanism provides persistent, macroscopic energy/momentum transfer from the shocked solar wind to the magnetosphere, powering the Earth's macro-scale magnetosphere processes. Since this process depends only on the relative scale length of the magnetic field in terms of the electron gyroradius, it is scalable for terrestrial, solar and astrophysical processes, allowing us to understand the behavior of magnetized current sheets from laboratory devices to astrophysical objects.

However we also want to note that using curvature signatures only is not enough to prove the existence of active reconnection. A small Rc can exist at thin current sheets where traditional large-scale explosive reconnection has not yet developed. For example, such electron scale boundaries are ubiquitous in the turbulent magnetosheath or shock transition region. The relationship between these electron-scale current sheets and the reconnection onset is still an open question and we would like to leave this study as future work.

2.3 Magnetic Flux Transport: Theories and Simulations

2.3.1 Introduction

Magnetic reconnection and plasma turbulence are both fundamental processes operating throughout the universe. Reconnection has been suggested to contribute to energy dissipation (Dmitruk et al., 2004; Sundkvist et al., 2007; Osman et al., 2011, 2012; Markovskii & Vasquez, 2011; Perri et al., 2012; Wan et al., 2012; Karimabadi et al., 2013; TenBarge et al., 2013; Wu et al., 2013; Zhdankin et al., 2013; Shay et al., 2018) and potential changes in the cascade (Loureiro & Boldyrev, 2017; Boldyrev & Loureiro, 2017; Mallet et al., 2017; Franci et al., 2017; Mallet et al., 2017; Loureiro & Boldyrev, 2017; Vech et al., 2018; Stawarz et al., 2019) of turbulence by in-situ observations, numerical simulations and theory. In heliospheric turbulence, reconnection was first observed in-situ in the terrestrial magnetosheath on Cluster (Retinò et al., 2007). Recently, high resolution measurements from MMS (Burch et al., 2016) have enabled the detection of electron jets in small-scale current sheets in the turbulent

magnetosheath (Yordanova et al., 2016; Vörös et al., 2017; Phan et al., 2018; Wilder et al., 2018), including notably, electron-only reconnection (Phan et al., 2018).

Reconnection occurs in a small-scale electron diffusion region (EDR) within a thin current sheet. As upstream field lines flow into the EDR, they reconnect at the X-point. The reconnected field possesses strong magnetic tension, which drives the reconnected field away from the X-point, ejecting plasma that is coupled to it as bi-directional outflow jets. The fundamental process of reconnection can be described as inward and outward transport of magnetic flux and associated plasmas at an X-point. The transport of magnetic flux and plasma flows across a separatrix was used to define reconnection (Vasyliunas, 1975).

At the frontier of turbulence and reconnection research, important questions include how reconnection occurs in a dynamical turbulent system and how the rich dynamics of turbulence and reconnection, such as turbulent energy dissipation and cascade, interplay. Nevertheless, there is still no clear, reliable method to identify reconnection X-points in turbulent plasmas. In 2D turbulence simulations, the method of saddle points that define an X-point topology was applied (Servidio et al., 2008, 2010; Wan et al., 2013; Haggerty et al., 2017). However, among many identified X-points, only a few displayed significant reconnection electric fields (Servidio et al., 2008). It is possible that many identified X-points are not actively reconnecting.

In observations, a commonly used method to identify reconnection is the detection of bi-directional Alfvénic ion outflow jets. In a turbulent system such as the terrestrial magnetosheath, reconnection can happen at sub-ion or electron scales (Wilder et al., 2018; Phan et al., 2018), and electron jets becomes the conclusive signature of reconnection. However, fast turbulent flows at sub-ion scales can make the detection challenging. In fact, only one out of several tens of sub-ion-scale current sheets detected by Phan et al. (2018) displayed clear bi-directional reconnection electron jets.

Recently, the transport of magnetic flux around an X-point was considered in kinetic simulations of reconnection (Liu & Hesse, 2016; Liu et al., 2018). MFT considers the decoupling of electron flow and magnetic flux (slippage) arising from a non-ideal electric field,

and thus correctly captures the inward and outward transport of magnetic flux around a reconnection X-point. In a symmetric reconnection simulation with shear flows, the electron flow can be highly distorted (Liu et al., 2018). Under stronger shear flows or asymmetry likely in turbulence, the electron flow may not show typical reconnection outflows. In fact, in a highly asymmetric configuration, active reconnection with only one electron jet is possible (Liu & Hesse, 2016).

2.3.2   Theory

The transport of magnetic flux inherent to reconnection represents an innovative way for identifying active reconnecting X-points in turbulence. The presence of inward flux transport also indicates reconnection is actively taking place. The MFT velocity $\mathbf{U}_\psi$ was previously derived in one and two dimensions (Liu & Hesse, 2016; Liu et al., 2018). The key steps leading to the definition of $\mathbf{U}_\psi$ are summarized here. In 2D, the magnetic field can be represented as an in-plane and out-of-plane (guide field) component directed along $\hat{\mathbf{z}}$: $\mathbf{B} = \hat{\mathbf{z}} \times \nabla\psi + B_0\hat{\mathbf{z}}$. Curling the Faraday's law: $\hat{\mathbf{z}} \times [\,\partial_t\mathbf{B} + c\nabla \times \mathbf{E} = 0\,]$ results in $\partial_t\psi = cE_z$. We then consider the electron momentum equation: $\mathbf{E} + \mathbf{v}_e \times \mathbf{B}/c = \mathbf{E}'_e$, where $\mathbf{E}'_e$ is the non-ideal electric field in the electron frame. Taking the z component of this equation and casting it into the form of the 2D advection equation of magnetic flux: $\partial_t\psi + \mathbf{U}_\psi \cdot \nabla_\perp\psi = 0$, the in-plane MFT velocity is then given by:

$$\mathbf{U}_\psi \equiv \mathbf{v}_{ep} - (\mathbf{v}_{ep} \cdot \hat{b}_p)\hat{b}_p + \frac{cE'_{ez}}{B_p}(\hat{\mathbf{z}} \times \hat{b}_p), \tag{2.5}$$

where $\hat{b}_p \equiv \mathbf{B}_p/B_p$ is the unit vector of the in-plane magnetic field $\mathbf{B}_p$ and $\mathbf{v}_{ep}$ the in-plane electron flow. The first two terms represent the in-plane electron flow perpendicular to $\mathbf{B}_p$. They come from the $\mathbf{v_e} \times \mathbf{B}$ term in the electron momentum equation. For $\mathbf{E}'_e$=0, the electron flow is frozen-in to the magnetic field and they move together. When $\mathbf{E}'_e \neq 0$, slippage between magnetic flux and electron flow arises as the last term. Without separating the perpendicular electron flow and slippage terms, which provide a relation between the transport of magnetic

flux and electron flow, Equation (2.5) can be simplified to:

$$\mathbf{U}_\psi = \frac{cE_z}{B_p}(\hat{\mathbf{z}} \times \hat{b}_p). \tag{2.6}$$

To the first order in gyrokinetics, $\mathbf{U}_\psi$ is given by Equation (2.5) or (2) with $\mathbf{v}_{ep}$, $\mathbf{B}_p$ and E'_{ez} replaced by $\delta\mathbf{u}_{ep}$, $\delta\mathbf{B}_p$ and $\delta E'_{ez} = \delta E_z + (\delta\mathbf{u}_{ep} \times \delta\mathbf{B}_p/c)_z$, where fluctuating quantities in turbulence are the in-plane electron bulk flow $\delta\mathbf{u}_{ep}$ and so on. Note that Equation (2.5) is not applicable at the X-point because a source or sink term, representing flux generation or annihilation at the X-point, is not included in this advection equation.

A new quantity, the divergence of MFT, $\nabla \cdot \mathbf{U}_\psi$, is considered here. $\nabla \cdot \mathbf{U}_\psi < 0$ and > 0 can capture the converging inflows and diverging outflows of magnetic flux, respectively. These bi-directional inflows and outflows of magnetic flux at an X-point signifies active reconnection. $\nabla \cdot \mathbf{U}_\psi$ also informs about the time scale of diverging magnetic flux from the X-point. Having the dimension of inverse time, $\nabla \cdot \mathbf{U}_\psi$ is frame-independent in 2D in the non-relativistic limit. Therefore, one can compute $\nabla \cdot \mathbf{U}_\psi$ for moving X-points without changing frames.

2.3.3 Code

The 2D gyrokinetic turbulence simulation has been previously performed (Li et al., 2016) using the the Astrophysical Gyrokinetics Code, or `AstroGK`, described in detail in (Numata et al., 2010). `AstroGK` has been extensively used to investigate turbulence in weakly collisional plasmas (Howes et al., 2008; Tatsuno et al., 2009; Howes et al., 2011; TenBarge & Howes, 2012; Nielson et al., 2013; TenBarge et al., 2013; Howes, 2016; Li et al., 2016; Howes et al., 2018; Li et al., 2019) and collisionless strong-guide-field reconnection (Numata et al., 2011; TenBarge et al., 2014; Kobayashi et al., 2014; Numata & Loureiro, 2015). `AstroGK` is an Eulerian continuum code with triply periodic boundary conditions. It has a slab geometry elongated along the straight, uniform background magnetic field, $\mathbf{B}_0 = B_0\hat{\mathbf{z}}$. The code evolves the perturbed gyroaveraged Vlasov-Maxwell equations in five-dimensional phase space (three-dimensional-two-velocity) (Frieman & Chen, 1982; Howes et al., 2006).

The evolved quantities are the electromagnetic gyroaveraged complementary distribution function for each species s, the scalar potential φ, parallel vector potential $A_\parallel$ and parallel magnetic field perturbation $\delta B_\parallel$, where $\parallel$ is along the total local magnetic field $\mathbf{B} = B_0\hat{\mathbf{z}} + \delta\mathbf{B}$. The total and background magnetic fields are the same to first-order accuracy retained for perturbed fields in gyrokinetics. The velocity grid is specified by pitch angle $\lambda = v_\perp^2/v^2$ and energy $\varepsilon = v^2/2$. The background distribution functions for both species are stationary uniform Maxwellians. Collisions are incorporated using a fully conservative, linearized gyro-averaged Landau collision operator (Abel et al., 2008; Barnes et al., 2009).

2.3.4 Simulation Setup

The 2D Orszag-Tang Vortex (OTV) problem is a 2D MHD initial condition that involves a system size vortex stretching two large-scale magnetic islands in periodic geometry. OTV is a strongly nonlinear initial condition that evolves into turbulence very quickly and it has been widely used to study plasma turbulence (Politano et al., 1989; Dahlburg & Picone, 1989; Picone & Dahlburg, 1991; Politano et al., 1995; Grauer & Marliani, 2000; Mininni et al., 2006; Parashar et al., 2009, 2014). It is given by

$$\delta\mathbf{u} = \delta u[-\sin(k_\perp y)\hat{\mathbf{x}} + \sin(k_\perp x)\hat{\mathbf{y}}]$$

$$\delta\mathbf{B} = \delta B[-\sin(k_\perp y)\hat{\mathbf{x}} + \sin(2k_\perp x)\hat{\mathbf{y}}],$$

where $\delta u = \delta B/\sqrt{4\pi\rho_0}$, $\delta\mathbf{u}$ and $\delta\mathbf{B}$ are perturbations in the ion and electron bulk flow and the magnetic field, and $k_\perp = 2\pi/L_\perp$ are positive constants.

To follow the turbulent cascade from the inertial range ($k_\perp\rho_i \ll 1$) to below electron scales ($k_\perp\rho_e > 1$) (TenBarge et al., 2013; TenBarge & Howes, 2013; TenBarge et al., 2014), we specify a reduced mass ratio, $m_i/m_e = 25$, which, in a simulation domain of $L_\perp = 8\pi\rho_i$ and dimensions $(n_x, n_y, n_z, n_\lambda, n_\varepsilon, n_s) = (128, 128, 2, 64, 32, 2)$, enables us to resolve a dynamic range of $0.25 \leq k_\perp\rho_i \leq 10.5$, or $0.05 \leq k_\perp\rho_e \leq 2.1$. Plasma parameters are ion plasma $\beta_i = 8\pi n_i T_{0i}/B_0^2 = 0.01$ and $T_{0i}/T_{0e} = 1$. Collision frequencies of $\nu_i = 10^{-5}\omega_{A0}$ and $\nu_e = 0.05\,\omega_{A0}$ (where $\omega_{A0} \equiv k_\parallel v_A$ is a characteristic Alfvén wave frequency in 3D) are sufficient to keep velocity space well resolved (Howes et al., 2008, 2011). Length, time and velocity

are normalized to the ion gyroradius $\rho_i \equiv v_{ti}/\Omega_{ci}$, where $\Omega_{ci} \equiv eB_0/m_i c$, domain turnaround time $\tau_0 \equiv L_\perp/\delta u$ and electron thermal speed $v_{te} \equiv \sqrt{2T_{0e}/m_e}$. τ_0 can be converted to the inverse ion gyro-frequency, a relevant time scale for reconnection, by $\tau_0 = 25\ \Omega_{ci}^{-1}$. The divergence of velocity is normalized to $v_{te}/\rho_e = \Omega_{ce}$.

2.3.5 Results

Figure 2.7(a) shows the out-of-plane current density J_z (color) and contours of the parallel vector potential $A_\parallel$ representing magnetic field lines of the OTV at an early time of t/τ_0=0.12. The OTV has an initial flow configuration that rotates the two vortices near the center of the domain, separated by a current sheet. The symmetry of the two vortices allows symmetric reconnection to take place at the current sheet. The flows also drive two asymmetric vortices at the top right and bottom left, resulting in two mirroring asymmetric reconnection X-points by symmetry of the system. A fourth reconnection X-point, which is a mirror of the central symmetric reconnection X-point, is located at $(x, y) \simeq$(0,12.6). The central symmetric (X1) and top-right asymmetric (X2) X-points are two of the cases we will discuss in detail.

As the total turbulence energy dissipates over time (Li et al., 2016), the driving of reconnection weakens and reconnection at later times is generally weaker than early-time events. Figure 2.7(c) shows J_z at late time t/τ_0=1.48 when multiscale features, including small-scale current sheets, have developed. A turbulent cascade in the dissipation range (see Figure 2.8 for the magnetic energy spectrum) is also developed. At the same time, an asymmetric reconnection X-point forms at the bottom left. This X-point (X3) does not develop bi-directional electron outflow jets and therefore cannot be identified through electron flows. Below we discuss the application of MFT and the identification of each reconnection X-point.

Figure 2.7(b) shows the x-component of the MFT velocity, $U_{\psi x}$, of the whole domain at t/τ_0=0.12, showing X1 and X2 as well as their mirrors, and (d) at t/τ_0=1.48, showing X3, its mirror and a reconnection X-point (X4) formed at the center of an evolved, elongated vortex (flux tube). The factor of δB_p^{-1} in the definition of $\mathbf{U}_\psi$ could tend to infinity at the X- and O-points where δB_p vanishes. As a practical step, we add a 1% offset to δB_p everywhere so
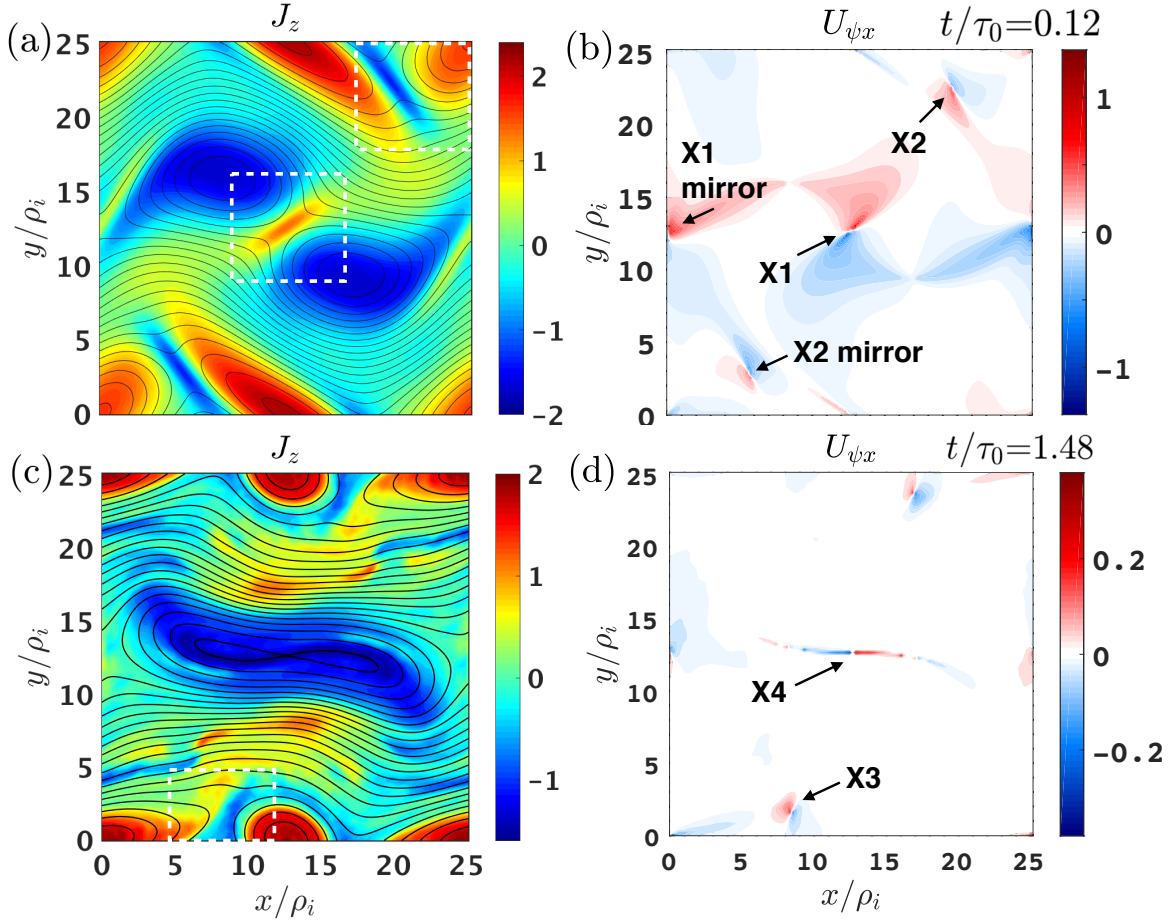
Figure 2.7: (a) The out-of-plane current density J_z (color) overlaid with contours of $A_\parallel$ of the OTV configuration, and (b) the x-component of $\mathbf{U}_\psi$ at t/τ_0=0.12, showing X1 and X2 and their mirrors (labeled). At t/τ_0=1.48, (c) J_z showing developed turbulence and (d) $U_{\psi x}$ revealing X3, X4 (labeled) and X3 mirror. The bi-directional outflows of magnetic flux at X1 and X4, and inflows at X2 and X3 are observed. δB_p is offset by adding a 1% of its maximum value in the domain such that $\mathbf{U}_\psi$ remains finite at the X- and O-points that have vanishing δB_p. This does not qualitatively affect the profile of $\mathbf{U}_\psi$. Dashed boxes indicate regions in zoomed-in figures. See an animation of J_z online. The animation lasts for t/τ_0=0–2.01. It shows the evolution of reconnection driven by turbulent flows.

that $\mathbf{U}_\psi$ remains finite at the X- and O-points that have vanishing δB_p. For the range of 0.01–4% offsets, the amplitudes of $\mathbf{U}_\psi$ and $\nabla \cdot \mathbf{U}_\psi$ only vary by a factor of 2. We mask the X-points by a grid point of size ρ_e which yields similar amplitudes to applying a 1% δB_p
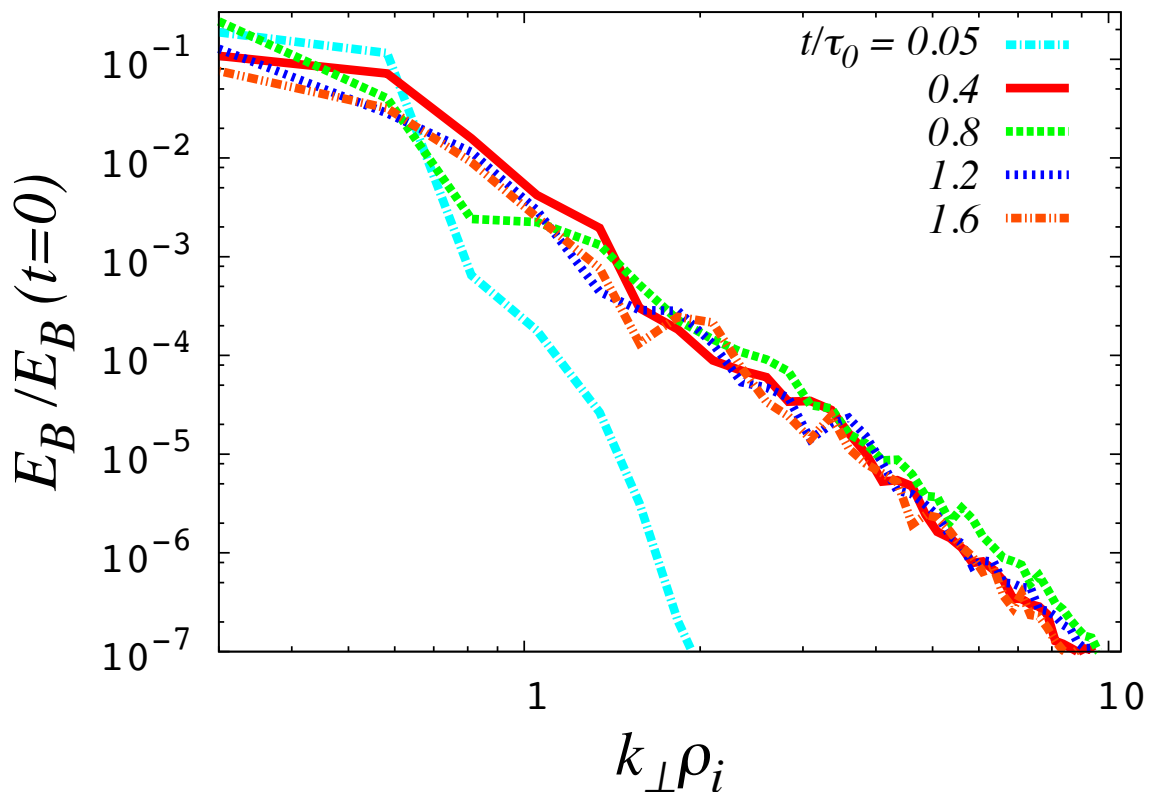
Figure 2.8: Evolution of the magnetic energy spectrum as a function of scale, showing a developed turbulent cascade in the dissipation range.

offset. Below we zoom in to X1–X3 to investigate the X-points more thoroughly.

2.3.5.1 Symmetric Reconnection X-point: X1

Figure 2.9 shows (a) vectors of $\mathbf{U}_\psi$, (b) $\nabla \cdot \mathbf{U}_\psi$, and for comparison, (c) vectors and (d) the divergence of $\delta\mathbf{u_e}$ in a zoomed-in region around X1. Clear bi-directional outflows and converging inflows of magnetic flux around X1 are captured in $\mathbf{U}_\psi$. (b) $\nabla\cdot\mathbf{U}_\psi$ reveals negative (blue) and positive (red) amplitudes highly localized to X1, representing converging inward and diverging outward MFT at the X-point. This is the inherent flux transport pattern of reconnection. It results in a new quadrupolar structure in $\nabla\cdot\mathbf{U}_\psi$. The quadrupolar structure reflects the bi-directional flux transport at the two sides upstream and downstream of the
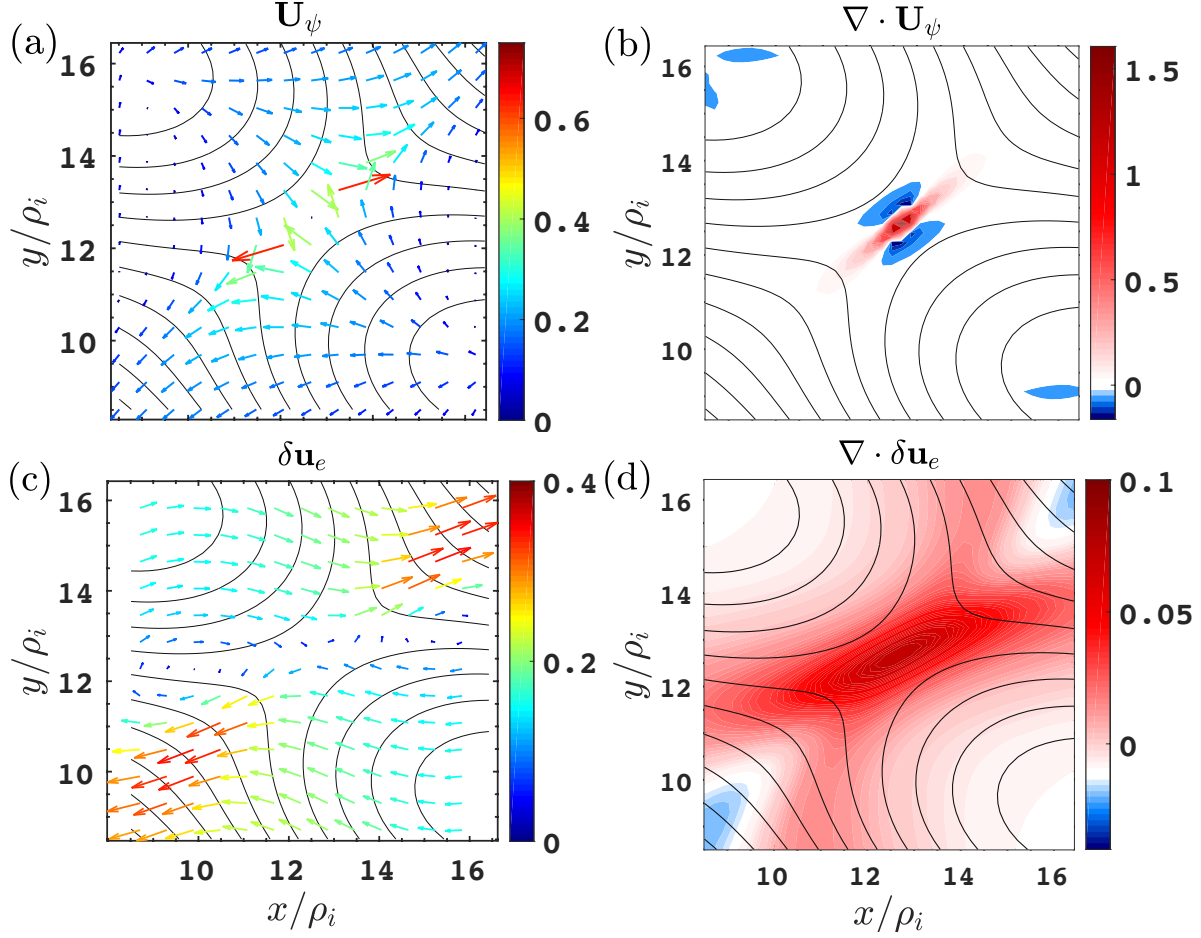
Figure 2.9: Application of the MFT method to X1, a symmetric reconnection X-point. Plotted quantities are (a) vectors of $\mathbf{U}_\psi$, (b) the divergence of $\mathbf{U}_\psi$, (c) vectors of the fluctuating in-plane electron flow velocity $\delta\mathbf{u}_e$, and (d) the divergence of $\delta\mathbf{u}_e$, overlaid with $A_\parallel$ contours. The amplitudes of vectors are denoted by the color and relative length of the arrows. The divergence of velocity is normalized to v_{te}/ρ_e.

X-point. Both quantities are highly localized to the X-point and can serve as local signatures of reconnection.

Bi-directional electron outflow jets in the outflow region can be seen in (c) $\delta\mathbf{u_e}$. (d) $\nabla\cdot\delta\mathbf{u}_e$ reveals positive amplitude, representing the diverging outflows. In comparison to $\mathbf{U}_\psi$, the electron outflow develops further from the X-point and over a much broader region.

2.3.5.2 Asymmetric Reconnection X-point: X2
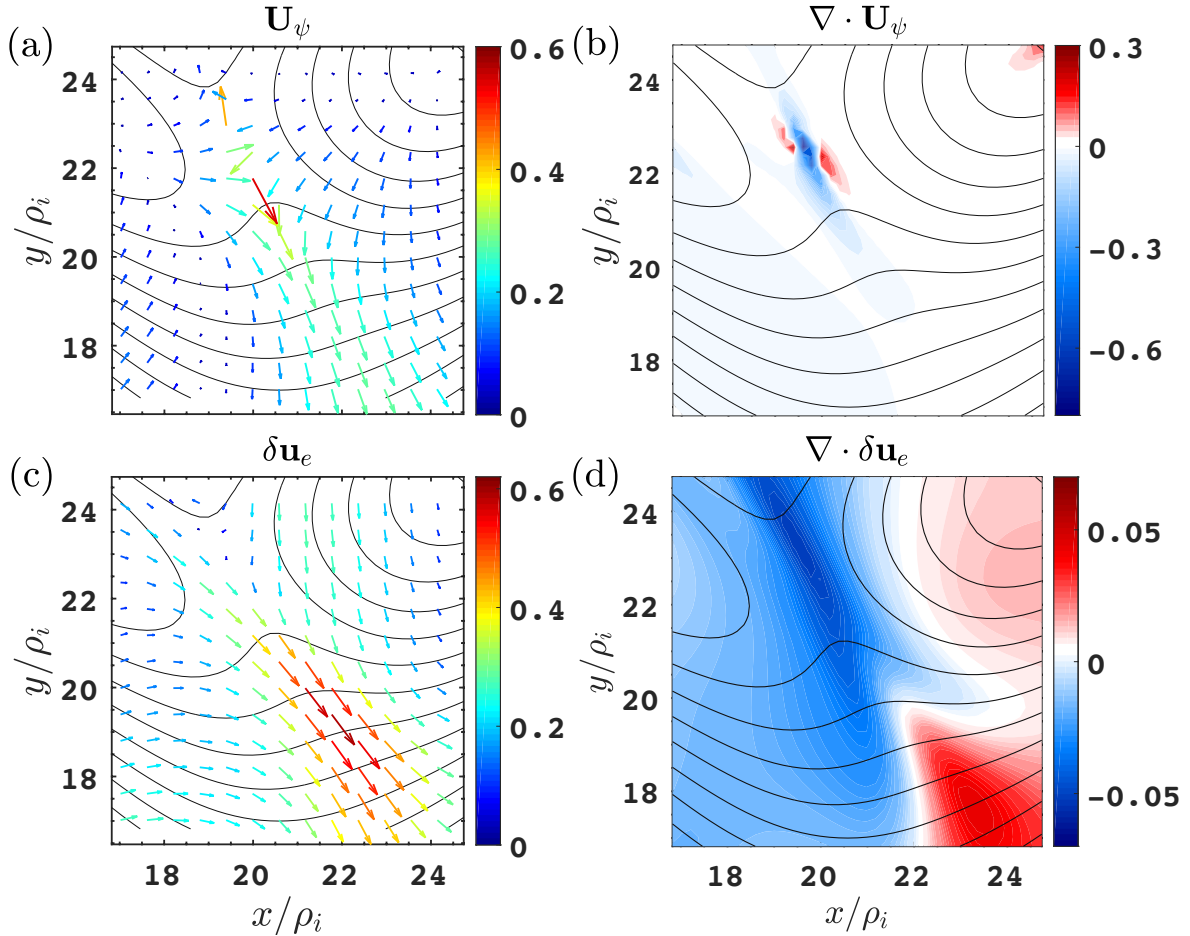
Figure 2.10: Application of the MFT method to X2, an asymmetric reconnection X-point. Same quantities as Figure 2.9 plotted for X2, an asymmetric reconnection X-point.

The same quantities as Figure 2.9 are plotted around X2 in Figure 2.10. Similarly, clear bi-directional inflows and asymmetric bi-directional outflows of magnetic flux are captured in (a) $\mathbf{U}_\psi$, with the downward transport being stronger. (b) $\nabla \cdot \mathbf{U}_\psi$ reveals the presence of converging inward and diverging outward flux transport as $\nabla \cdot \mathbf{U}_\psi < 0$ and > 0, respectively, at X2. Both signify active reconnection.

In (c) $\delta\mathbf{u_e}$, asymmetric electron outflow jets are seen, with a stronger downward jet from X2. (d) The divergence of the electron flow reveals negative and positive amplitudes located broadly around and downstream from the X-point, representing converging inflows

and diverging outflows of electrons at this X-point.

2.3.5.3   Reconnection X-point without Bidirectional Plasma Jets: X3
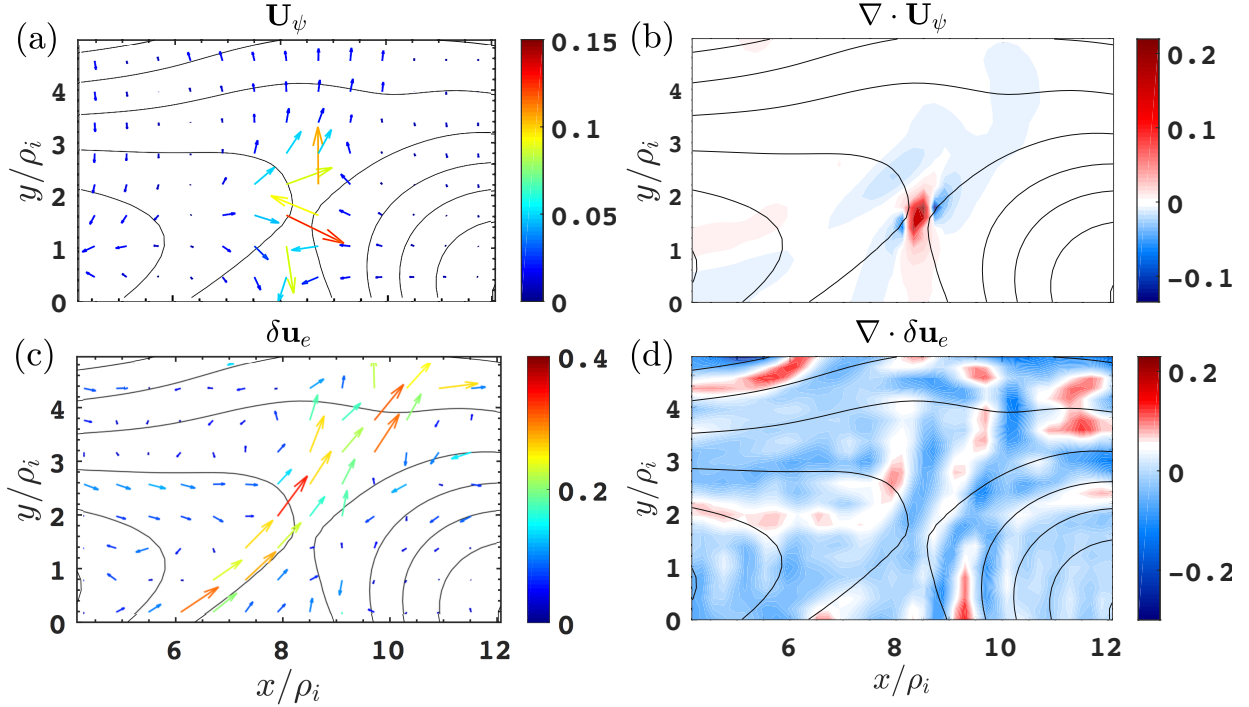
Figure 2.11: Application of the MFT method to X3, a reconnection X-point with only one outflow jet in electrons (and ions) at $t/\tau_0 = 1.48$. Velocity vectors are measured at the X-point frame. Same format as Figure 2.9 plotted for X3. Velocity vectors are measured at the X-point frame.

The turbulent flows that drive reconnection are significantly dissipated at late times (Li et al., 2016) and reconnection activity becomes weaker. Nevertheless, converging inflows and bi-directional outflows of magnetic flux are captured in Figure 2.11(a) $\mathbf{U}_\psi$ at X3. (b) $\nabla \cdot \mathbf{U}_\psi$ also reveals positive and negative amplitudes highly localized to the X-point, sharing a similar quadrupolar structure to X2 and X1.

On the other hand, the electron flow is highly modified by turbulence. No clear bi-directional outflow jets are seen in the electrons (or in the ions (Appendix Figure 2.12)) at
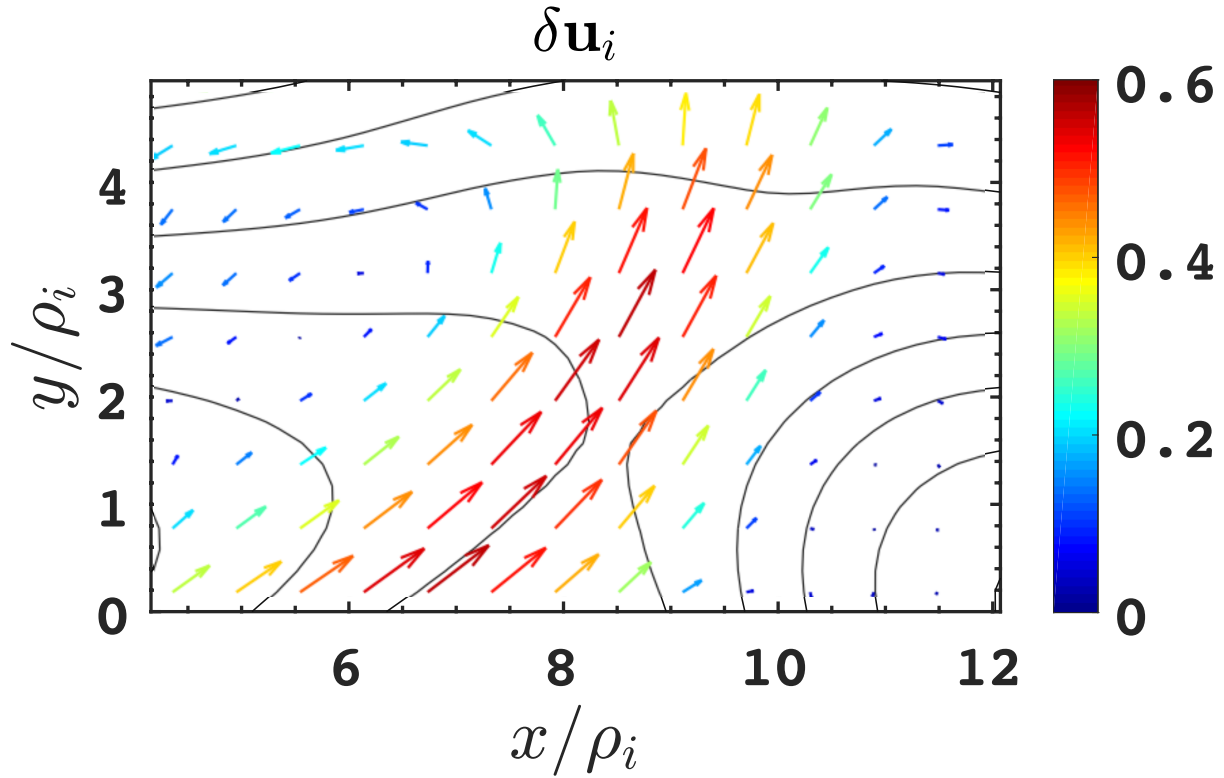
Figure 2.12: Ion flow velocity $\delta \mathbf{u}_i$ for X3, showing one outflow jet in ions. Compare with the electron flow velocity in Figure 2.11(c). $\delta \mathbf{u}_i$ is normalized to the ion thermal speed v_{ti}.

X3. Only one electron and one ion outflow jet are present. (d) $\nabla \cdot \delta \mathbf{u}_e$ also does not show clear evidence of reconnection. Plasma flows cannot be used for identifying reconnection at this X-point. However, the MFT method can identify reconnection through its clear inward and outward flux transport at this X-point, demonstrating the sensitivity of MFT in identifying reconnection activity in turbulence.

2.3.5.4 Super Alfvénic $\mathbf{U}_\psi$

While $\mathbf{U}_\psi$ is normalized to v_{te}, it is meaningful to compare it with the upstream Alfvén speed. Using the electron plasma $\beta_e \equiv (v_{te}/c_{Ae})^2 = 0.01$, where $c_{Ae} = \sqrt{B_0/4\pi n_0 m_e}$, in the simulation, and estimates of the upstream $\delta B_p/B_0 \sim 0.1$ and density $n/n_0 \sim 0.7$–1.1 for the three X-points, we can relate the upstream electron Alfvén speed (Cassak & Shay, 2007) to

51

v_{te} as $c_{Ae,p}/v_{te} \sim 1$. Therefore, at X1 and X2, U_ψ is of order $c_{Ae,p}$. The flux transport velocity is electron Alfvénic. Similarly, at X3, $U_\psi \sim 1.2\ c_{A,p}$ is super-Alfvénic. The higher velocity at early-time reconnection is associated with strong driving by initial turbulent flows. The Alfvénic velocity at late times is consistent with undriven reconnection simulations (Liu & Hesse, 2016). $\mathbf{U}_\psi$ is between orders $c_{A,p}$ and $c_{Ae,p}$ based on the simulation.

2.3.6 Divergence of MFT
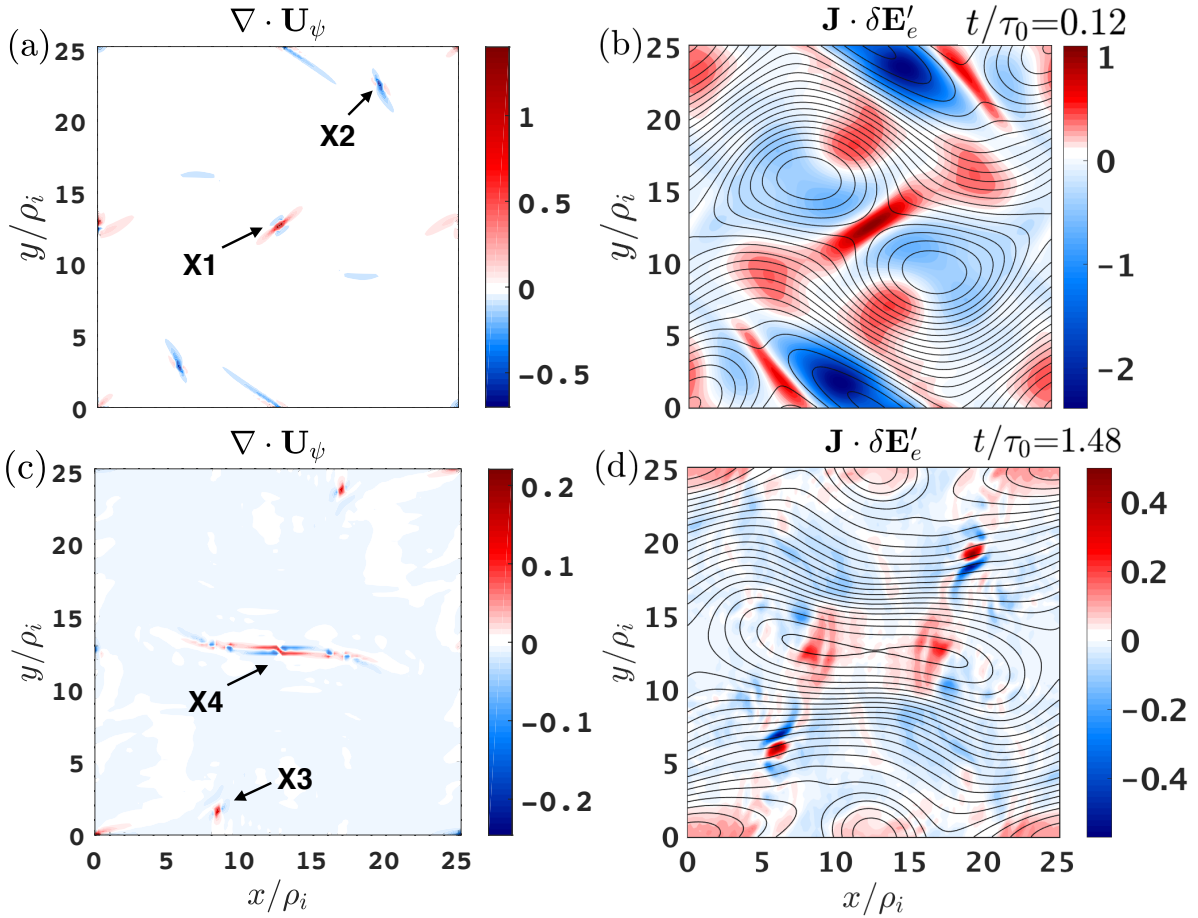
Figure 2.13: The divergence of MFT of the whole domain at (a) $t/\tau_0=0.12$, showing X1 and X2 (labeled) and their mirrors, and (c) $t/\tau_0=1.48$, showing X3 and X4 (labeled) among the turbulence; (b) and (d) $\mathbf{J} \cdot \delta\mathbf{E}'_e$, the non-ideal energy conversion in the electron frame, at the two times.

Plotted in Figure 2.13 is the divergence of MFT of the whole domain at (a) t/τ_0=0.12, showing X1 and X2 and their mirrors, and at (c) t/τ_0=1.48, when turbulence is developed, revealing X3 and X4. $\nabla \cdot \mathbf{U}_\psi$ shows significant amplitudes only at the active reconnection X-points, even among the turbulence. It remains small throughout the domain, and is thus suitable for the identification of reconnecting X-points in turbulence. $\nabla \cdot \delta\mathbf{u}_e$ is much more structured throughout the system, and at late times, becomes highly turbulent (not shown). For comparison, (b) $\mathbf{J} \cdot \delta\mathbf{E}'_e$, energy conversion (Zenitani et al., 2011) in the electron frame, is much more broadly distributed over the current sheets and throughout the system. (d) At late times, it is dominated by turbulent flows far away from the reconnection X-points, and thus may not help in locating reconnection in turbulence. The amplitude of $\nabla \cdot \mathbf{U}_\psi$ is of order 0.1–1 Ω_{ce} at the three reconnection X-points.

2.3.7 Discussion, Application, and Conclusion

The flux transport velocity has been generally considered as the E×B drift velocity. In Equation (2.5), the slippage between magnetic flux and electron flow arising from a non-ideal electric field $\mathbf{E}'_e$ is included. For the three reconnection X-points, the slippage provides the major contribution to the inflows and outflows of magnetic flux near the X-point, being ~2–3 times larger than the perpendicular electron flow. Further away from the X-point where the slippage becomes small, $\mathbf{U}_\psi$ follows the perpendicular electron flow, which is mainly the E×B drift.

$\nabla \cdot \mathbf{U}_\psi$ consistently shows a quadrupolar structure at all reconnection X-points in turbulence. However, a signal is possible at O-points, where magnetic flux annihilation could happen. This process is recently explored by MMS (Hasegawa et al., 2020). MFT activity at O-points deserves future investigation.

A new category of reconnection in turbulence beyond electron-only reconnection (Phan et al., 2018) is revealed by X3. Only a single electron Alfvénic electron jet and Alfvénic ion jet are observed at X3. This category has $\mathbf{U}_\psi$ reversals, but no plasma outflow jet reversal. Electron-only reconnection with only one jet is also reported in simulations of shock-driven

turbulence (Bessho et al., 2020).

Application of the MFT method to heliospheric plasmas requires the following conditions: (i) $k_\parallel \ll k_\perp$, where "$\parallel$" is along the background magnetic field, and (ii) the reconnection magnetic fields primarily reside on a local reconnection plane. $k_\parallel \ll k_\perp$ is based on $k_\parallel/k_\perp \ll \delta E_\parallel/\delta E_\perp$ for deriving $\partial_t \psi$ (§2.3.2), a condition well satisfied in the simulation. Equation (2.5) is then a good approximation of $\mathbf{U}_\psi$ even in 3D systems. Physically, this represents quasi-planar reconnection with parallel length scales much longer than perpendicular. $k_\parallel \ll k_\perp$ is well satisfied in the cascade of kinetic Alfvén wave turbulence (Cho & Lazarian, 2004; Schekochihin et al., 2009), which is consistent with solar wind and magnetosheath observations (Alexandrova et al., 2008, 2009; Sahraoui et al., 2013; Chen et al., 2016, 2017). The model of planar reconnection is adopted by the local current sheet (LMN) coordinate (Sonnerup & Cahill, 1967), commonly used in space reconnection observations. Observations of reconnection in small-scale current sheets in the turbulent magnetosheath are consistent with this model (e.g. (Phan et al., 2018; Wilder et al., 2018)). Thus, the conditions for applying MFT are expected to be realistic for reconnection in heliospheric turbulence. Recent 3D PIC simulations further show that a long extended X-line, satisfying $k_\parallel \ll k_\perp$, easily arising in sub-ion-scale current sheets in 3D (Li et al., 2020), also favors reconnection activity (Liu et al., 2019; Huang et al., 2020).

The MFT method is a new way of identifying reconnection X-points in turbulent plasmas. It captures bi-directional inflows and outflows of magnetic flux at the X-points to signify reconnection, even without bi-directional plasma outflow jets. $\nabla \cdot \mathbf{U}_\psi$ is suitable for use in multi-spacecraft missions such as MMS. The first application to a 2D gyrokinetic turbulence simulation demonstrates the capability of this method in clearly capturing active reconnection signatures, as an inflow-outflow pattern or a quadrupolar structure in $\nabla \cdot \mathbf{U}_\psi$. It also reveals a new category of reconnection in turbulence beyond electron-only reconnection. This method has the potential to replace the plasma outflow jet reversal signature for reconnection. Applications to 3D simulations and heliospheric observations from spacecraft missions will present new opportunities to study the role of reconnection and identify new

types of reconnection in turbulence.

2.4 Magnetic Flux Transport: Observations

2.4.1 Introduction

The identification of active reconnection has been challenging. With the high-resolution observations from MMS, we are able to see most of the above-mentioned signatures. However, these signatures may not be observed coherently. The trajectory of the spacecraft has a significant influence on the observational profile. In addition, asymmetry of upstream conditions (Shay et al., 2016), existence of finite guide fields (Bessho et al., 2019; Ng et al., 2011) and strong shear flows (Li et al., 2021; Liu et al., 2018) likely in a turbulent system may all distort the signatures, adding complexity to reconnection.

As we introduced in Section 2.3, recent studies (Hesse et al., 2016; Liu & Hesse, 2016) have analyzed the transport of magnetic flux around an X-point in kinetic simulations. The Magnetic Flux Transport (MFT) technique has been developed and carefully analyzed in a two-dimensional gyrokinetic simulation (Li et al., 2021) where MFT was applied to both symmetric and asymmetric reconnection X-point regions in turbulence generated by a double-vortex setup (Li et al., 2016). MFT successfully captures bidirectional inflows and outflows of magnetic flux around active X-points in a region significantly smaller than the region extended by particle outflow jets or finite energy conversion, i.e., the MFT method can locate the active reconnection sites more accurately than previous methods. In addition, they also found that although strong background shear flows distort the bidirectional particle outflow jets, the velocity of magnetic flux transport U_ψ maintains its regular pattern, demonstrating that the MFT method is more robust than previous methods. Quadrupolar structures are observed in $\nabla \cdot U_\psi$ at the X-points, supporting the active reconnection picture. Based on these numerical modeling results, MFT has the potential to be a more accurate indicator of active reconnection. The present study applies this newly developed technique to MMS in-situ observations and validates its functionality in various plasma conditions.

In the following sections, we examine the MFT process in 37 previously reported EDR/reconnection-line crossing events at the dayside magnetopause, in the magnetotail and magnetosheath using Magnetospheric Multiscale (MMS) measurements. The co-existing inward and outward MFT flow at the X-point provides a signature that magnetic field lines become disconnected and reconnected. The application of MFT analysis to in-situ observations demonstrates that MFT can successfully identify active reconnection sites under symmetric, asymmetric, and turbulent upstream conditions, providing a higher rate of successful identification than relying on plasma outflow jets alone.

2.4.2   Data

The data used herein is obtained by the MMS mission. This mission is designed to capture the elusively thin and fast-moving diffusion regions of reconnection with unprecedented time resolution (Burch et al., 2015). The orbits cover the most common reconnection locations on both the dayside and nightside of the Earth's magnetosphere, a natural laboratory for in-situ observations of reconnection. Four identical spacecraft form a tetrahedron configuration with spacecraft separation varying from ∼10 to 150 km which provides spatial resolution down to the particle kinetic scale (Fuselier et al., 2016). The magnetic field is measured by the fluxgate magnetometer (FGM) (Russell et al., 2014) at its highest sampling rate of 128 Hz. The fast plasma investigation (FPI) instruments (Pollock et al., 2016) provide the electron/ion distribution functions and moments every 30/150 ms in burst mode, covering the energy range from 10 eV to 30 keV.

We select previously identified EDR or the reconnection line crossing events to represent the different environments where reconnection happens near Earth. The events include reconnection in the turbulent shock transition region (Wang et al., 2019), magnetosheath (Eriksson et al., 2018; Phan et al., 2018), dayside magnetopause (Burch et al., 2016; Burch & Phan, 2016; Khotyaintsev et al., 2016), magnetotail (Lu et al., 2020b; Torbert et al., 2018; Zhou et al., 2019), and a list of EDRs reported by Webster et al. (2018).

Although the selected events are not a complete survey of all possible reconnection condi-

Date and time	Location	Guide field	Type	Reference
2015-10-16 13:07:02	dayside	~ 0	Classic	Burch et al. 2016
2015-12-08 11:20:43	dayside	~ 1	Classic	Burch & Phan 2016
2015-12-06 23:38:31	dayside	~ 0.2	Classic	Khotyaintsev et al. 2016
2015-10-25 11:07:46	sheath	~ 0.5	Classic	Eriksson et al. 2018
2016-12-09 09:03:54	sheath	> 5	Electron-only	Phan et al. 2018
2016-11-09 13:39:26	Shock transition region	~ 0	Classic	Wang et al. 2019
2017-07-11 22:34:02	Tail	~ 0	Classic	Torbert et al. 2018
2017-06-17 20:24:07	Tail	~ 0	Electron-only	Lu et al. 2020
2017-08-10 12:18:33	Tail	~ 0.13	Classic	Zhou et al. 2019
31 EDRs	Dayside	varying	Classic	Webster et al. 2018

Table 2.1: Case studies of EDR/reconnection-line crossing.

tions, they are sufficiently typical, representing symmetric and asymmetric upstream conditions, varying guide field strength, quiet and turbulent regions, as well as classic ion-coupled reconnection and newly discovered electron-only reconnection. Requiring events with four spacecraft measurements, we exclude the January 2, 2017 EDR event when MMS3 was not available. We also note the three case studies partly overlap with the 32 EDRs (Webster et al. 2018). In total we apply the MFT analysis to 37 events, listed in Table 2.1.

To apply this technique to observations by MMS and other spacecraft missions, it is necessary to validate it with known events and this study does that. With the 37 events of varied plasma conditions, we find this technique robust enough for identifying reconnection.

2.4.3 Method

The MFT velocity $\mathbf{U}_\psi$ was previously derived in one and two dimensions (Liu & Hesse, 2016; Liu et al., 2018). The formula for this velocity is:

$$\mathbf{U}_\psi \equiv \mathbf{v}_{ep} - (\mathbf{v}_{ep} \cdot \hat{b}_p)\hat{b}_p + \frac{cE'_{ez}}{B_p}(\hat{\mathbf{z}} \times \hat{b}_p), \qquad (2.7)$$

where $\hat{b}_p = \mathbf{B_p}/B_p$ is the unit vector of the magnetic field component ($\mathbf{B_p}$) in the 2D reconnection plane, the LN plane in LMN coordinates, and $\mathbf{v_{ep}}$ is the electron flow in the reconnection 2D plane. $\mathbf{E}'_e = \mathbf{E}_e + \mathbf{v}_e \times \mathbf{B}$, where $\mathbf{E}'_e$ is the nonideal electric field in the electron frame. The first two terms represent the in-plane electron flow perpendicular to $\mathbf{B}_p$. They come from the $\mathbf{v}_e \times \mathbf{B}$ term in the electron momentum equation. The last term represents the slippage between the magnetic flux and electron flow due to the non-ideal electric field. According to simulation work (Li et al. 2021), $\mathbf{U}_\psi$ will form super ion alfvenic jets in both inflow (N) and outflow (L) directions, indicating strong magnetic flux transport close to the active X-point. The upstream Alfven speed V_A is calculated as in Cassak et al. (2007) . For events with strong background flow, we subtract the ion bulk flow velocity from U_ψ to more accurately demonstrate the MFT jets in the frame of the current sheet.

With four spacecraft measurements, we can estimate the divergence of the magnetic flux transport velocity $\nabla \cdot \mathbf{U}_\psi$ following the linear gradient technique (Chanteur, 1998). This quantity is able to represent the converging inflows and diverging outflows of magnetic flux. In addition to the signature in $\mathbf{U}_\psi$, these bidirectional inflows and outflows of magnetic flux at an X-point signify active reconnection.

For events from Webster et al. (2018) we apply the Minimum Variance Analysis (MVA) technique (Sonnerup & Cahill, 1967) on the magnetic field in the interval around the recorded EDR crossings to determine the boundary normal coordinate (LMN). The maximum variance direction (L) aligns with the reconnecting field direction and corresponds to the expected outflow direction. The minimum variance direction (N) gives the normal of the reconnecting current sheet or the expected inflow direction. The intermediate variance direction (M) is the out-of-plane direction, along which the magnetic field component is considered the guide field. For other events, we use the original coordinate rotation matrices to convert data to the LMN coordinates. MFT only depends on simple quantities, the electric and magnetic fields. Optimally transforming the field data to the LMN coordinate will be essential to the accuracy of MFT in identifying active reconnection.

There are two signatures of active reconnection in MFT analysis. They are: 1) the co-

existing magnetic flux ($\mathbf{U}_\psi$) jets in outflow (L)/inflow (N) directions, and 2) a significantly enhanced divergence of flux transport ($\nabla \cdot \mathbf{U}_\psi$) at the X-point. Previously theory and simulation work suggests the jet peak value to be at least ion Alfvenic ($\gtrsim 0.5 V_A$), and the divergence peak value at the order of 0.1 electron cyclotron frequency ($\nabla \cdot \mathbf{U}_\psi \gtrsim 0.05\Omega_e$) or higher (Li et al., 2021). Observing either signature indicates an encounter of an active reconnection site. For each event, we select a region of interest around the EDR/reconnection-line crossing such that the radius of the field line curvature R_c becomes comparable to or smaller than the ion gyro-radius, indicating agyrotropic or chaotic ion motions indicative of the IDR (Rogers et al., 2019). Within the selected region, we record the peaks of $\mathbf{U}_\psi$ and $\nabla \cdot \mathbf{U}_\psi$.

2.4.4 Results

2.4.4.1 Example of a successfully identified reconnection site

As an example of MFT signatures in MMS data, we summarize in Figure 2.14 the analysis of an active reconnection event in the magnetosheath reported by Eriksson et al. (2018). At the reversal of the magnetic field L component (a), the magnetic curvature increases and Rc reaches the electron kinetic scale. The MFT velocity demonstrates a bipolar signature in the N direction (blue, (g)) and a unipolar peak in L (red). Both peaks exceed the upstream Alfven speed V_A (horizontal dashed line). These bidirectional MFT inflows and unidirectional outflow are consistent with (i) the deduced spacecraft trajectory of MMS crossing the actively reconnecting current sheet from upstream to downstream and then back to upstream on the other side. (h) The bipolar structure in $\nabla \cdot \mathbf{U}_\psi$ is consistent with converging MFT inflows and diverging outflows near the X-point, with a peak value exceeding order 0.1 Ω_e. The observed MFT signatures agree well with simulation.

We plot the L and N component of $\mathbf{U}_\psi$ on each spacecraft in Figure 2.15. The patterns of the velocity are similar on all spacecraft, suggesting the scale of the structure is greater than the spacecraft separation. Thus, MMS resolves the structure of $\mathbf{U}_\psi$. MMS4 and MMS2 detect the two strongest peaks in the L-component, in agreement with the X-point being
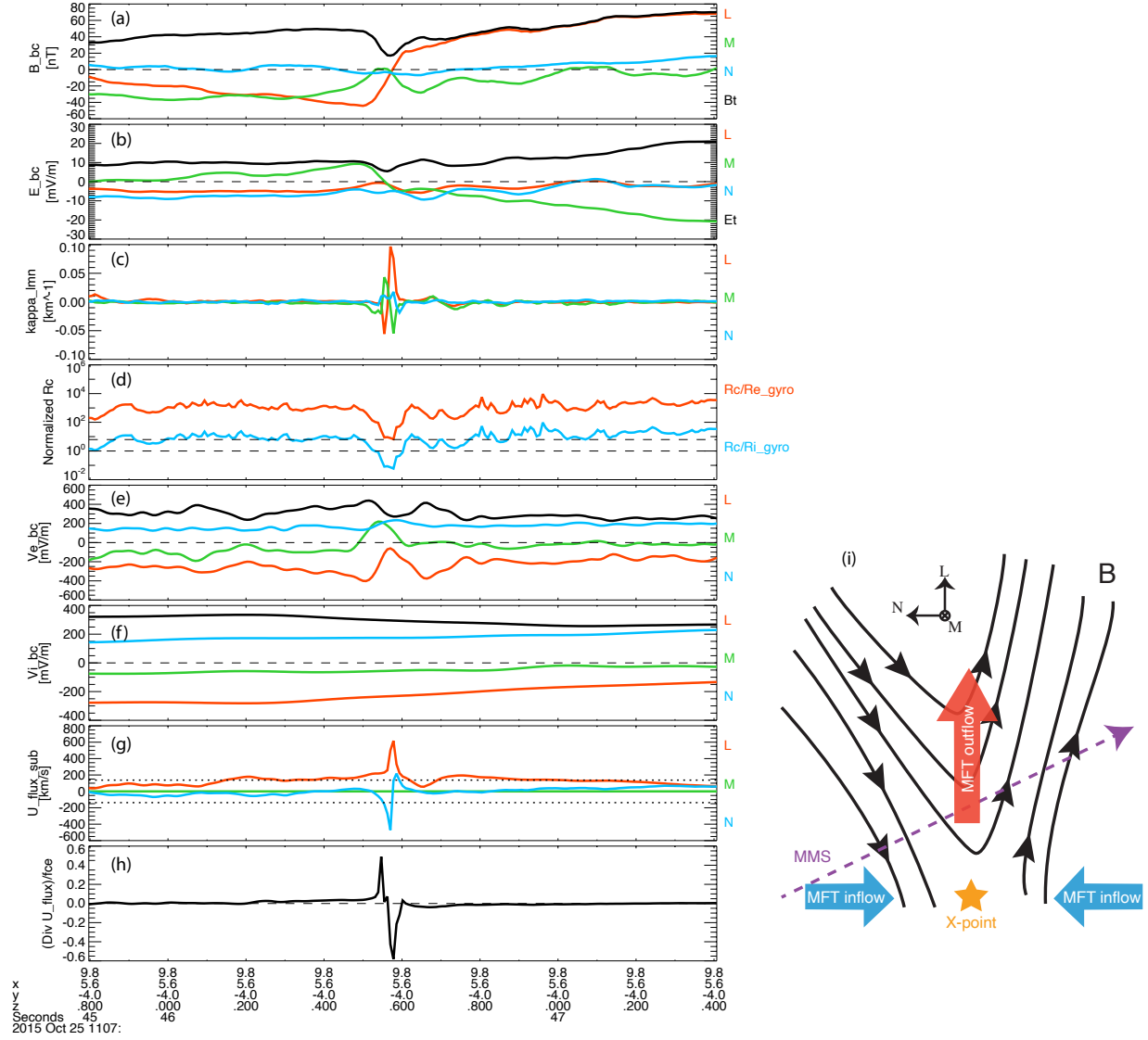
Figure 2.14: MMS observations of an example event on Oct 25, 2015. Vectors are transformed in LMN coordinates (L = [0.31, -0.91, 0.28], M = [0.31, 0.37, 0.87], N=[-0.90, -0.19, 0.40] in GSE). Four-spacecraft-averaged (a) magnetic field and (b) electric field. (c) Magnetic curvature.. The horizontal dashed lines correspond to 2.52 and 1. (d) Radius of curvature Rc normalized to the electron (red) and ion (blue) gyro-radius. (e-f) Electron and ion bulk flow velocity. (g) The velocity of magnetic flux transport $\mathbf{U}_\psi$. (h) $\nabla \cdot \mathbf{U}_\psi$ normalized to Ω_e (i) Sketch of MMS trajectory and expected MFT flows, adapted from Eriksson et al. (2018).

south of the spacecraft and MMS4 and MMS2 being the closest to it.
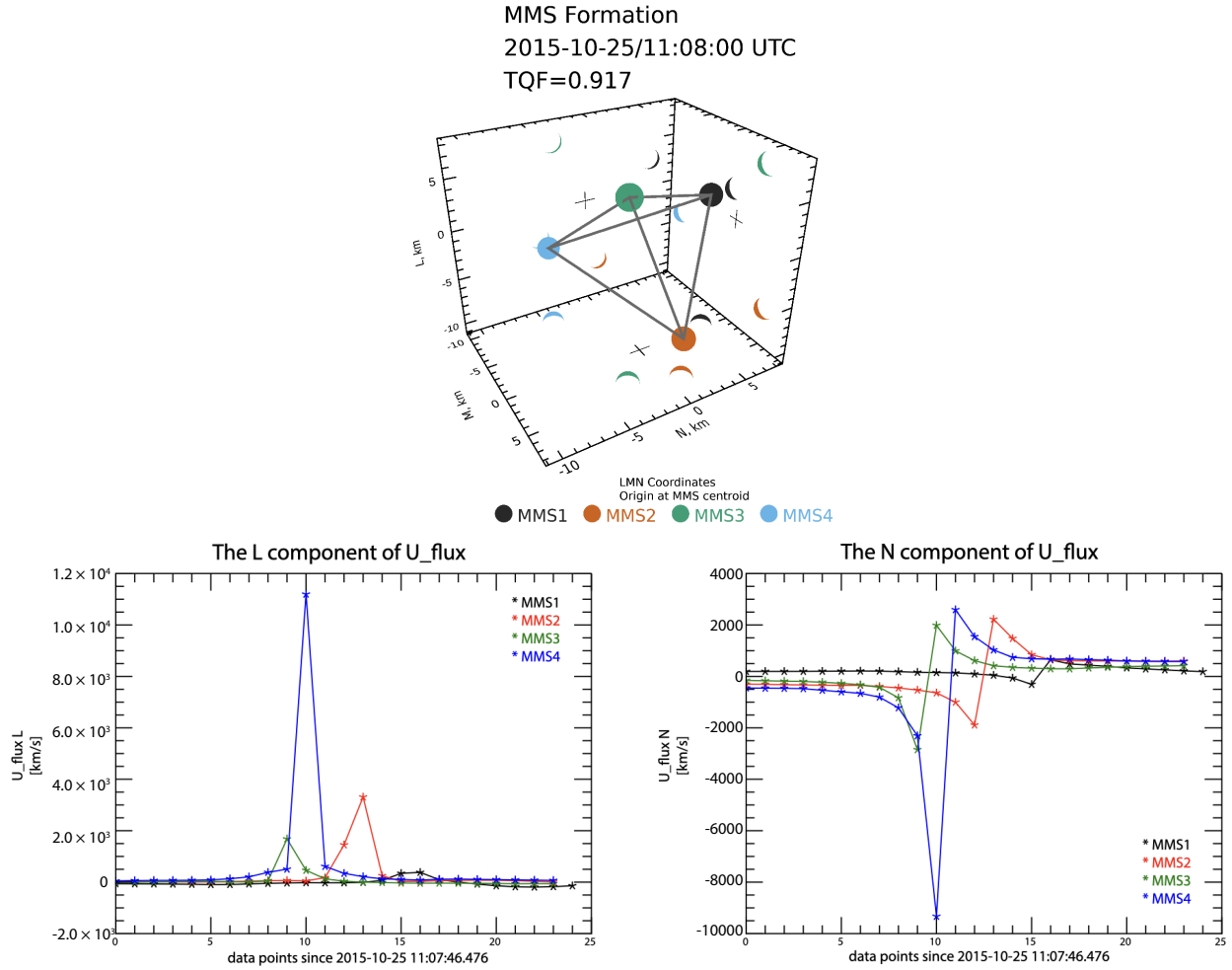
Figure 2.15: Configuration of four MMS spacecraft and MFT velocity on each spacecraft. (a) Spacecraft formation with the origin at the tetrahedron center.. (b) The L and (c) N components of $\mathbf{U}_\psi$ measured by four spacecraft. Data are plotted at every 0.0078 sec.

Applying the four-spacecraft timing technique (Russell et al. 1983) we find that the current sheet was mainly moving in the +N direction ([-0.03, -0.09, 0.99] in LMN). Thus, MMS4, having the smallest N coordinate, is the first to cross the current sheet, followed by MMS3, MMS2 and lastly MMS1. This order agrees with the sequence of the $\mathbf{U}_\psi$ peak. Assuming there is no temporal variation of the reconnection in this observing interval, with the trajectory plotted by Eriksson et al. (2018), the X-point is moving southward and away

61

from the spacecraft, in which case the spacecraft that encountered the current sheet first would be the closest to the X-point and record the strongest signature. We see this trend in Figure 2.15 as well.

2.4.4.2 Identification in 37 events

The same analysis is applied to all 37 events. Figure 2.16 summarizes the result on the peak values of (a) $\mathbf{U}_\psi$ jets, and (b) $\nabla \cdot \mathbf{U}_\psi$ for each event.

One of the two MFT signatures for active reconnection is co-existing alfvenic jets in the inflow and outflow directions. Figure 2.16 panel(a) shows the peaks of MFT jet in N (circles) and L (crosses) directions for all events. $\mathbf{U}_\psi$ is normalized to the upstream Alfven speed V_A. The shaded area is bounded by ± 1, above which the jets are super-Alfvenic. The dashed lines mark $\pm 0.5 V_A$, above which they are considered Alfvenic. Jets less than $0.5 V_A$ are masked. For almost all events MMS observed co-existing N and L jets, demonstrating both inflow and outflow MFT in these events. Only three events on December 09, 2016, January 10, 2016, and November 13, 2016 do not have this signature. The December 09, 2016 event was reported as electron-only reconnection (Phan et al., 2018). It has a scale small compared to the spacecraft separation. Instead of using the four-spacecraft-averaged value, we examine the MFT properties on each spacecraft,, Then co-existing Alfvenic inflow and outflow jets are correctly revealed. For the events on January 10, 2016 and November 13, 2016, the divergence of $\mathbf{U}_\psi$ is used and also identifies active reconnection (below).

The other MFT signature of active reconnection is the divergence of the $\mathbf{U}_\psi$ being of the order of 0.1 of the local electron cyclotron frequency Ω_e or higher. Plotted in Figure 2.16 (b) is $\nabla \cdot \mathbf{U}_\psi$ normalized to Ω_e. The dashed lines indicate $\pm 0.1 \Omega_e$. Values smaller than 0.05 are considered below order 0.1 Ω_e, and masked. Similarly, the MFT jets, for nearly all events, the peak $\nabla \cdot \mathbf{U}_\psi$ exceeds the threshold of $\mathcal{O}(0.1\Omega_e)$, confirming the presence of active reconnection encounter in these events.. The typically observed $\nabla \cdot \mathbf{U}_\psi$ lies within $\pm 0.5 \Omega_e$, consistent with the expected ordering. As discussed, events on January 10, 2016 and November 13, 2016, have a high enough divergence of $\mathbf{U}_\psi$ to be active reconnection. In total,
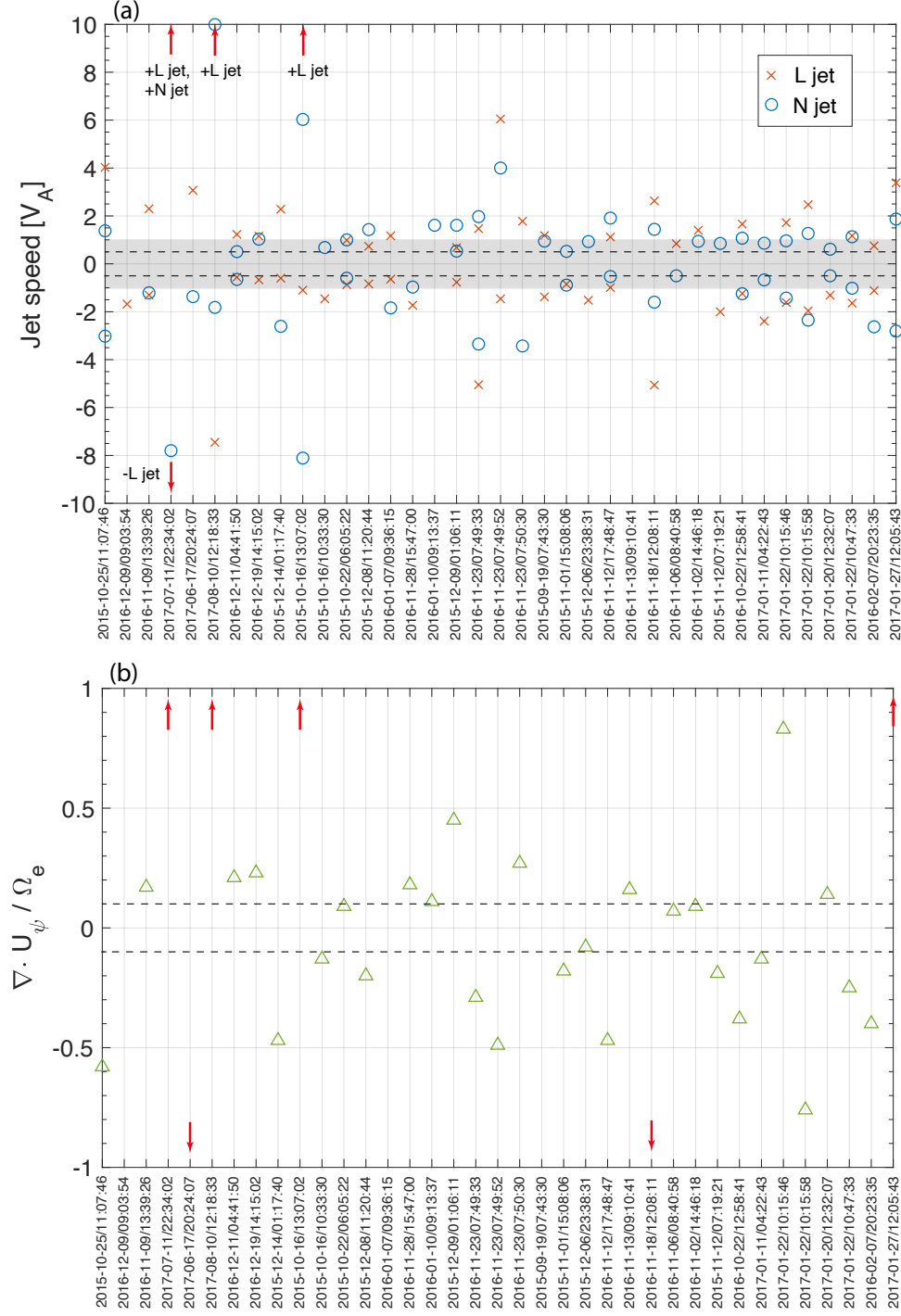
Figure 2.16: The peak values of (a) $\mathbf{U}_\psi$ in the L and N direction normalized to V_A and (b) $\nabla \cdot \mathbf{U}_\psi$ normalized to Ω_e. The red arrows indicate L or N jets out of the plotted range.

63

all 37 events were successfully identified as active reconnection through MFT signatures.

The median value of $+/-$ L jet peak is $1.17/-1.12$ V_A, and that of N jet peak is $0.95/-0.89$ V_A. These values indicate that typical MFT jets are Alfvenic or super-Alfvenic around the active reconnection site. The median absolute value of $\nabla \cdot \mathbf{U}_\psi$ is 0.23 Ω_e, also meeting the criteria of being order 0.1 Ω_e or higher.

2.4.5 Discussion

The two MFT properties that serve as active reconnection signatures are the co-existing Alfvenic inflow and outflow flux jet and a high divergence of flux transport velocity. As marked by the pink shadow in Table 2.2, these two properties are observed in 94.59% and 83.78% of all the events. Meeting either one of the two criteria will be sufficient for reconnection identification. In this case, all 37 events are successfully identified by MFT properties.

In Table 2.2 we also record additional MFT properties and their corresponding occurrence rate. As for the appearance of magnetic flux jet, we start from the property that is the easiest to detect or develop: the co-existing jets in both inflow and outflow direction, without any further requirements on the magnitude of the jets. The occurrence rate is the highest. When we keep adding requirements on the magnitude of the jets, the occurrence rates drop but remain higher than 85%. We then increase the numbers of jets to be at least three. The occurrence rate again drops when adding more requirements on the magnitude of the jets. The lowest rate is $\sim 84\%$ when we require at least one of the jets to be super-Alfvenic. As for the behavior of $\nabla \cdot \mathbf{U}_\psi$, we again start from requiring a certain number of poles in the $\nabla \cdot \mathbf{U}_\psi$ profile and then add more requirements on the magnitude. The occurrence rates for seeing two poles in $\nabla \cdot \mathbf{U}_\psi$ are still higher than 80%, while that for seeing three poles are generally lower (as low as 67%). It is understandable since observing at least three poles in $\nabla \cdot \mathbf{U}_\psi$ has relatively more strict limits on the MMS trajectory. It not only needs the spacecraft to cross at least 2 inflow regions and 1 outflow region or 2 outflow regions and 1 inflow region, but also remain close enough to the X-line during the whole crossing to measure large enough MFT signatures. Hence a relatively lower occurrence rate is expected.

Properties	Percentage
1 N & 1 L flux jets or more	97.30%
1N & 1L jets or more, and at least one Alfenic jet	94.59%
1N & 1L jets or more, and at least two Alfvenic jets	94.59%
1N & 1L jets or more, and at least one super-Alfvenic jet	89.19%
Three flux jets or more	91.89%
Three flux jets or more , and at least one Alfvenic jet	89.19%
Three flux jets or more, and at least one super-Alfvenic jet	83.78%
Two or more poles in $\nabla \cdot \mathbf{U}_\psi$	89.19%
Two or more poles in $\nabla \cdot \mathbf{U}_\psi$, and maximum amplitude of order 0.1 Ω_e or higher	83.78%
Three or more poles in $\nabla \cdot \mathbf{U}_\psi$	72.97%
Three or more poles in $\nabla \cdot \mathbf{U}_\psi$, and maximum amplitude order 0.1 Ω_e or higher	67.57%
At least one ion outflow jet	97.30%
At least one electron outflow jet	100.00%
bi-directional ion outflow jets	18.92%
bi-directional electron outflow jets	43.24%

Table 2.2: Occurrence rates of MFT properties and plasma outflow jets in the 37 events.

We also compared the MFT signatures with the ion and electron bulk flow velocity jets. To confidently identify reconnection line crossing using the plasma flow we usually need the flow to be bi-directional. Also the occurrence rates for bi-directional plasma outflow jets are lower than 50%. If we use the bi-directional outflow jets as the criteria for active reconnection crossing, it is very likely we will miss more than half of the events. If we use only one jet as the criteria, it is not confined as closely around the x-line as the MFT signatures (Li et al., 2021), and it is harder to establish a straightforward link between the observation of a single plasma jet and the reconnection.

The existence of a finite guide field will make the situation more complicated. It does not only modify the topology at the reconnection sites, but also possibly change the planar picture into a more turbulent three-dimensional scenario (Chen et al., 2020; Ng et al., 2011). Our database includes a variety of guide field strength and as mentioned earlier, regardless of the guide field strength, the MFT analysis successfully identified active reconnection. Thus we suggest the accuracy of MFT is robust in the presence of varying guide fields.

2.4.6   Conclusion

In this study, for the first time we have applied the newly developed Magnetic Flux Transport (MFT) technique to MMS data and show this technique can successfully identify active reconnection. The two MFT properties that are signatures of active reconnection encounter are the co-existing Alfvenic inflow and outflow flux jet and a high divergence of the flux transport velocity. The detection of either one is sufficient. We select 37 previously reported EDR/reconnection line crossing events on the Earth's dayside magnetopause, in the magnetotail and magnetosheath to test the functionality of MFT under various plasma conditions. All events are successfully identified with the two MFT properties. The median value of the magnetic flux transport velocity peak is typically Alfvenic and sufficient for locating the active reconnection region. The divergence of the flux transport velocity has a median absolute value of 0.23 Ω_e, consistent with the expected threshold for reconnection. The occurrence rates of these two properties are 95% and 84%, much higher success rates

compared to using bi-directional plasma outflow jets. This application of MFT to the terrestrial data confirmed its capability to identify reconnection under complex varied plasma conditions, motivating the application of this technique for analyzing reconnection in more heliospheric contexts such as the solar corona and solar wind turbulence.

CHAPTER 3

Magnetic entanglement

In this section, we present studies on the flux transfer events (FTEs) and magnetic entanglement process. In Section 3.1, we review the observation and generation mechanism of flux transfer events. We also introduce the previous study on flux tube interactions on the Sun. In Section 3.2[1], we explain the complexity of FTEs on the Earth's magnetopause and how magnetic entanglement could generate flux ropes in pairs. In Section 3.3[2], we further investigate the magnetic entanglement and identify three temporal evolutionary stages using MMS measurements. In Section 3.4[3], we utilize Hall MHD simulation to test the feasibility of magnetic entanglement and how magnetic reconnection at the entanglement interface simplify the geometry.

3.1 Flux Transfer Events, Flux Ropes and Flux Tubes

3.1.1 Flux Transfer Events on the Earth

Flux Transfer Events (FTEs) were first observed by the ISEE 1 and 2 spacecraft and were interpreted as generated by patchy and impulsive reconnection near the sub-solar point (Russell & Elphic, 1979). In 1977, the dual spacecraft International Sun-Earth Explorer mission was launched into a single, high-apogee orbit with a variable separation between the two spacecraft. One of its first discoveries was that near the Earth's magnetopause, there

---

[1]This section is a version of Russell & Qi (2020).

[2]This section is a version of Qi et al. (2020).

[3]This section is a version of Jia et al. (2021)

were detached (in the time domain) flux ropes (FRs). FRs are bundles of magnetic flux that are twisted about the central axis of the bundle so that the bundle is well defined and the outward pressure is balanced by the $\mathbf{j} \times \mathbf{B}$ force associated with the twisted field. These FRs often contained energetic electrons, signaling that they might be connected to the Earth's magnetosphere (Russell & Elphic, 1978).

Figure 3.1 shows the time series of the magnetic field at ISEE 1 and 2, for over an hour on 8 November 1977. At 0212 UT and 0236 UT, the spacecraft entered a strong field region similar in strength to that of the magnetic field in the magnetosphere after 0250 UT, but these fields had a quite different orientation. This transient feature was termed a flux transfer event (FTE) by the authors. It was postulated to be evidence of a FR that had become connected between the magnetosheath and the magnetosphere, convected away from the subsolar region and supposedly transferring that flux inventory of the magnetotail. These FRs were macroscopic structures containing up to about 20 mWb of magnetic flux, but FRs of much smaller size are also found in the higher-resolution MMS data (Russell et al., 2017).

Following the first discovery, other generation models were raised, including the multiple X-line model by Lee & Fu (1985), and the single X-line model (Scholer, 1988; Southwood et al., 1988). The different generation mechanisms may be associated with different upstream conditions and could result in different magnetic field topology and connectivity within/around the FTE (Dorelli & Bhattacharjee, 2009; Hesse et al., 1990; Hwang et al., 2020; Lu et al., 2020a) Despite differences in detail, reconnection plays an essential role in transferring magnetic flux. FTEs feature a bipolar B_N component in boundary normal coordinates associated with the twisted magnetic field. The field strength may increase in rope-like FTEs (Russell & Elphic, 1979), or decrease as in the possibly related phenomenon, a "crater FTE" whose generation can be explained in the single X-line model and shows signatures of separatrices at their borders (Farrugia et al., 2011; Trenchi et al., 2019).
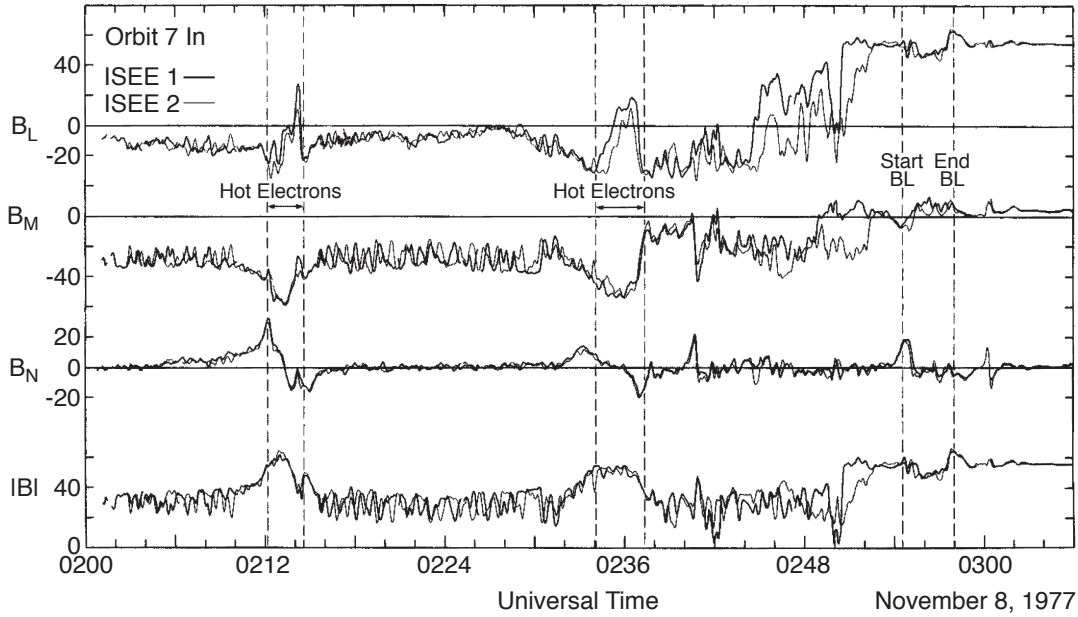
Figure 3.1: The time series of the magnetic field measurements by ISEE 1 that revealed magnetic field ropes at the Earth's magnetopause, when the interplanetary field was southward and showing that these ropes could contain energetic magnetospheric electrons. Adapted from Russell & Elphic (1979)

3.1.2 Flux Tube Interactions on the Sun and in the Solar Wind

Besides carrying magnetic flux into the magnetosphere, flux ropes are also an important structure of various eruptive phenomena in the solar atmosphere. The interaction between flux tubes in the solar corona has been proposed to trigger solar flares by the coalescence of two or more flux tubes which leads to magnetic reconnection at the interface (Frazier & Stenflo, 1972; Smartt et al., 1993). Figure 3.2 gives an example of the observed interaction between the arched magnetic flux tubes in the solar corona.

Massive efforts have been invested in understanding how the interaction between flux tubes works, and what kind of interaction could further result in reconnection in the solar flare. For example, in the study by Lau & Finn (1990), they set up a pair of flux ropes that are parallel or antiparallel to each other with co- or counter- helicities. The final products vary depending on the initial set-ups. Within all four cases, only the system with parallel

70
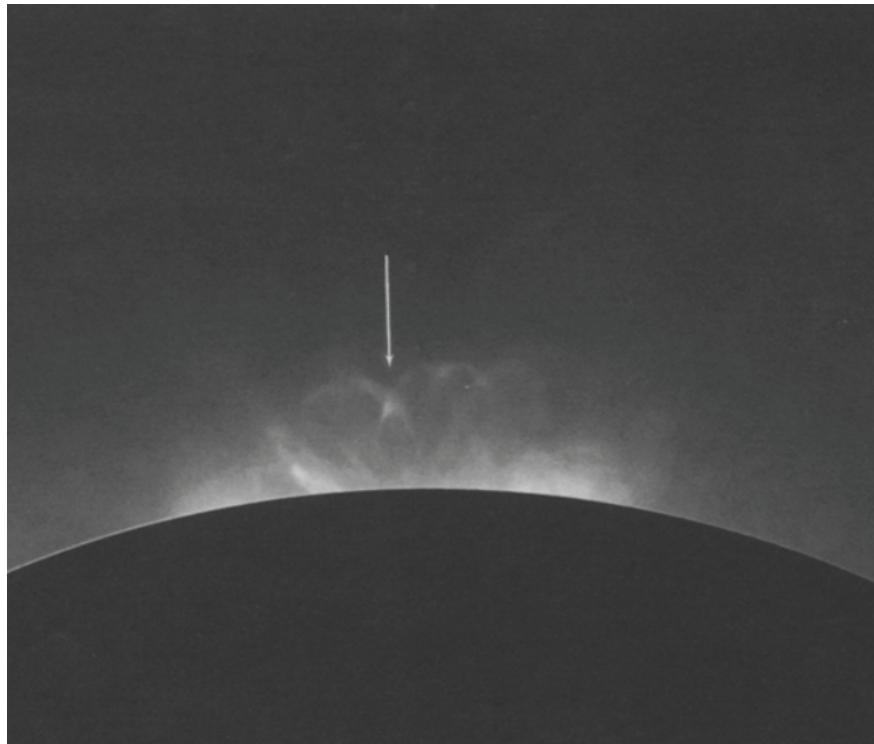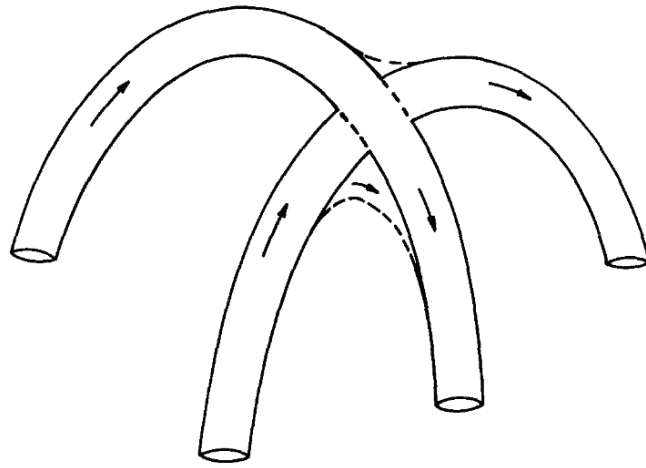
Figure 3.2: Sketch of the interacting post-flare coronal loops and the observation of an event on April 28, 1990 recorded in the emission of the green coronal line. Figure adapted from (Smartt et al., 1993)

currents and close-to-zero net helicity, successfully generated reconnection. A later study by Linton et al. (2001) also tested the influence of helicity. In addition to parallel and antiparallel configurations, they tested different angles between the flux tubes in 45 deg intervals. The interactions between flux tubes with different settings can be categorized into four types: bounce, merge, slingshot and tunnel. The total energy that was converted during the interaction was also different. Within the four, the slingshot type generates the most efficient reconnection. To achieve the slingshot type of interaction, the angle between two flux tubes can vary from 90 ° to 270 ° and the helicities of the tubes are opposite. Magnetic reconnection occurs at the interface between the two entangled flux tubes. While converting the energy from magnetic field to plasma, magnetic reconnection also modifies the connectivity of the field lines of the two flux tubes.

In addition, in the solar corona, flux tube interactions are also proposed to happen in the solar wind. While the solar atmosphere expands outward, helical magnetic field structures are also carried out. In addition to large scale structures like Interplanetary Coronal Mass Ejections, there are papers that have proposed that the solar wind, especially in the inner heliosphere, is filled with entangled magnetic flux tubes which originate at the solar surface (Borovsky, 2008). An illustration of this texture is shown in Figure 3.3. Instead of being a relatively uniform flow that follows the picture of Parker's spiral, the interaction between the woven flux tubes will modify the flow properties of the solar wind, as well as creating turbulence in the solar wind. Thus it can also alter the energetic-particle propagation in the inner heliosphere, and the driving of the Earth's magnetosphere (Borovsky, 2008; Bruno et al., 2001).

It is reasonable we expect similar processes will happen on the Earth as well. The flux transport on the magnetopause and in the magnetosphere may not always be as straightforward as pictured in the Dungey Cycle.

3.2 Magnetic Entanglement and the Birth of Flux Ropes in Pairs
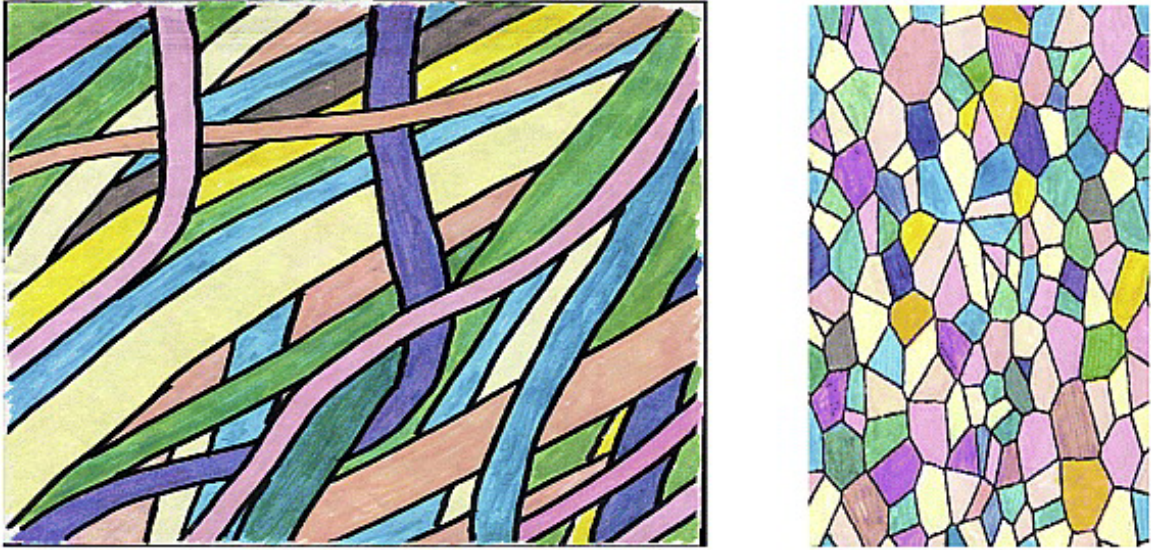
Figure 3.3: A sketch of the flux tube texture of the solar-wind. left panel: A depiction showing the sides of the tubes. right panel: An end view depicts the cross sections of the network of tubes. The scale sizes of the flux tubes correspond to the scale sizes of granules on the solar surface. Image adapted from Bruno et al. (2001)

3.2.1 Flux Rope Properties

As we have introduced in section 3.1, in the idealized model, FTEs are self-balancing magnetic flux ropes. This model does not require strict force-free structure, but the force balance between the magnetic and plasma pressure forces. The bending and winding magnetic field lines insert curvature force toward inside, and the pressure gradient force presses outward. Panel (a) of Figure 3.4 shows an example of the structure of a magnetic flux rope.The purple lines surrounding the orange rope surfaces represent the magnetic field lines; green arrows indicate the pressure force. A rope coordinate system can be established to better understand the measurements of flux rope crossings. The three orthogonal axes are defined as follows: R points to the rope axial direction along which the pressure gradient minimum varies direction; Q is defined by the transverse crossing, and the direction is obtained by the four-spacecraft timing technique; P completes the right-hand coordinate system.
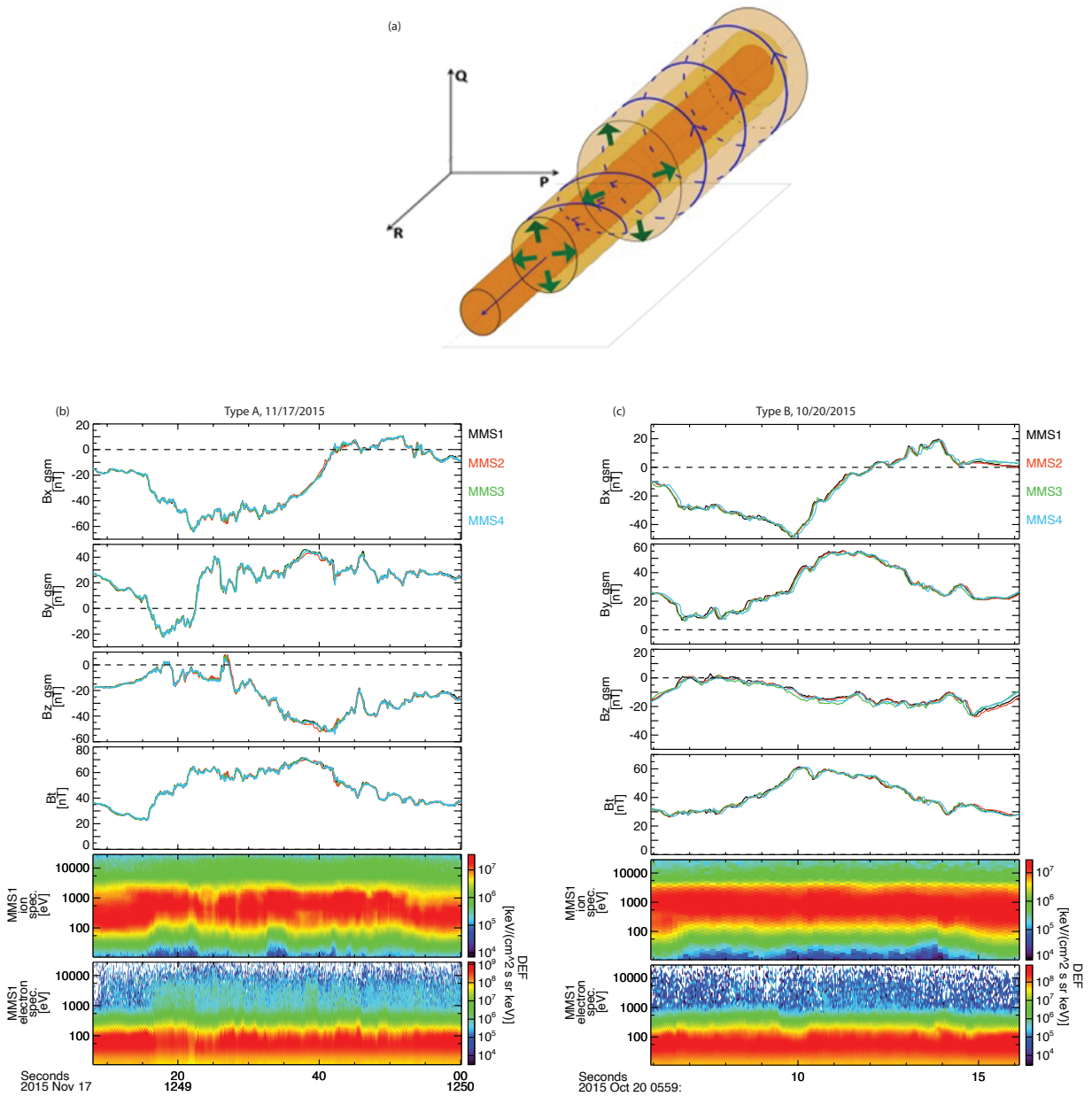
Figure 3.4: (a) Sketch of the internal structure of a magnetic flux rope. (b, c) time series of magnetic field and plasma and particle data during two intervals (on Nov 17, 2015 and Oct 20, 2015) as examples of Type A and Type B flux ropes. During the first interval, energetic (1–10 keV) electrons are present (Type A), but in the second interval, they are not (Type B).

3.2.2 Two Types of FRs: Statistical Study

While the observed FTEs at the Earth's magnetopause all share similarities in magnetic field profile, their plasma contents differ and can be categorized into two types. One type populated with electron flux of magnetospheric energies (Type A) and the other without such electron flux (Type B). Panel (b) and Panel (c) of Figure 3.4 show examples of these two different types of flux ropes with time series of the magnetic field components and field strength, as well as the ion and electron differential energy flux. Energetic electrons are clearly seen between 1 and 10 keV in panel (b), but in panel (c), the electron flux within this energy range is much weaker. This difference indicates that the first flux rope is more likely connected to the magnetosphere on both ends, thus it can trap magnetospheric electrons inside easily. In contrast, during the second interval, the flux rope may not connect with the terrestrial magnetosphere but instead, connect only to solar wind field lines so magnetospheric electrons can escape quickly.

An important question is: Whether there is any additional difference besides the presence of energetic electrons? To answer this question, we examined 98 flux ropes during MMS mission phase 1a. Within the 98 events, 47 were identified as Type A (energetic electrons are present) while the remaining 51 are identified as Type B (energetic electrons are not present). Figure 3.5 displays the spatial distribution of these events in the Geocentric Solar Magnetospheric (GSM) coordinate system Y-X plane (panel (a)), Z-X plane (panel (b)) and Z-Y plane (panel (c)). In all panels, the symbol + represents Type A, and $\triangle$ represents Type B.

We do not find distinguishable differences in the spatial distributions of the two types. If there is a process resulting that Type A flux ropes are "closed" field lines so they can trap magnetospheric electrons and Type B flux ropes are "open" field lines so they let energetic particles escape easily, this similarity in the spatial distribution suggest the occurrence rates of the two types are independent of location.

In addition to the location, the magnetic field strength (3.6 panel (a) and (b)) of the two types also appears to be the same. The peak-to-peak magnetic field distribution has
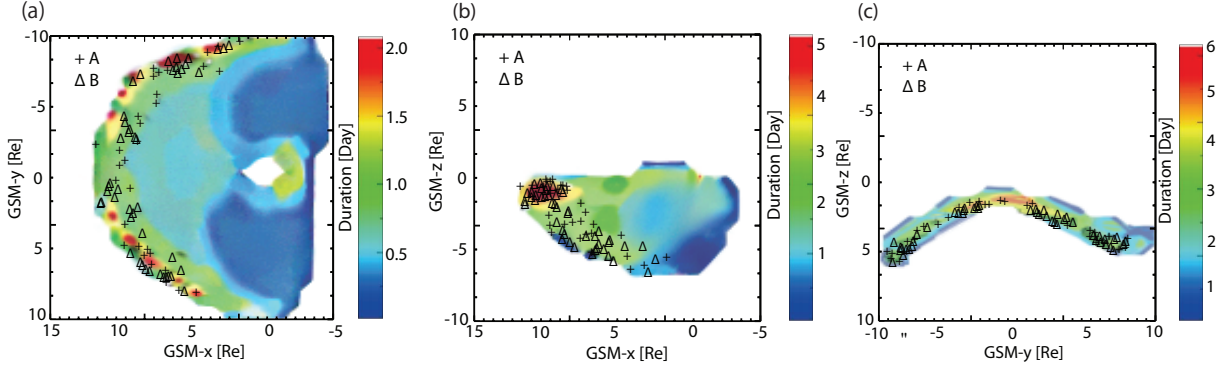
Figure 3.5: The location of the crossings of flux tubes by the four MMS spacecraft. The symbols △ and X indicate flux tubes with and without significant fluxes of energetic electrons. These plots show the same spatial distribution for each type of rope. Panel (a) is the GSM X-Y plane, that is, the view from above the Earth. Panel (b) is the Z-X plane, the view from the dusk side. Panel (c) is the Y-Z plane, that is, the view from the Sun. Adapted from Zhao (2019)

the largest density at 40 – 60 nT for both types which is reasonable in the vicinity of magnetopause. The shape of the distribution is also similar. When we normalize the peak-to-peak magnetic field strength by using the core field strength of the rope, the distribution becomes identical. When the total flux content (Figure 3.6 panel (c)) of the two types of FRs is calculated, their distribution is still almost the same. This suggests that the process that is responsible for the generation of these ropes does not lead to extra compression or more magnetic flux for one type.

Another factor that usually has impact on dayside magnetopause dynamics is the Interplanetary Magnetic Field (IMF) orientation. Figure 3.7 panel (a) shows the distribution of the IMF B_z GSM magnetic field strength in 2 nT bins during the timespan of MMS phase 1a. The occurrence rate peaks around 0 nT and becomes almost zero at ± 10 nT. The distribution is symmetric. However, when we use this distribution to normalize the occurrence rate of FRs as a function of IMF B_Z values, the distributions of both types are no longer symmetric with an apparent bias toward the southward negative B_z values. For
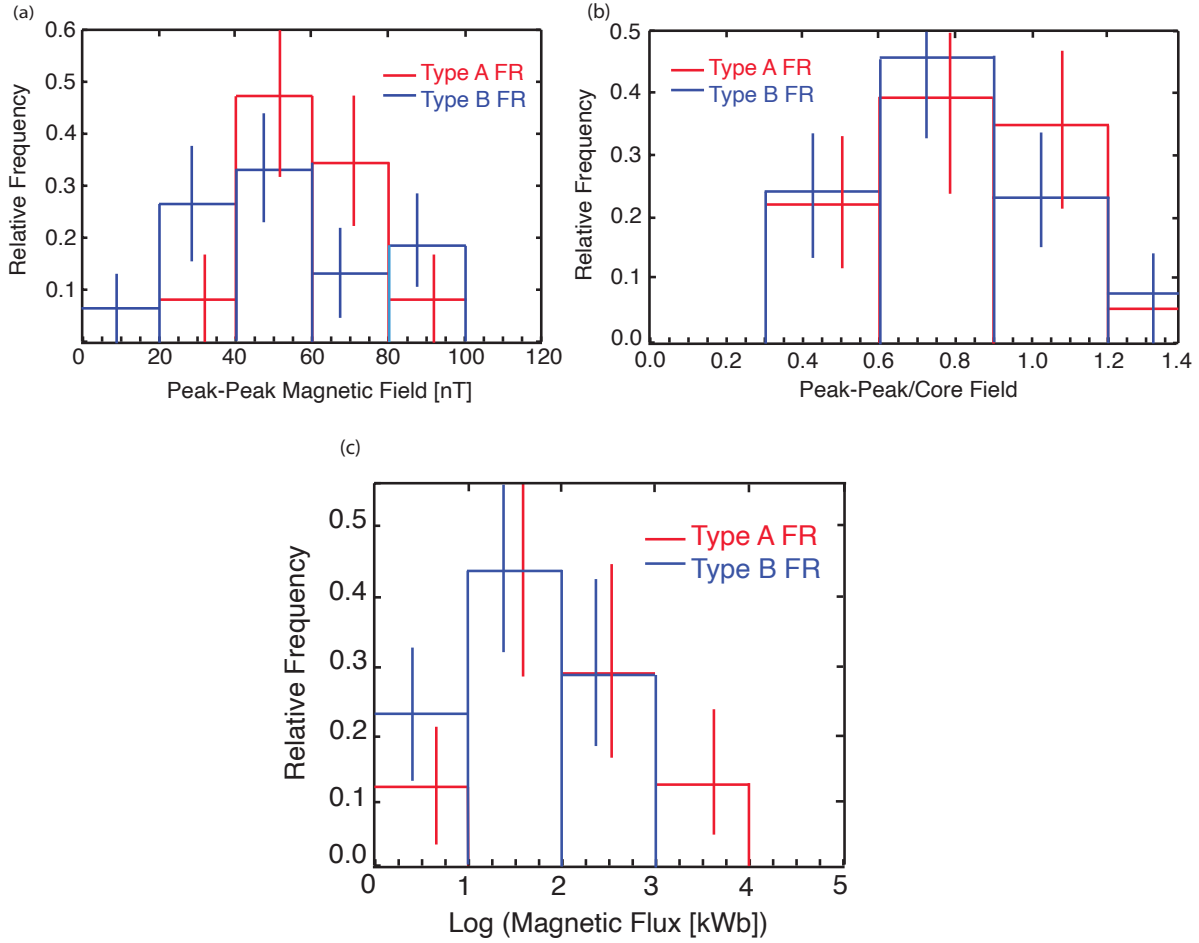
Figure 3.6: The statistics of two types of flux ropes: (a) Histogram of the occurrence rate as a function of the peak-to-peak field strength. (b) Histogram of the occurrence rate versus the ratio of the peak-to-peak field divided by the core field strength. (c) Histogram of the flux content. Adapted from Zhao (2019).

northward positive B_z, there are a few FRs, but not many. The occurrence rate increases for increasingly southward IMF B_Z until the (-6 to -4 nT) bin, when the rate suddenly drops. Considering this dramatically decreasing occurrence rate, and the gradually decreasing IMF distribution under this extreme circumstance, this behavior is possibly not a statistical fluke but rather signals that rope production does not occur for large magnetic B_z of about -10 nT and stronger. Still, this trend is shared by both types of flux ropes no matter they contain magnetospheric electron fluxes or not. Thus, we suggest there is not statistically significant

dependence of the rate of flux rope production or difference between A and B rates
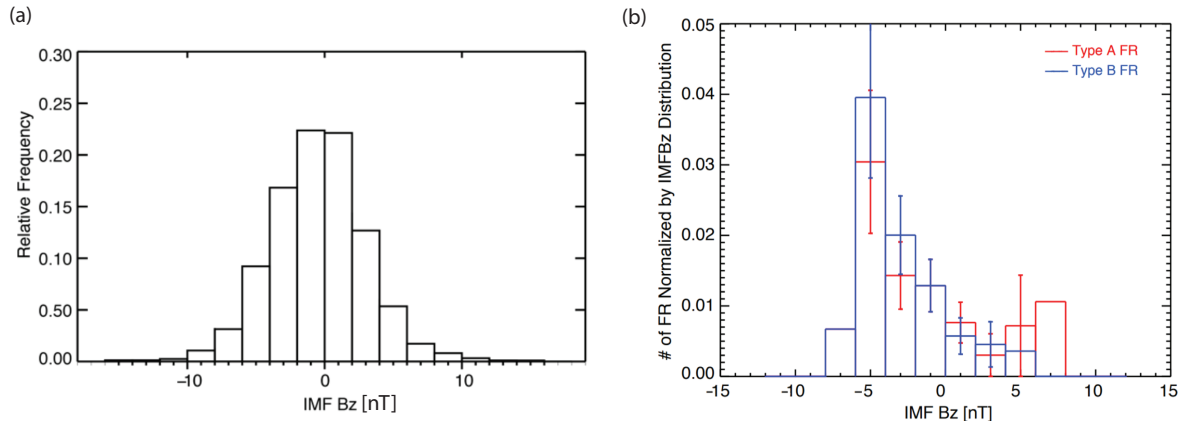
Figure 3.7: (a) The occurrence rate of the north-south component of the interplanetary magnetic field measured by the Wind spacecraft in GSM coordinates in 2 nT steps, from -12 to 12 nT. (b) The occurrence rate of the two classes of event versus the north-south component of the interplanetary field normalized by the occurrence rate of these north-south fields. Adapted from Zhao (2019).

In all of the parameters we examined, the number of flux ropes devoid of magnetospheric energetic electrons matches the number of flux ropes with energetic electrons in all the comparisons. The most likely way of causing this is that the flux rope production process produces an empty flux tube at the same time when it produces a filled flux tube. This process occurs in common solar wind conditions with a preference in slightly southward IMF and occurs frequently across the magnetopause. In the next part, we discuss a possible mechanism that meets the above requirements that can take place, resulting in the production of a pair of flux ropes of which one closes in the magnetosphere proper while the other one has no ends in the magnetosphere.

3.2.3 How Pairs of FRs Can Be Produced

Previous studies, e.g. (Kacem et al., 2018; Øieroset et al., 2019), have demonstrated with MMS observations the interaction between two converging magnetic flux tubes that come

from two different reconnection lines during a period with a moderately southward, or even B_y-dominant IMF. This configuration is sketched in the left-hand panels of Figure 3.8 (a–c). Reconnection taking place in the south (Location 1) and the north (Location 2) will each produce a pair of reconnected flux tube that, on their south/north end, were connected to the south/north polar regions (one to each), and another pair between the two locations that will converge and collide with each other. Then these two flux tubes become entangled as shown in Figure 3.8b. At the interface between two entangled flux tube, magnetic field will build up and reconnection could happen with their regions of anti-parallel fields (Pyakurel et al., 2019).

The interface between these two converging tubes undergoes reconnection and annihilates any anti-parallel magnetic field lines at the entanglement, while the parallel segments remain to form two "new" ropes. Before reconnection, field lines are connected to the magnetosphere on one end and connected to the sheath on the other end. After reconnection, half of the field lines (north pointing as shown in Figure 3.8 (c)) are connected to the two high-latitude regions in Earth's ionosphere, and the other half (horizontal as shown in Figure 3.8 (c)) are completely disconnected from Earth's magnetic field. Figure 3.8 (d–k) reviews an example of the middle stage-an ongoing entanglement between two flux tubes that are not magnetically connected (first reported by Kacem et al. (2018), and Øieroset et al. (2019), and the reconnection-related characteristics have been analyzed in detail). On 7 November 2015, MMS satellite located at [8.6, 6.2, -0.9] R E in geocentric solar ecliptic coordinates. From 14:16:20 to 14:17:00, MMS observed a sharp rotation in the magnetic y component centered on a significantly enhanced field strength region (Figure 3.8 (d–g)). This sharp rotation corresponds to a thin current sheet crossing, and it differs from the bipolar signature when crossing a normal FR which varies smoothly and expands into the whole field enhanced region. Figures 3.8 (j) and (k) demonstrate the electron pitch angle distribution of the low-energy (10–200 eV) and mid-energy (200–2 keV) range, and the sudden change of plasma population at the current sheet indicates the two sides are not magnetically connected, and thus does not fully agree with the magnetic island picture. The electron and ion number
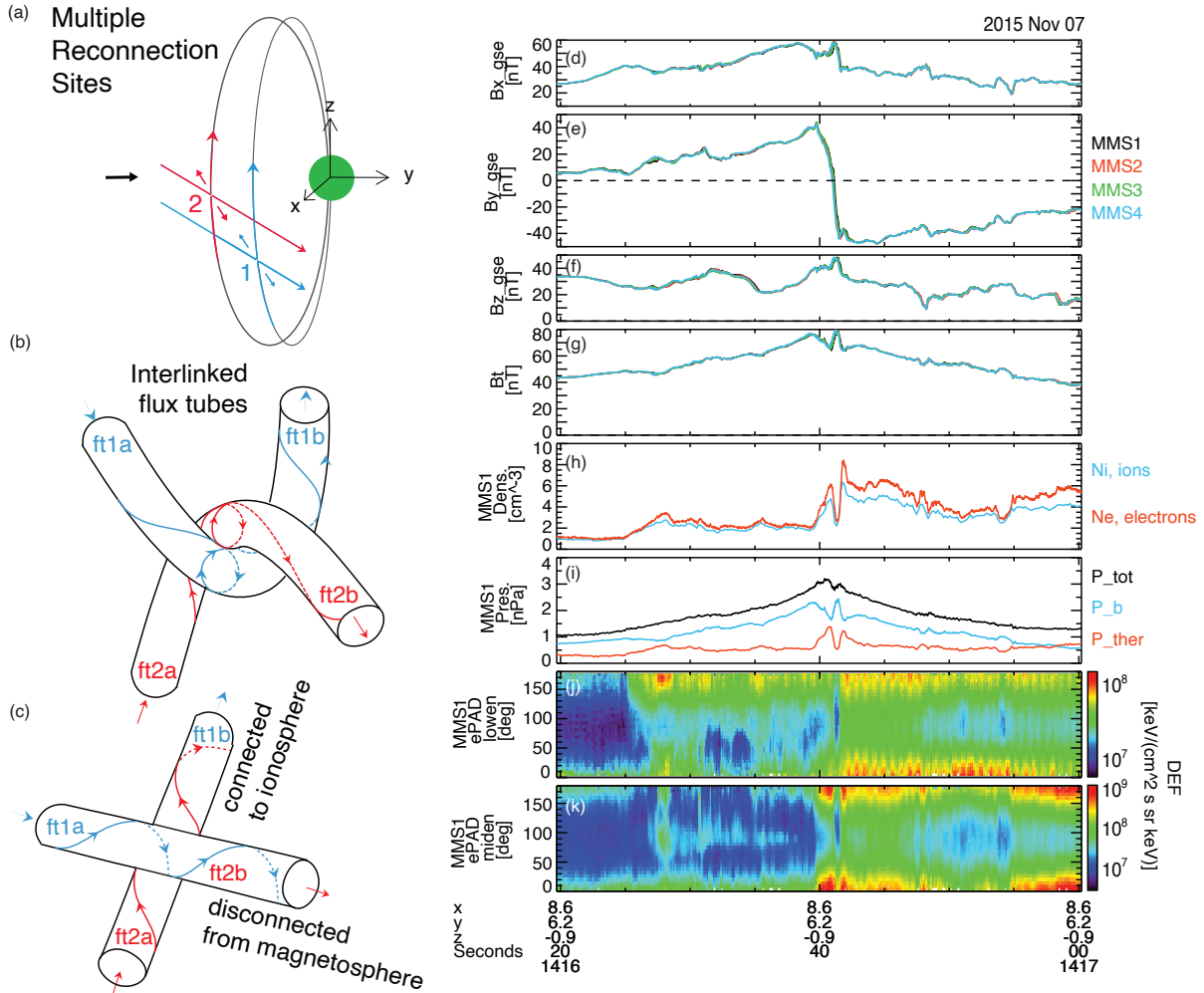
Figure 3.8: (a)-(c) Sketch showing how entangled flux ropes can be produced when the interplanetary magnetic field is southward and oblique to the equator; (d)–(g) show the magnetic field in geocentric solar ecliptic coordinates and the magnetic field magnitude. Panel (h) shows the ion and electron densities. Panel (i) shows the thermal and magnetic pressure plus their sum. Panels (j) and (k) show the electron flux versus pitch angle at low and medium energies.

density fluctuate and have a minimum colocated with the central current sheet (Figure 3.8 (h)). Despite the variations of magnetic pressure (the blue line in Figure 3.8 (i)) and plasma pressure (the red line in Figure 3.8 (i)), the sum of these two (the black line in Figure 3.8 (i)) grows steadily from the edge to the center. The unbalanced pressure indicated the

equilibrium has not been reached yet and the flux on the two sides will keep pushing in to the reconnecting central current sheet. Thus eventually, all the field lines of the initial tubes reconnect and form a new pair of flux tubes, but now with twisted fields resulting from the reconnection, and thus identified as FRs. One rope of the pair contains magnetospheric plasmas and is linked to the high-latitude ionosphere. These are illustrated in Figure 3.8 (c). A totally unconnected rope would be free of any energetic particles. A rope connected to the north and south magnetic hemispheres would trap energetic particles, and it would exhibit low- and mid-energy electrons at 0° and 180°. This scenario is in complete accord with the observations. We note that this is the simplest tangled configuration and therefore the more common, and expected, configuration.

In short, the formation of FTEs, as described here, does involve both the solar wind connected flux tubes and terrestrial magnetic flux tubes, but not, as originally envisioned by Russell & Elphic (1979), by convecting flux into the polar cap. Rather, the initial reconnection step that led to the production of the flux tubes sent the magnetic flux into the two polar caps, without producing FRs. This initial poleward transfer of magnetic flux increased the sizes of the two polar caps without entanglement. Instead, the FRs result from interlinked flux tubes generated at two independent reconnection sites in the subsolar region: one in each hemisphere, in moderately southward IMF conditions. While initially this leads to a complex magnetic configuration with a tangled magnetic field, magnetic reconnection between the two twisted flux tubes simplifies the magnetic structure and, in the end, produces a configuration containing two ropes, one connected to the magnetosphere and one disconnected from it in the nearby solar wind. Rather than making a complicated magnetic field structure even more complex, reconnection returns the system to a simpler, low-energy state. Our observations in Figure 3.7 panel (h) also suggest that when the IMF is very southward, the tangled fields do not arise, and this process does not occur. When the IMF is horizontal or northward, reconnection appears to be weak, and FRs are also not formed. The FRs appear principally over an intermediate range of southward-directed interplanetary fields under conditions of moderate and high Mach number solar wind flow.

81

3.2.4 Conclusion

For the most common, moderately southward interplanetary fields, the reconnection of magnetic fields in the magnetosheath with those in the magnetosphere produces both reconnected flux with a simple path to the poles and magnetic flux that becomes entangled. The stresses produced by entanglement produce magnetic forces that attempt to simplify the magnetic field configuration. The flux tubes that are connected to the magnetosphere recombine to form a closed flux tube twisted by the entanglement and reconnection and, at the same time, produce a second twisted flux tube with an equal amount of flux that is connected to the solar wind. The entanglement created by the finite area of the reconnecting magnetopause surface has resulted in the production of self-balancing FRs. The flux transfer to the polar regions/tail has been handled by classical transport processes poleward of the entanglement region.

This example of entanglement at the Earth's magnetopause might have lessons for magnetic reconnection in other venues, such as on the Sun. The Sun produces very large FRs that are responsible for coronal mass ejections. There seems to be no consensus on the instability that is responsible for these energetic events, but for the largest events, the rate of occurrence decreases with increasing strength, and their strength, as judged by speed, is grouped in narrow bins (Freed & Russell, 2014). It is possible that magnetic entanglement on the Sun also plays a role in creating different types of magnetic ropes, possibly with both open ropes ejected into the solar wind and closed ropes that stay connected to the Sun. Entanglement may be an important step in the evolution of magnetic fields in the cosmos, leading to explosive events.

3.3 Temporal Evolution of Magnetic Entanglement

3.3.1 Introduction

We have introduced the concept of magnetic entanglement in the previous section. The start of magnetic entanglement is that reconnection occurs at multiple locations on the magnetopause simultaneously. Thus, the motion of the flux tubes leaving reconnection sites may become intricate, especially when the equatorial component of the interplanetary magnetic field (IMF) is significant (Fargette et al., 2020a; Kan, 1988; Nishida, 1989; Otto, 1991; Zhao, 2019). Under these circumstances, two flux tubes generated by reconnection, each with one end connected to the northern/southern hemisphere of the Earth and the other end connected to the magnetosheath, that flow away from their original reconnection sites may collide and become entangled. The magnetic field becomes highly compressed around the interface of these two entangled flux tubes. Secondary reconnection can occur within the flux pile-up region to alter the field line connectivity, which can further simplify the complexity of magnetic entanglement. Previous three-dimensional MHD simulations (Fedder et al., 2002; Lee et al., 1993), global hybrid simulations Tan et al. (2011) and observations (Bogdanova et al., 2008; Lv et al., 2016; Pu et al., 2013) have examined how reconnection enables the field topology changes.

Recently, with the improvement in spatial and temporal resolution of instruments, direct observations of flux tube entanglement, i.e. interlinked flux tube, in addition to the studies we mentioned in the previous sections were reported (Fargette et al., 2020a; Hwang et al., 2020; Kacem et al., 2018; Kieokaew et al., 2020; Øieroset et al., 2019). These studies pointed out the differences between a single stand-alone flux rope and the magnetic entanglement between two flux tubes. These differences include: the large pressure enhancement mainly due to the magnetic field build-up which violates the force balance flux rope model (Russell et al., 2017); a sharp rotation of magnetic field at the field strength peak region instead of a smooth bipolar variation in the transverse direction; and disparate plasma on two sides of this thin current indicating the lack of magnetic connectivity.

In these studies, reconnection characteristics have been carefully identified at the entanglement interface. As it proceeds, reconnection is expected to resolve the entanglement

and generate a new pair of flux ropes. In contrast to the initial pair which had one end connected to Earth and the other end to the sheath, now one rope has both ends connected in the magnetosheath while the other one has its both ends connected in the magnetosphere (Russell & Qi, 2020).

In this section, we further evaluate the effect of reconnection between entangled flux tubes. By examining 17 entanglement events, we identify the characteristics of entanglement at their different evolutionary stages using the field line geometry, the pressure profile, and electron distributions. We use three representative events to outline the three evolutionary stages of flux rope entanglement. Then we revisit a classic entanglement event with additional analysis at the interface and tabulate all the 17 events. Section 4 includes further discussion and a summary of our findings.

3.3.2   Dataset

All flux tube entanglement events studied here are found from the Magnetospheric Multiscale (MMS) mission (Burch et al., 2015) data during its first two dayside phases (Winter 2015-2016 and Winter 2016-2017) (Fuselier et al., 2016). In these time periods at the magnetopause, the MMS maintains a tetrahedron formation at apogee with spacecraft separation usually being < 100 km, which allows us to analyze spatial gradients at the electron-kinetic scale. The magnetic field is measured by the fluxgate magnetometer (FGM) (Russell et al., 2014) at its highest sampling rate of 128 Hz. Fast plasma investigation (FPI) instruments (Pollock et al., 2016) provide the electron/ion distribution functions and moments every 30/150 ms at burst mode, covering the energy range from 10 eV to 30 keV. Solar wind conditions are examined for each event using measurements from the OMNI database (King & Papitashvili, 2005).

3.3.3   Selecting Entanglement Cases

We examined events from published literature (Fargette et al., 2020a; Hwang et al., 2020; Kacem et al., 2018; Kieokaew et al., 2020; Øieroset et al., 2019) as well as our own FTE-like

event list and looked for entanglement characteristics by eye. No quantitative criteria were established previously as and these characteristics were discussed mainly qualitatively. When we were selecting events, we kept only the typical events that are comparable to previously reported cases. Here as recorded in Table 3.1, we summarize their common features in a measurable way:

- A significant increase in both magnetic field strength and total pressure (the sum of plasma thermal pressure nkT and magnetic pressure $B^2/(2\mu_0)$ ($\Delta P_{tot} \gtrsim 50\%$)

- A sharp rotation of the magnetic field (i.e., a thin current sheet) around the maximum pressure location (the current duration $< 25\%$)

- A sudden change in the electron pitch-angle distribution across the central current sheet

Here, ΔP_{tot} is obtained by the peak value of total pressure P_{tot} during the event divided by the ambient P_{tot} outside the enhancement. The "current ratio" is calculated by the duration of the reversal component peak-to-peak interval (also corresponds to the prominent current density increased interval) divided by the duration of B enhancement interval

Table 3.1 lists all the events with their times and locations in the Geocentric Solar Magnetospheric (GSM) coordinate system. Our purpose here is not to conduct a complete survey and we have not tried to select all the entanglement events from the MMS measurements. Thus, the statistical distributions discussed in this paragraph only represent these 17 events. With this in mind, we still find that the event locations are slightly biased towards the dusk side, with 10 of 17 events located in positive Y GSM (Figure 3.9 panel (b)). The events also tend to appear below the equator in a limited Z GSM range (< 6 RE), which may be caused by the longer dwell time of the MMS in the southern hemisphere and the limited latitude coverage of the orbits. In general, the flux tube entanglement events are ubiquitous and happen frequently at the magnetopause. Figure 3.9 (a) shows the solar wind clock angle distribution during these events. Peak distribution appears close to the horizontal direction.

No.	Date	Start Time	End Time	Location (GSM) [RE]	Ptot [%]	Current Duration [%]	Notes
1	2016-12-10	04:52:59	04:54:04	[9.55, 0.14, -0.46]	59	1.9	1
2	2015-10-31	07:17:44	07:19:06	[10.73, 3.48, -2.31]	73	4.6	1
3	2015-11-07	14:16:22	14:16:55	[8.62, 5.42, -3.22]	160	6.5	1
4*	2017-05-05	20:06:42	20:06:57	[-13.97, -17.91, -4.76]	139	16.8	2
5	2015-11-05	14:47:06	14:47:34	[8.17, 5.74, -3.27]	83	2.1	3
6	2015-11-21	01:55:59	01:57:38	[9.73, -1.42, -0.35]	112	3.7	3
7	2016-02-10	02:47:23	02:48:14	[6.45, -7.68, -4.61]	28	4.1	3
8	2016-12-28	04:59:12	04:59:46	[10.90, -1.60, 0.10]	94	2.3	3
9	2015-12-08	10:27:41	10:28:07	[10.81, 0.82, -1.27]	46	3.5	3
10	2016-02-26	01:48:54	01:49:11	[4.28, -7.91, -5.48]	99	6.1	3
11	2016-11-12	17:50:27	17:51:25	[6.60, 9.17, -1.09]	121	6.8	3
12	2015-11-06	13:23:31	13:24:24	[9.27, 5.26, -3.38]	212	5.1	4
13	2015-12-03	10:24:08	10:25:13	[11.04, 1.31, -1.48]	60	6.4	4
14	2016-01-18	01:22:46	01:23:11	[8.57, -7.43, -3.92]	49	1.3	4
15	2015-10-11	12:48:52	12:49:31	[8.01, 7.35, -5.06]	69	7.8	4
16	2015-11-17	14:20:56	14:21:05	[8.48, 4.48, -2.52]	97	5.0	4
17	2015-11-17	14:21:45	14:21:59	[8.48, 4.48, -2.52]	83	13.1	4

Table 3.1: Time and location of the identified flux tube entanglement events. As labeled in the notes column, some events have been reported in recent publications: 1. (Øieroset et al., 2019); 2. (Hwang et al., 2020); 3. (Fargette et al., 2020a); 4. This paper. *Event #4 has been studied as entanglement between flux tubes generated within a Kelvin-Helmholtz vortex, but was not detected at the dayside magnetopause.

This agrees with earlier findings that entanglement favors a By-dominated IMF condition (Fargette et al., 2020a; Hesse et al., 1990).
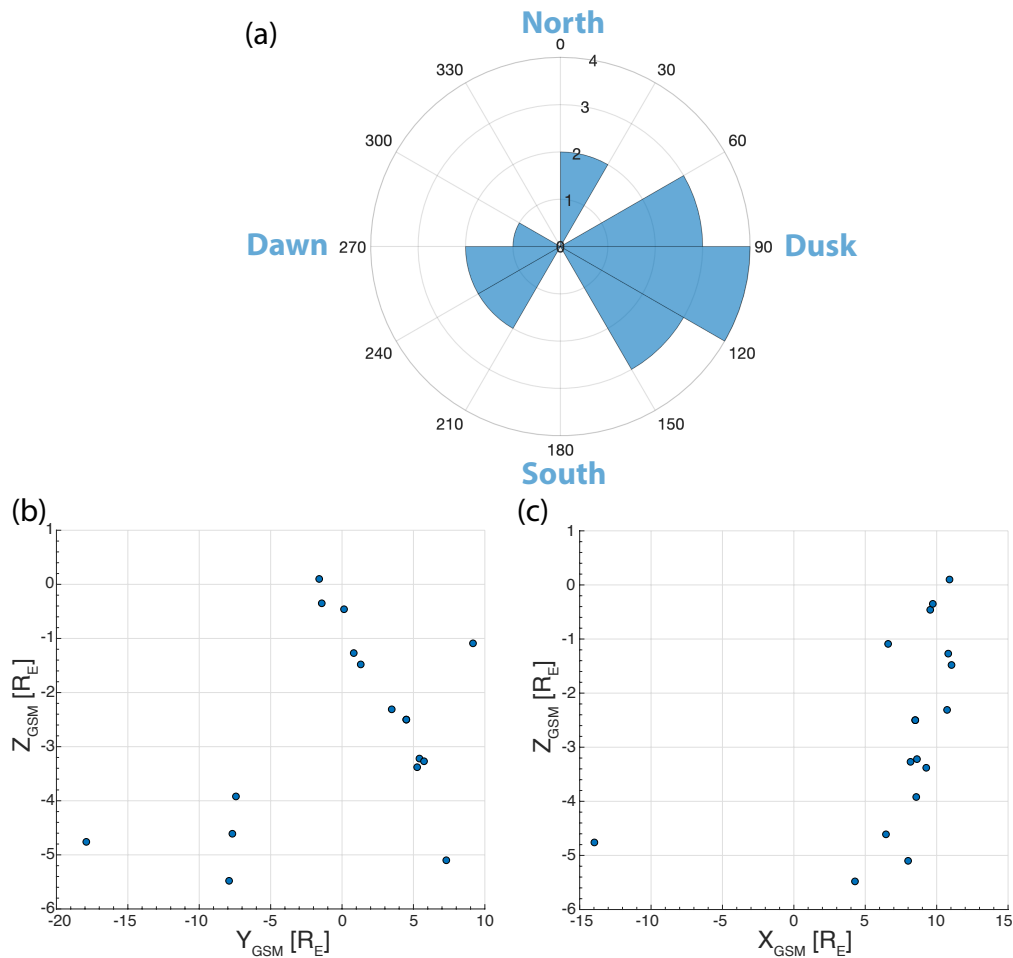

Figure 3.9: IMF conditions and locations of 17 events. (a) Solar wind clock angle measured by the MMS during the 17 events. Starting from 0°, each bin is 30° wide. The bar length in units of radius is the number of events in that clock angle bin. (b), (c) The locations of 17 events in the GSM Y-Z and X-Z planes. Event 4 has been studied as entanglement between flux tubes generated within a Kelvin-Helmholtz vortex, but is not detected at the dayside magnetopause

3.3.4 Three Evolutionary Stages of Magnetic Entanglement

As shown in the sketch of Russell & Qi (2020), two flux tubes generated at different primary reconnection sites move towards each other. These tubes have one end connected to the Earth, and the other end connected to the magnetosheath. When the two flux tubes encounter each other, there is no way for them to pass. Instead they become entangled and stretched, with significant compression at the interface. How do they eventually disentangle? We have identified three typical cases to examine this evolution process.

Figure 3.10, 3.11, and 3.12 use three typical events to show the temporal evolution of flux tube entanglement: Event no. 13 (3.10), event no. 3 (3.11), and event no. 1 (3.12) in Table 1. We rotate the data into an LMN coordinate system, where N is the current sheet normal direction determined by four-spacecraft timing (Russell et al., 1983), M' is the averaged current direction (current interval is marked by blue vertical lines in figure 3.10), the L direction is perpendicular to the plane containing both N and M', and finally $N \times L$ gives M. We note that this LMN coordinate is different from the LMN coordinates of a flux rope that we mentioned in the introduction. In this coordinate system, the interface between the two flux tubes is demonstrated by the sharp reversal of the BL component near the maximum field strength location. Each side of this current sheet corresponds to one of the flux tubes that are not magnetically connected. Near this interface where the maximum field build-up and distortion is expected, we compute the magnetic field curvature $\mathbf{C} = \mathbf{b} \cdot \nabla \mathbf{b}$ using a linear gradient estimation(Shen et al., 2003), where $\mathbf{b} = \mathbf{B}/B$ is the unit vector along the magnetic field. The N (normal) component of the curvature vector is plotted and used to visualize whether the field lines on the two sides are bending towards the current sheet and are imposing pressure on each other.

For all three events, we show the four-spacecraft-averaged magnetic field, the current density, the pressure, the ion and electron energy spectrogram in a wider time range to demonstrate the full entanglement (pressure enhanced) region as marked by the black vertical lines. The magnetic field curvature projected in the direction of the current sheet normal is plotted in a narrower time interval around the sheet marked by the blue vertical lines. The

red vertical line marks the maximum current density location within the current sheet.
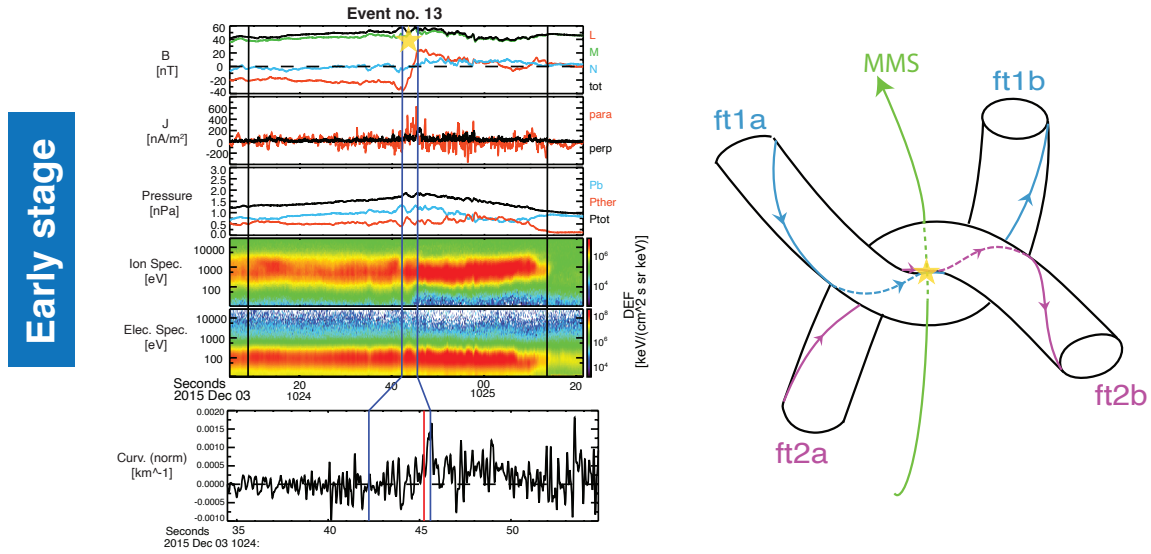

Figure 3.10: Context plot and schematic sketch showing characteristics of the early stage of the entanglement. The LMN directions in GSM are L: [0.50, -0.86, -0.06], M: [0.42, 0.18, 0.89], N: [0.75, 0.47, -0.46]. A possible MMS trajectory is sketched in green. The yellow star in top panels mark the central current sheet crossing.

In Figure 3.10 which corresponds to the early stage (event no. 13), the curvature normal component varies around zero, showing no systematic pattern at the central current sheet. The total pressure enhancement is only about 60% of its ambient value, indicating a not-yet-grown compression as the two flux tubes just start to interact. Throughout the entire pressure enhanced region in event no.13, the MMS does not observe a significant electron population at energies above 1keV. This is consistent with an early stage of entanglement, when neither of the two entangled flux tube are "closed" in the magnetosphere. Thus, it is difficult for them to trap the hot magnetospheric electrons.

As the entanglement proceeds, the field lines bend more toward the current sheet, keep adding magnetic tension force, leading to further increased compression. The most outstanding difference between event no. 3 (Figure 3.11) and the other two is the curvature normal component. The clear negative-to-positive bipolar signature of the curvature normal
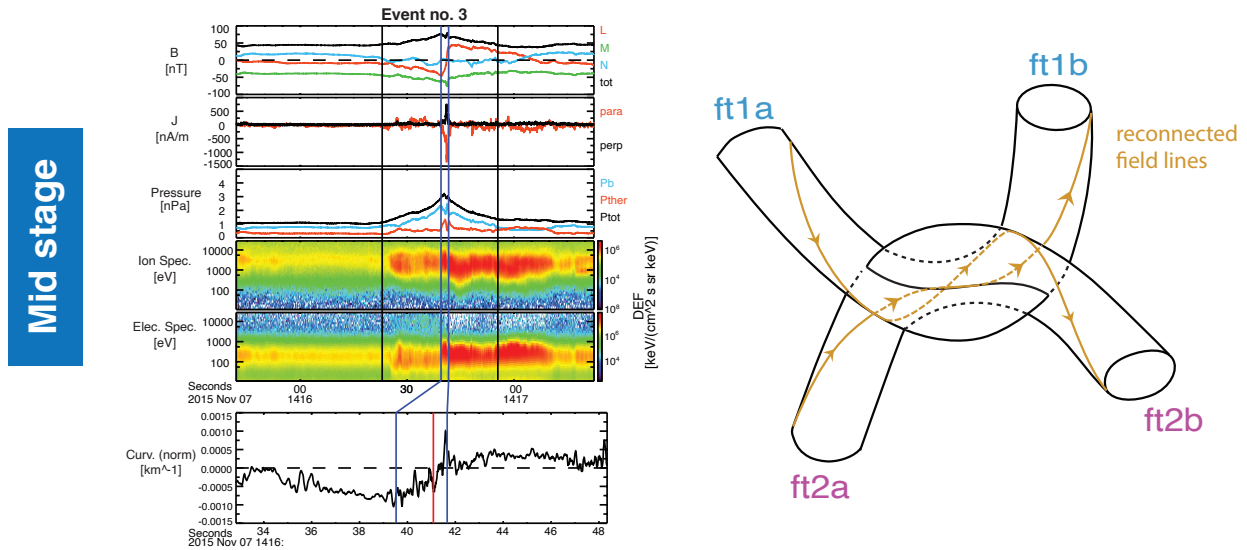
89

Figure 3.11: Context plot and schematic sketch showing characteristics of the mid stage of the entanglement. The LMN directions in GSM are L: [-0.08, -0.92, 0.39], M: [-0.78, -0.19, -0.59], N: [-0.62, 0.36, 0.70].

in event no. 3 indicates that the magnetic field lines are curving towards the central current sheet on both sides. Magnetic flux piles up around the central current sheet, resulting in a total pressure imbalance (pressure panel of Figure 3.11, or enlarged plot in Figure 3.13), and preparing for secondary reconnection to release the energy (Øieroset et al., 2019). The total pressure enhancement is about 190% of the ambient value. These features are consistent with this being the stage when the two flux tubes are actively pulling against each other, and the magnetic field wraps around the interface tightly. Based on the strong pressure build-up and the negative-to-positive bipolar curvature N component, we label event no. 3 as the middle stage of the entanglement process.

Eventually, a new pair of ropes are formed by a topological transition from the initial pair of flux ropes, as shown in Figure 3.12 (event no. 1). In contrast with the initial flux tube pair, now one rope has its both ends connected to the ionosphere ("closed" in the magnetosphere) while the other rope has its two ends connected to the magnetosheath ("interplanetary"). The "closed" flux rope is capable of trapping energetic magnetospheric
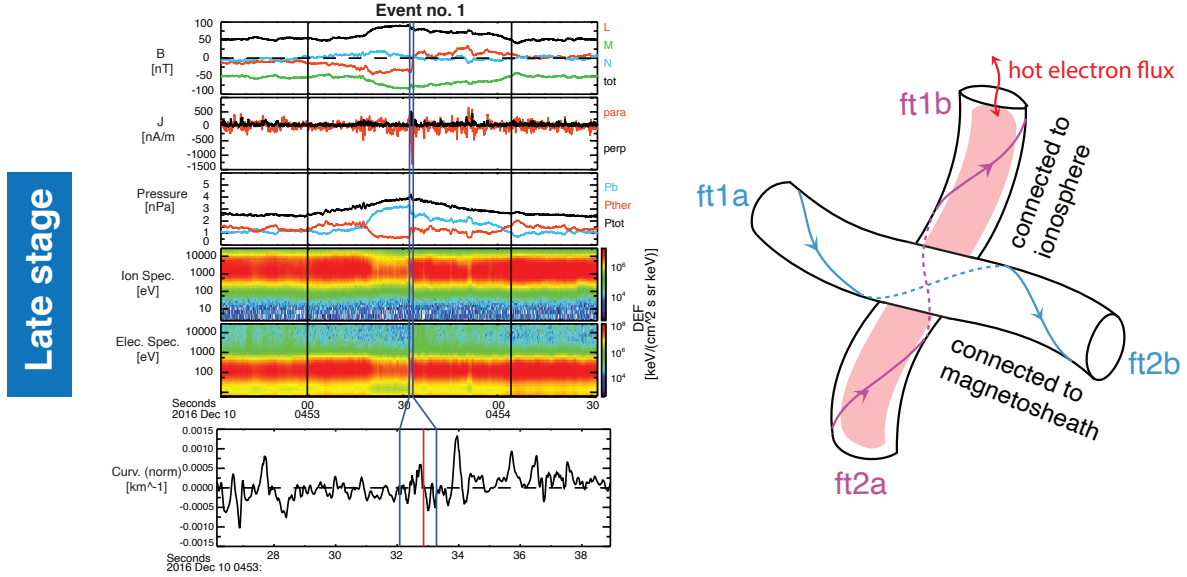
Figure 3.12: Context plot and schematic sketch showing characteristics of the late stage of the entanglement. The LMN directions in GSM are [0.66, -0.58, -0.48], M: [-0.34, 0.34, -0.88], N: [-0.67, -0.74, -0.03].

electrons. The "interplanetary" flux rope will lose its energetic electrons quickly. Comparable to the early-stage event no. 13, the curvature normal component remains insignificant except in the current sheet region in event no. 1. The total pressure enhancement is 70% in event no. 1, similar to that of the entanglement in its early stage. At this late stage, the compression has been canceled when reconnection has almost released the entanglement and the new ropes are about to form. The key difference between event no. 13 and event no. 1 is in the electron distributions. In event no. 1, the right half of the pressure enhanced region shows increased electron flux between 1keV — 10 keV, which is absent in the left half. This is consistent with a later stage of entanglement when reconnection has almost finished, making two new ropes one of which (like the right half in event no. 13) has the majority of its field lines connected to the southern and northern hemisphere of the Earth and is capable of trapping the hot electrons originating from the plasma sheet.

We found 8 events within the 17 events that can be categorized clearly into these three stages. These events are listed in Table 3.2 As sketched to the right of each event in Fig-
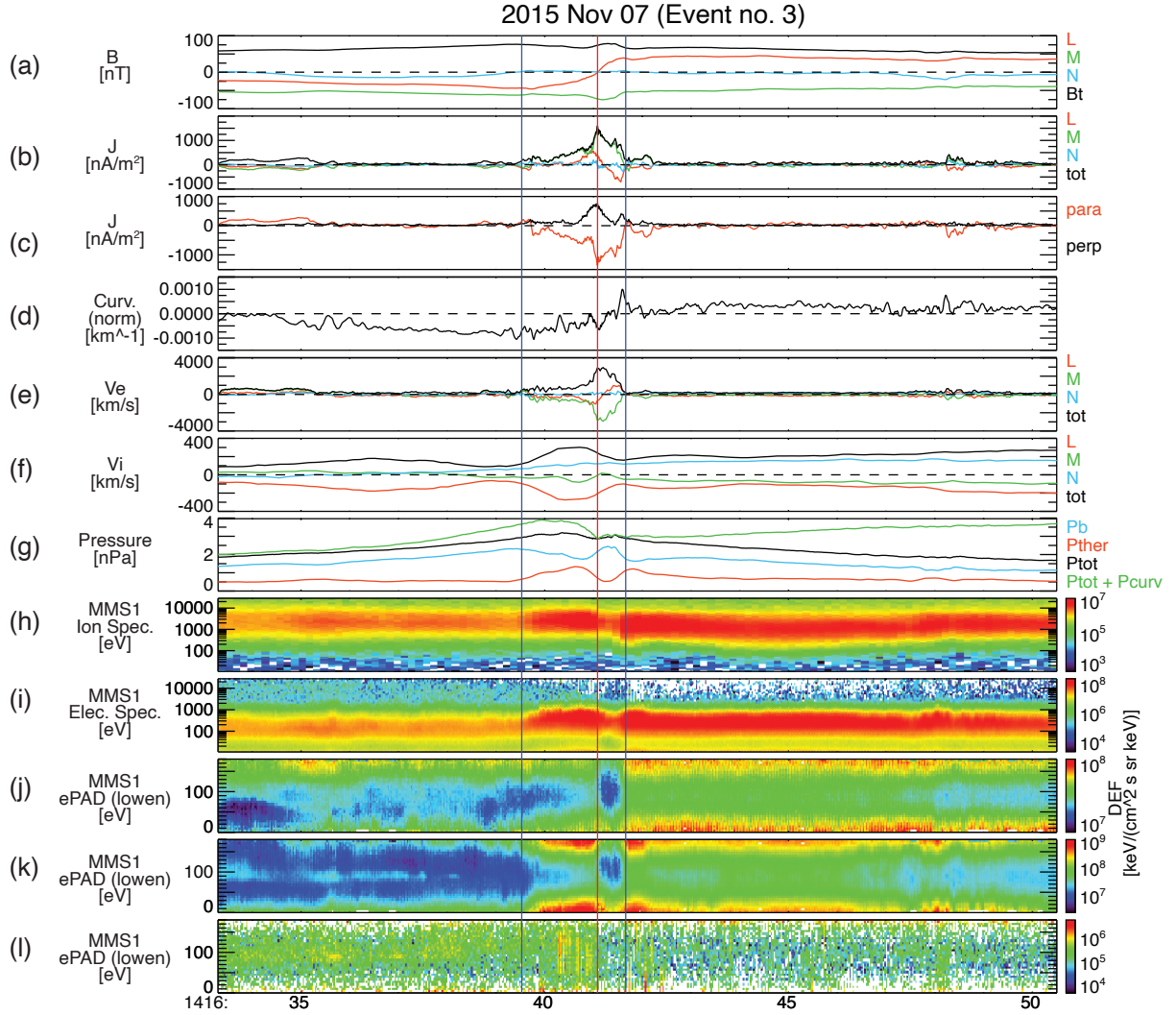
91

Figure 3.13: An example of two entangled flux tubes as observed by the MMS on 2015 November 7. (a) Four-spacecraft-averaged magnetic field in LMN coordinates and the field strength; (b), (c) current density computed by curlometer technique in LMN and field-aligned coordinates; (d) magnetic field curvature projected in the direction of central current sheet normal; (e), (f) four-spacecraft-averaged electron and ion bulk flow velocity; (g) four-spacecraft-averaged pressure; (h), (i) ion and electron energy spectrogram at MMS1; (j)-(l) electron pitch-angle distribution for low (10eV-200 eV), mid (200eV-2 keV), and high (2 keV–30 keV) energy range at MMS1. Blue vertical lines mark the central current sheet between two entangled flux tubes. The red vertical line marks the location of strongest current density within this current sheet.

92

ure 3.10, 3.11, and 3.12, we summarize the temporal evolution characteristics of flux tube entanglement as follows:

- The three most diagnostic parameters are: 1) total pressure; 2) the curvature component along the current sheet normal; and 3) hot electron flux.

- An early-stage entanglement does not have the bipolar variation in curvature and has less significant pressure enhancement ($< 100\%$), indicating the two flux tubes are loosely compressed. There are no clear energetic magnetospheric electron flux increases on either side because the flux tubes have not been sufficiently "closed" in the magnetosphere, thus it is harder for them to trap hot electrons.

- A mid-stage entanglement exhibits a clear bipolar curvature normal component, and a fairly strong total pressure increase ($> 100\%$), indicating the significant compression between two tubes. A hot electron population may or may not be present due to the co-existence of magnetic field lines with different connectivity

- A late-stage entanglement does not have the bipolar variation in curvature and has less significant pressure enhancement ($< 100\%$), as the compression has been mostly resolved by reconnection. Energetic magnetospheric electrons appear either before or after the current sheet crossing, indicating that the field lines on this side are almost "closed" (i.e., have two ends on the Earth), and a new pair of flux ropes is about to be born.

We use the mid stage event, event no.3 (November 7, 2015) as an example for further analysis of the highly compressed interface between two entangled flux tubes. The sharp rotation of the magnetic field is clearly seen as the B_L reversal from 14:16:39.527 to14:16:41.660. B_N is close to zero. B_M remains strong and enhanced at the current density peak time (indicated by the red vertical line). The current density dramatically increased around the maximum magnetic flux pile-up region. The dominant component of the current is anti-parallel to the magnetic field, with a magnitude reaching over 1000 nA/m^2. The normal speed of this

No.	Date	Time	Duration [sec]	V_cs [km/s]	CS Duration [sec]	CS Ratio [%]	CS Width [km]	Stage
9	2015-12-08	10:27:40	26	222.7	3.50	5.20	202.66	Early
13	2015-12-03	10:24:00	53	73.1	6.36	5.04	246.35	Early
6	2015-11-21	01:56:50	99	72	3.65	3.58	259.92	Mid
3	2015-11-07	14:16:42	33	90.1	6.46	6.36	191.91	Mid
11	2015-11-06	13:24:00	58	113.8	5.12	6.44	337.99	Mid
1	2016-12-10	04:53:32	65	54.5	1.85	1.83	65.40	Late
8	2016-12-28	04:59:18	34	130.2	2.32	2.49	102.86	Late
13	2016-01-18	01:23:00	65	67.7	1.29	3.50	56.87	Late

Table 3.2: List of 8 events indicative of entanglement temporal evolution

current sheet is about 90 km/s. With a time span of 2.1 seconds (between the blue vertical lines), the current sheet thickness is ∼190 km. Electron bulk flow velocity increases significantly in the current sheet and deviates from the ion bulk flow velocity, especially in the M direction, suggesting that the current is mainly carried by the electrons. The electron flow accelerates and reverses in the L direction (3.13 (e)). Meanwhile, the ion flow increases in the -L direction (3.13 (f)), consistent with the magnetic field actively reconnecting. 3.13 (h–l) manifests the abrupt change in the energy spectra (3.13 (h), (i)), as well as the electron pitch-angle distribution (3.13 (j–l)). Last, in panel (d), the curvature of magnetic field increases around the current sheet into a clear bipolar signature, indicating that the field lines bend towards the current sheet on both sides. This is consistent with the compression of the magnetic field being balanced by the magnetic tension force. The green line in 3.13 (g) is the estimated total pressure including the curvature force in the normal direction integrated along the path away from the current sheet center/maximum current density location:

$$P_{curv} = \int \frac{B^2}{\mu_0} \, |\mathbf{C}_N| \, dx = \int \frac{B^2}{\mu_0} \left(\mathbf{C} \cdot \mathbf{V_{i,perp}} \right) dt \tag{3.1}$$

where B is the magnetic field strength, μ_0 is the vacuum permeability, $\mathbf{C}_N$ is the curvature normal component, $\mathbf{V_{i,perp}}$ is the ion bulk flow velocity perpendicular to the magnetic field). This modified total pressure (green line in Figure 3.13 (g)) on the right appears stable. However on the left, there still remains an apparent slope, suggesting pressure balance has

not yet been reached during such a dynamic process.

3.3.5 Discussion and Conclusions

We applied the stage criteria outlined in the previous section to all 17 events, and we have classified 2 events as early-stage (nos. 9 and 13), 3 events as mid-stage (nos. 3, 6 and 11), and 3 events as late-stage (nos. 1, 8 and 13). The information of these events is recorded in table 3.2.

The rest events are ambiguous and cannot easily be classified into any of the three stages, due to the mixture of characteristics. These events represent the transition phase between three representative stages. This is to be expected since the entanglement is a continuously developing process, and we do not expect a clear boundary between different stages. For example, in event no. 11 (Figure 3.14), the total pressure enhancement is greater than 100% of the ambient plasma, and to the left of the central current sheet, the curvature normal component becomes negative. However, to the right of the central current sheet, there is no clear positive curvature normal component, thus the lack of bipolar signature with a relatively strong compression indicates that event no. 11 is in a transition stage either between early and middle, or between middle and late stages. Another example is event no. 2 (Figure 3.15). While there exists bipolar signature in the curvature, the pressure enhancement is not as strong as other mid-stage events, thus it is also in a transition stage.

To further examine whether the current sheet between two entangled flux tubes is able to reveal the temporal evolution, we list additional information about these local current sheets for each of the eight events in Table 3.2 of the supplementary material. The duration of the entanglement events (the timespan between the event start time and the end time listed in Table 3.1) has a wide range from ∼30 seconds to ∼100 seconds, suggesting that the spatial scale of entanglement varies. The size of the entangled structure depends on the size of the flux tubes, which is determined by the primary reconnection rate and duration. The velocity of the central current sheet is relatively slow, as to be expected in two tubes tugging in opposite directions. Except in event no. 9, current sheets in the rest of the events move
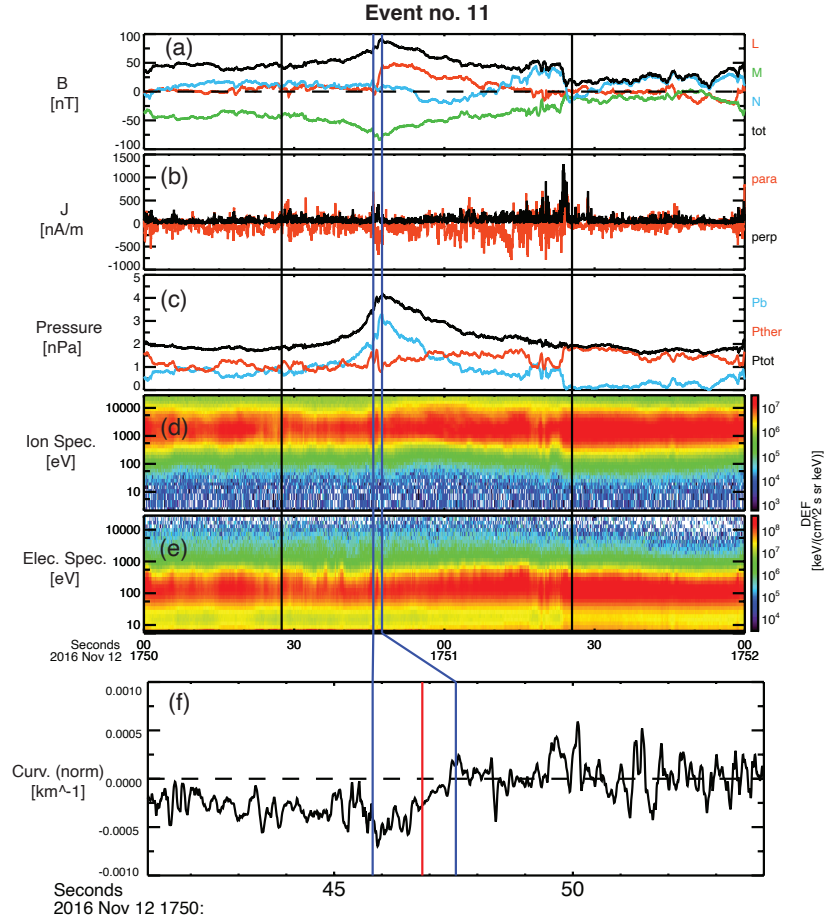
95

Figure 3.14: Summary plot for event no. 11. (a) The four-spacecraft-averaged magnetic field, (b) the current density, (c) the pressure, (d), (e) the ion and electron energy spectrogram in a wider time range to demonstrate the full entanglement (pressure enhanced) region as marked by the black vertical lines. (f)The magnetic field curvature projected in the direction of the current sheet normal is plotted in a narrower time interval around the sheet marked by the blue vertical lines. The red vertical line marks the maximum current density location within the current sheet. The LMN rotation matrix is L: [0.90, 0.38, 0.23], M: [-0.36, 0.92, -0.12] , N: [0.26, -0.03, -0.97]]

at a speed close to or below 100 km/s. The current sheet duration is manually determined as the timespan of the magnetic field rotation region around the pressure peak. The current sheet width is computed by normal speed multiplied by the current sheet duration. There
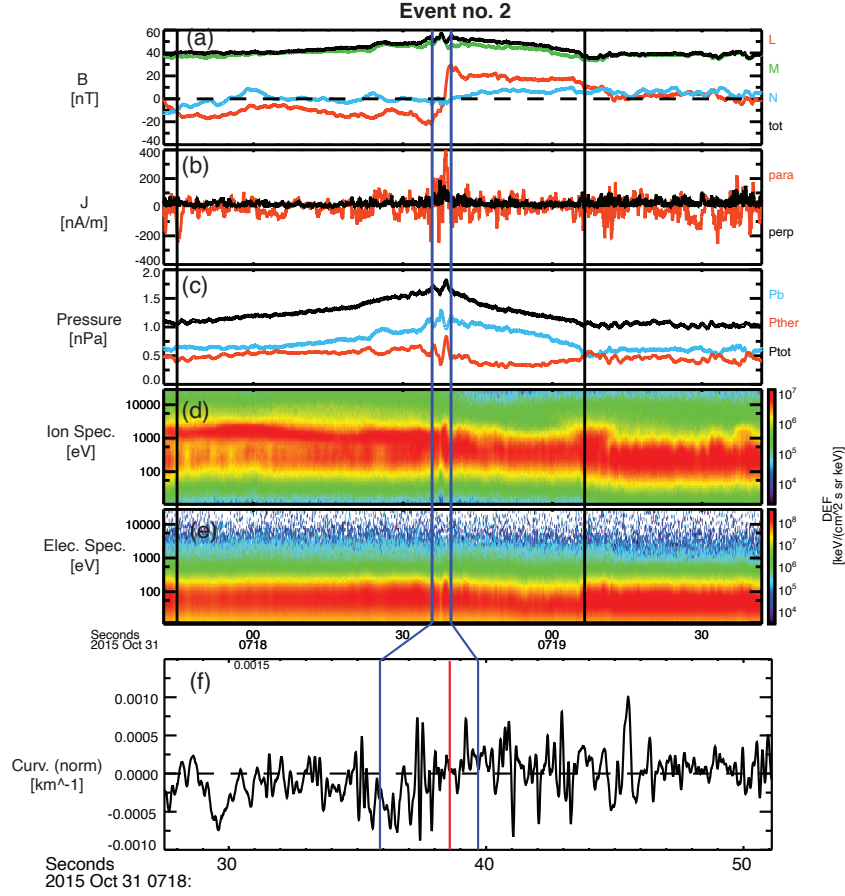
Figure 3.15: Summary plot for event no. 2. (a) The four-spacecraft-averaged magnetic field, (b) the current density, (c) the pressure, (d), (e) the ion and electron energy spectrogram in a wider time range to demonstrate the full entanglement (pressure enhanced) region as marked by the black vertical lines. (f)The magnetic field curvature projected in the direction of the current sheet normal is plotted in a narrower time interval around the sheet marked by the blue vertical lines. The red vertical line marks the maximum current density location within the current sheet. The LMN rotation matrix is L: [0.94, 0.18, -0.30], M: [0.17, 0.51, 0.84], N: [-0.30, 0.84, -0.45]]

are two events (no. 1 and no. 13) with thin current sheets (close to or smaller than ion inertial length). Other current sheets are thicker, but still thinner than 5 ion inertial lengths. The current sheet ratio is below 7%. This parameter quantitatively describes how "sharp" the field rotation is at the center, and this sharp rotation certainly differs from a smooth

variation, as seen in an isolated stable flux rope. None of these parameters are informative about the temporal development sequences. This implies that flux tube entanglement may happen under varying conditions, like varying flux tube sizes, and/or plasma flow speed.

The total pressure profile in event no. 3 is very symmetric, as are most events: Only 5 out of 17 events are asymmetric (event nos. 7, 10, 11, 12 and 14). This asymmetry may be due to the differences in size and momentum of the two flux tubes. They do not occur as often as symmetric ones. One possible explanation is, if one tube is significantly smaller than another tube, it will easily be overpowered or merged. Under this circumstance, the entanglement process would not last as long, and should be observed less frequently.

In this section, we examine a list of 17 flux tube entanglement events from the first two dayside phases of the MMS observations. Their By-dominated IMF distribution agrees with previous findings. By comparing their similarities and differences in the magnetic field curvature, total pressure, and existence of hot electrons, we select eight events to showcase the temporal evolutionary features of three stages. They show that mid-stage entanglement events usually have the clearest bipolar signature in the curvature normal component, and a strong total pressure increase ($> 100\%$). Early-stage and late-stage entanglement does not have the bipolar variation in curvature and has less significant pressure enhancement ($<100\%$). In late-stage events, energetic magnetospheric electrons appear either before or after the central current sheet crossing, indicating that one set of field lines is almost closed (having two ends on the Earth), and a new pair of flux ropes is about to be born.

3.4 Magnetic Entanglement in Magnetohydrodynamic Simulations

3.4.1 Introduction

Magnetic reconnection, the process in which magnetic fields of opposite polarity annihilate and reconnect converting magnetic energy into kinetic energy, has long been a classic topic of research in plasma physics. In addition to its ubiquity and explosive energy release, at the magnetopause, the change in magnetic field topology during magnetic reconnection

allows particles from the solar wind and the magnetosphere to mix. Such mixing, as well as the topological change itself, is believed to be the major channel for mass and momentum exchange on a global scale.

As we have introduced in the previous sections, on the day side of the magnetosphere, magnetic reconnection is often associated with a commonly observed phenomenon called the flux transfer event (FTE), characterized by the magnetic field in the form of a magnetic flux rope (Russell & Elphic, 1979). Four different theories have been proposed to reconstruct/generate their global topologies, and it is not yet observationally settled which mechanism is operative. Three mechanisms are summarized by Fear et al. (2008): The original connected flux rope model (Russell & Elphic, 1979); the magnetic island model, often called the multiple X-line model (Lee & Fu, 1985); and the outflow-region bubble model requiring a single x-line (Scholer, 1988; Southwood et al., 1988), which is later associated with "crater" FTEs when spacecraft encounters the separatrix of reconnection (Trenchi et al., 2019). A fourth type is the proposed magnetic reconnection induced by flow vortices, such as modeled by Dorelli & Bhattacharjee (2009), and supported by a number of observations like Liu & Hu (1988); Zhang et al. (2011) and references herein.

Numerous modeling efforts have attempted to self-consistently generate FTEs in a global three-dimensional (3-D) magnetosphere to understand their formation, including Magnetohydrodynamics (MHD) models relying on ad hoc or numerical resistivity to initiate magnetic reconnection (e.g., work of Fedder et al. (2002); Raeder (2006)), and a hybrid particle-fluid model (Tan et al., 2011). These mostly favor the magnetic island explanation (Lee & Fu, 1985).

With the launch of the magnetospheric multiscale (MMS) mission in 2015, in situ plasma and field measurements at the magnetosphere with high time and spatial resolution have become available at the corners of a tetrahedron with side length as small as 7 km (Burch et al., 2016). Magnetic reconnection processes are now being extensively studied using the MMS data.

As part of the magnetic reconnection studies enabled by the MMS measurements, FTEs

have been substantially studied in recent years. Among these, interaction between multiple flux ropes/tubes has been inferred: Øieroset et al. (2016) observed reconnection inside a flux rope, proposing two merging flux ropes as one possible explanation; Kacem et al. (2018) reported an event consistent with "interaction of two distinct flux tubes"; while Øieroset et al. (2019) examined more events that are consistent with two magnetic flux tubes interlinked with each other. On the other hand, statistical study found the flux ropes of FTEs are either filled with or devoid of hot magnetospheric particles (Russell & Qi, 2020). The structural and composition studies in turn led to the hypothesis that the flux tubes of FTEs were not created singly but at multiple sites on the magnetosphere. The originally disparate flux tubes then collide and merge, producing a pair of flux tubes with axis approximately perpendicular to each other (entanglement), via a second round of magnetic reconnection (Russell & Qi, 2020). Following this hypothesis, multiple cases consistent with the early, middle, and late stages of time evolution of such FTE reconnections have been identified in the MMS data obtained between 2015 and 2018 (Qi et al., 2020).

The realization of the importance of flux tube entanglement is not new. In theoretical treatments, "interlinked" flux tubes have been repeatedly depicted since the pioneering visualization work by (Hesse et al., 1990), using analytical functions of prescribed currents, and sketched by Otto et al. (1991), based on multiple MHD simulation results. Later, in more sophisticated models, magnetic field lines underwent multiple reconnection and produced flux ropes in which all magnetic field connectivity options were possible (e.g. Tan et al. (2011)). The Cluster observation of time evolution with a resolution of a few minutes (Pu et al., 2013) appeared to be consistent with the interlinking theory. In contrast, events found in MMS observations consist of compression on both sides with a current sheet in the middle. This configuration is consistent with two magnetic flux tubes merging at their interface (Øieroset et al., 2019; Qi et al., 2020).

The coalescence of two parallel flux ropes have been observed using the MMS data (Zhou et al., 2017). Now how do they interact when their axes are perpendicular to each other (entangled) during the encounter? In this study, we have designed a numerical local-interaction

model that shows the 3-D evolution of such entangled flux rope/tubes with several distinctive conditions. Following this introductory section, Section 3.4.2 and 3.4.3 explains our model and numerical methods, and Section 3.4.5 – 3.4.6 show our results, while Section 3.4.7 summarizes this study with discussion and applications.

3.4.2 The Physical Models of the Four Simulation Cases

We consider both flux rope-flux rope and flux tube-flux tube interactions to cover both possibilities. In addition, we consider two different driving mechanisms: the ambient plasma's converging motion, and the dragging exerted by the flux tube foot points'motion. This provides us with four different interaction scenarios in total to examine the magnetic entanglement process.
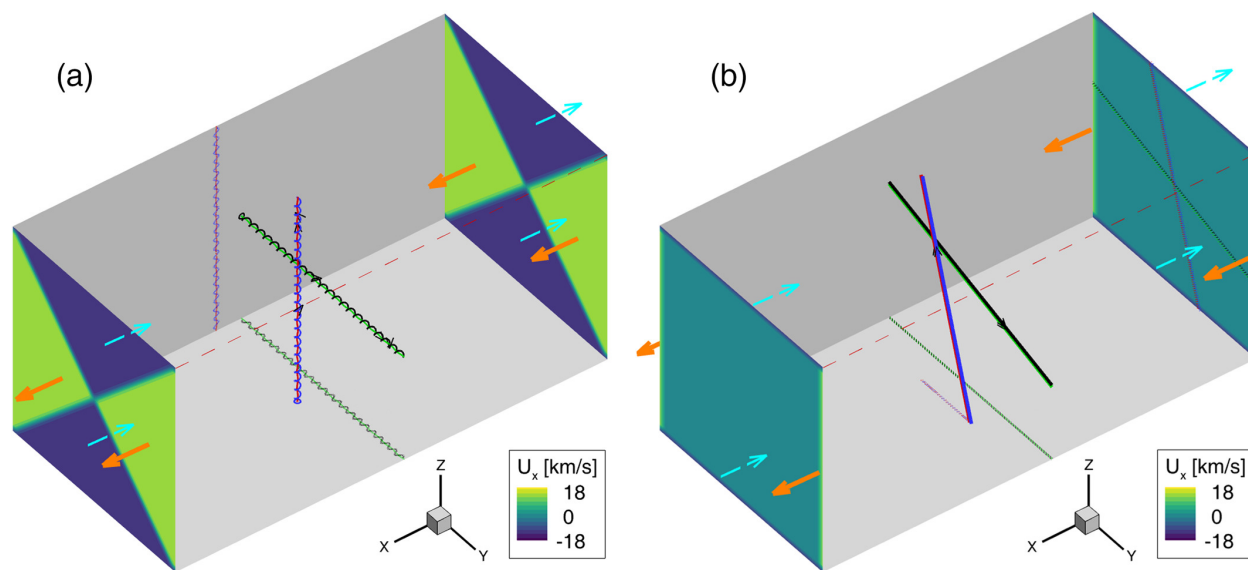
Figure 3.16: Two types of initial and boundary conditions of the simulation domain plotted in 3-D view. Left panel (a): Case A1, magnetic flux ropes at the center, forced flow for both the initial condition and at the x = max/min boundary. Right panel (b): Case B2, flux tubes at the center, dragged by the flow at the side boundary. Colored lines in the middle are indicative of magnetic field lines: Red-blue in flux rope #1, green-black in rope #2. Their projections are shown on two surfaces with dashed lines of the same color. Orange and cyan arrows mark the flow directions at the root of the arrow.

We employ a Cartesian calculation domain of $51.2 \times 25.6 \times 25.6\ R_E$. The x-axis is along the initial flow direction, while y and z are two arbitrary right-hand orthogonal directions for the initial flux-rope alignment. As shown in Figure 3.16, we first place two flux ropes perpendicular to each other, at $d_0 = \pm 1.5 R_E$, respectively. Initially, the plasma density and temperature are a uniform $10/cm^3$ and $2 \times 10^7 K$, respectively, which is similar to the background conditions during the entanglement event on November 07, 2015 (Kacem et al., 2018). We refer to this event as the November 07 event hereafter. This condition approximates a sound speed of ~ 520 km/s, ion thermal velocity of 300 km/s, and an ion inertial length of 70 km, or $0.01 R_E$. The background magnetic field is 0 nT, and the flow velocity is 0 km/s, except as defined by the initial conditions (ICs) and boundary conditions (BCs).

Initially, we use the force-free cylindrical model to simulate each of the two flux ropes (Lundquist, 1950):

$$B_{r'} = 0,$$
$$B_{\phi'} = HB_0 J_1(\alpha r'/R_0), \tag{3.2}$$
$$B_{z'} = pB_0 J_0(\alpha r'/R_0)\ when\ r'\ \leq\ R_0,\ B\ =\ 0\ when\ r > R_0,$$

where r', ϕ', and z' are local poloidal coordinates with z' being the direction of the axis of the flux rope, $H = \pm 1$ is the handedness, or chirality of the helical magnetic vectors, $p = \pm 1$ is the polarity of the core field, J_0 and J_1 are the zero- and first-order Bessel functions, R_0 is the radius of the flux rope, and constant $\alpha = 2.405$ defines the ratio between azimuthal component and axial component (Imber et al., 2014). Unless specified in test cases for comparison, we choose $H = p = 1$ for both flux ropes.

In MMS observations, an entanglement event typically lasts 10–100 s, in a 100 km/s magnetic sheath flow (Qi et al., 2020), so the average radius of one of the two compressed flux ropes is about $0.25\ R_E$, smaller than that of a stand-alone FTE measured and modeled in pre-MMS era models, which may extend up to a few R_E . In this study, we set the radius $R_0 = 0.4\ R_E$, which is between the recently observed ion-scale FTE size and the size used in traditional models. The coordinate conversion from local cylindrical to Cartesian

	BC case A: Dynamic Pressure	BC case B: Tension force
IC type 1: Flux rope	Case A1	Case B1
IC type 2: Flux tube ($B_\phi = 0$)	Case A2	Case B2

Table 3.3: comparison of the four cases: each is a combination of two types of initial conditions (ic) and two types of boundary conditions (bc)

coordinates is achieved by rotating z' to the desired direction: For flux rope #1, z' is parallel to the Cartesian z-axis, and its axis crosses point (1.5, 0, and 0) in unit of R_E , while for flux rope #2, z' is parallel to the y-axis, and crosses (-1.5, 0, and 0) R_E. After the real-time simulation has started, the two flux tubes are driven against each other by boundary conditions so that they become entangled.

As summarized in Table 3.3, two types of initial conditions are adopted based on Equation 3.2: The initial conditions of each of the flux ropes in Case 1 are defined by Equation 3.2, while the flux tubes with Case 2 initial conditions were modified from Equation 3.2 by setting $B_{\phi'} = 0$. In addition, both flux tubes with Case 2 initial conditions are tilted inside the y-z plane by an angle of 16.7°, away from each other, to facilitate reconnection. For the plasma inside the tubes of all cases, a constant bulk flow velocity of $u_0 = -\sin(d_i) \times 13$ km/s is assigned along the x-axis, where subscript i runs through flux ropes 1 and 2.

As also summarized in Table 3.3, two different boundary conditions are applied to move the magnetic flux tubes: Case A simulates two flux ropes/tubes being pushed against each other by the dynamic pressure of the ambient plasma. Cases A1 and A2 divide the entire domain into four regions, and use both the initial and boundary conditions to maintain the flow with speed u 0 in these regions, respectively. Specifically, as plotted in Figure 3.16 panel (a), both $x = x_{min}$ and $x = x_{max}$ boundaries have inflow and outflow conditions. On the other four sides, where y and z are at their minimum and maximum values, floating boundaries are applied, where the boundary value equals the value in its adjacent cell located in the opposite direction of the boundary normal. Accordingly, this floating boundary is a zero-gradient boundary.

The Case B boundary simulates two flux ropes/tubes being pulled against each other, i.e. the interaction is driven by magnetic tension force propagated from the distant end of the flux ropes/tubes. Cases B1 and B2 employ velocity u_0 at both ends of the flux ropes/tubes as a side boundary condition, while the plasma outside the tubes is initially stationary. Specifically, both y-boundaries force a flow of $+u_0$ in the $+x$ direction, while both z-boundaries are fixed with a flow of $-u_0$. Accordingly, both x boundaries are floating boundaries, to allow inflow, outflow, and stationary conditions determined by their location, as shown in Figure 3.16 panel (b).

3.4.3 The Hall-MHD Equations and Numerical Solver

The ideal MHD model of localized plasma interaction solves for the continuity, momentum, and pressure of the proton-electron plasma, as well as the magnetic induction equation. In addition, Hall terms (Tóth et al., 2008) are added to guarantee a fast reconnection that is achievable by particle-fluid hybrid models or full particle models (Birn et al., 2001). The full set of control equations are written as:

$$\frac{\partial \rho}{\partial t} + \nabla \cdot (\rho \mathbf{u}) = 0, \tag{3.3}$$

$$\rho \frac{\partial \mathbf{u}}{\partial t} + \rho (\mathbf{u} \cdot \nabla) \mathbf{u} = -\nabla P + \mathbf{G} + en\mathbf{E}, \tag{3.4}$$

$$\frac{\partial P}{\partial t} + (\mathbf{u} \cdot \nabla) P + \gamma P (\nabla \cdot \mathbf{u}) = G\mathbf{u} + \eta J_2, \tag{3.5}$$

$$\frac{\partial \mathbf{B}}{\partial t} = -\nabla \times \mathbf{E}, \tag{3.6}$$

$$\mathbf{E} = \mathbf{E_0} - \mathbf{u} \times \mathbf{B} + \eta \mathbf{J} + \frac{\mathbf{J} \times \mathbf{B}}{en}, \tag{3.7}$$

where e is the electric charge on an electron; ρ, $\mathbf{u}$, P is the mass density, bulk velocity vector, and thermal pressure of the plasma, respectively. Vector $\mathbf{G}$ is the gravity force but

remains negligible in our study, and $n = \rho/m$ is the number density of protons, and m is proton mass, and we neglect the electron momentum. $\mathbf{B}$ is the magnetic field vector; $\mathbf{E_0} = 0$ is the exterior electric field on this system, which remains 0 in all our cases; η is a constant electric resistivity that is set to 0 in all cases, except one test case in Section 3.4.4 for comparison purposes; J is the electric current inversely calculated from its induction effect (Ampere's law): $\mathbf{J} = 1/\mu_0 \nabla \times \mathbf{B}$, where μ_0 is the vacuum permeability.

Equations 3.3– 3.7 are solved numerically using the Michigan BATS-R-US code (Tóth et al., 2012), with a grid resolution of 0.05 R_E at the center.

Magnetic reconnection involves large-scale evolution of magnetic topology and fine-scale diffusion. We carefully limit our discussion to the MHD regime, which describes the large-scale plasma dynamics and the magnetic topology, and leave the fine structure for future study.

A few tests have been launched to benchmark the evolution of our system: (1) By setting all B = 0 for a hydrodynamic solution with no magnetic flux ropes, both boundary conditions result in stable laminar flow throughout the calculation domain. The shearing speed stays within less than 4 cells of the prescribed regions. This is expected because the Reynolds number is large in such a vacuum-like collisionless plasma. (2) We also run tests with only a single flux tube to evaluate the effect of the surrounding plasma on the tubes: tests applying the type A boundary condition result in a straight flux tube carried by the flow, while the type B boundary results in a flux tube bent and slipping at the boundaries. Although the plasma contained in each flux tube is given an initial velocity that matches the boundary conditions, they lose their momentum if the surrounding plasma is stationary.

The magnetic field strength during the November 7 event is about 50 nT, resulting in an Alfvén speed of 350 km/s, and a proton gyro radius of 60 km, or 0.01 R_E . However, because we initially set B = 0 outside the flux tubes, even with 0.05 R_E resolution, the flux ropes will dissipate during the simulation, so a flux rope with magnetic field strength as strong as this event cannot be sustained in our simulation. Instead, even when we set the initial field strength to B = 80 nT, the magnetic field magnitude drops to about 4 nT with

or without the entanglement interaction. Also, in cases A1 and A2, because the surface field is dissipating to the zero-field region, the magnetic $B_{\phi'}$ component decreases more quickly than the axial component, thus the flux ropes appear less "twisted" around the rope axis during the evolution. Our test shows that the field diffuses much more slowly in lower plasma temperatures (i.e., T = 10^5 K).

3.4.4 Magnetic Flux Rope Reconnection Driven by Dynamic Pressure (Case A1)

After the initial condition of Case 1 shown in Figure 3.16 (a), the time evolution is revealed by Figure 3.17. As expected, most of the flux ropes are pushed by the flow at a constant speed, so the flux ropes remain straight except in the center region, at the entanglement. At T = 20 min, the footpoints of the flux tubes on the boundaries are at $\pm 1 R_E$, respectively. In the meantime, the bent segments of the two ropes extend $\pm 5 R_E$ in y and z coordinates, consistent with an Alfvén speed of 27 km/s. At 40 min, as shown in the right panel of Figure 3.17, the flux tubes did reconnect to form a new pair, comparable to what was sketched by Russell & Qi (2020).

Figure 3.18 shows the reconnection region in close-up snapshots during the evolution of the flux rope-flux rope interaction. Case A1' is a special simulation launched with different settings from the four cases listed in Table 1: We use a domain size of 12.8 $\times$ 12.8 $\times$ 12.8 R_E , with a center resolution of 0.025 R_E , while the rest of the conditions remain the same as those of Case A1. The simulated evolution process remains similar to that of Case A1, indicating that the grid resolution is sufficient in our regular cases.

Panels (a) and (b) of Figure 3.18 show an early stage of this interaction. The ropes are slightly bent by the entanglement interface, while most of the two ropes are not yet merged with each other. Like the initial condition, the system is mostly symmetric in the x-y plane and the y-z planes, respectively. There is a minor asymmetry at the center, arranged by the polarity of the two tubes. In contrast, at t = 30 min, as shown in panels (c) and (d) of Figure 3.18, both ropes are highly bent within a radius of 4 R_E, while newly connected lines recoil
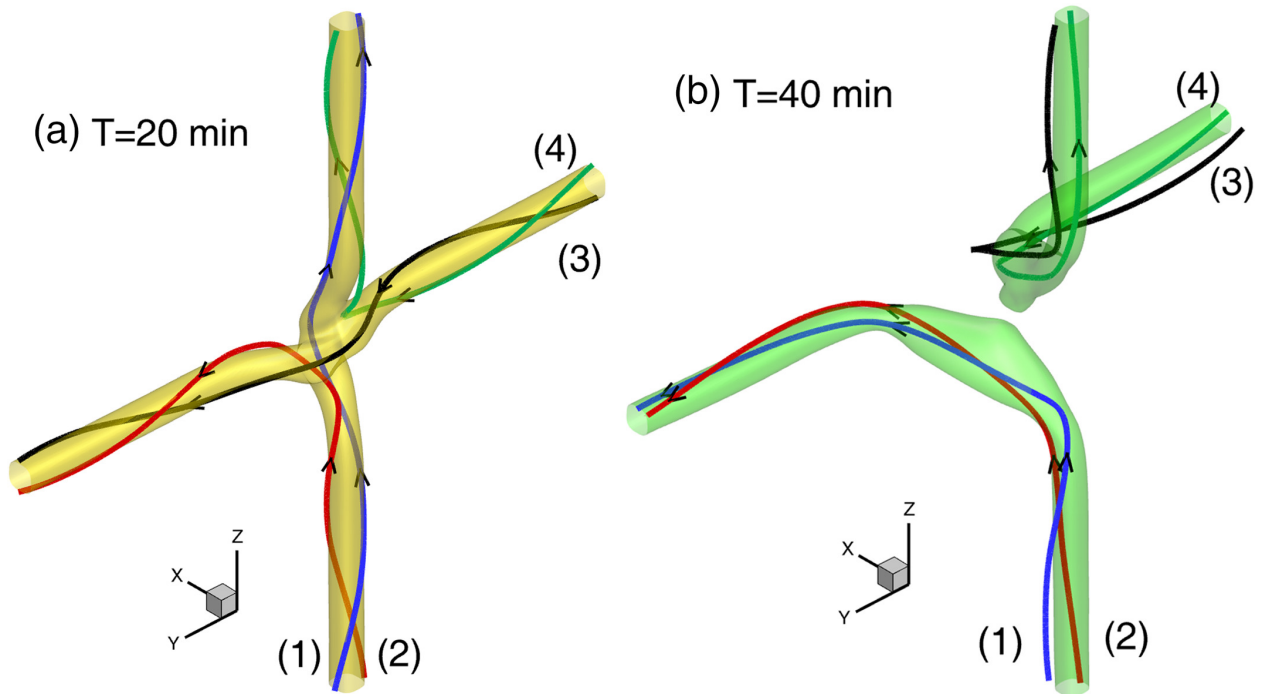
Figure 3.17: Case A1 results at two different times plotted in two different panels, respectively: Two 3-D field line plots of the simulated evolution of the entanglement. A colored surface of constant magnetic field magnitude (panel a, B = 2 nT; panel b, B = 1.4 nT) is plotted to estimate the location of the flux rope. In each of the plots, four representative field lines are traced in 3-D, color coded only so they are identifiable: the vertical field lines used to belong to flux rope #1 of the initial state, while field lines quasi parallel to the y-axis used to belong to flux rope #2
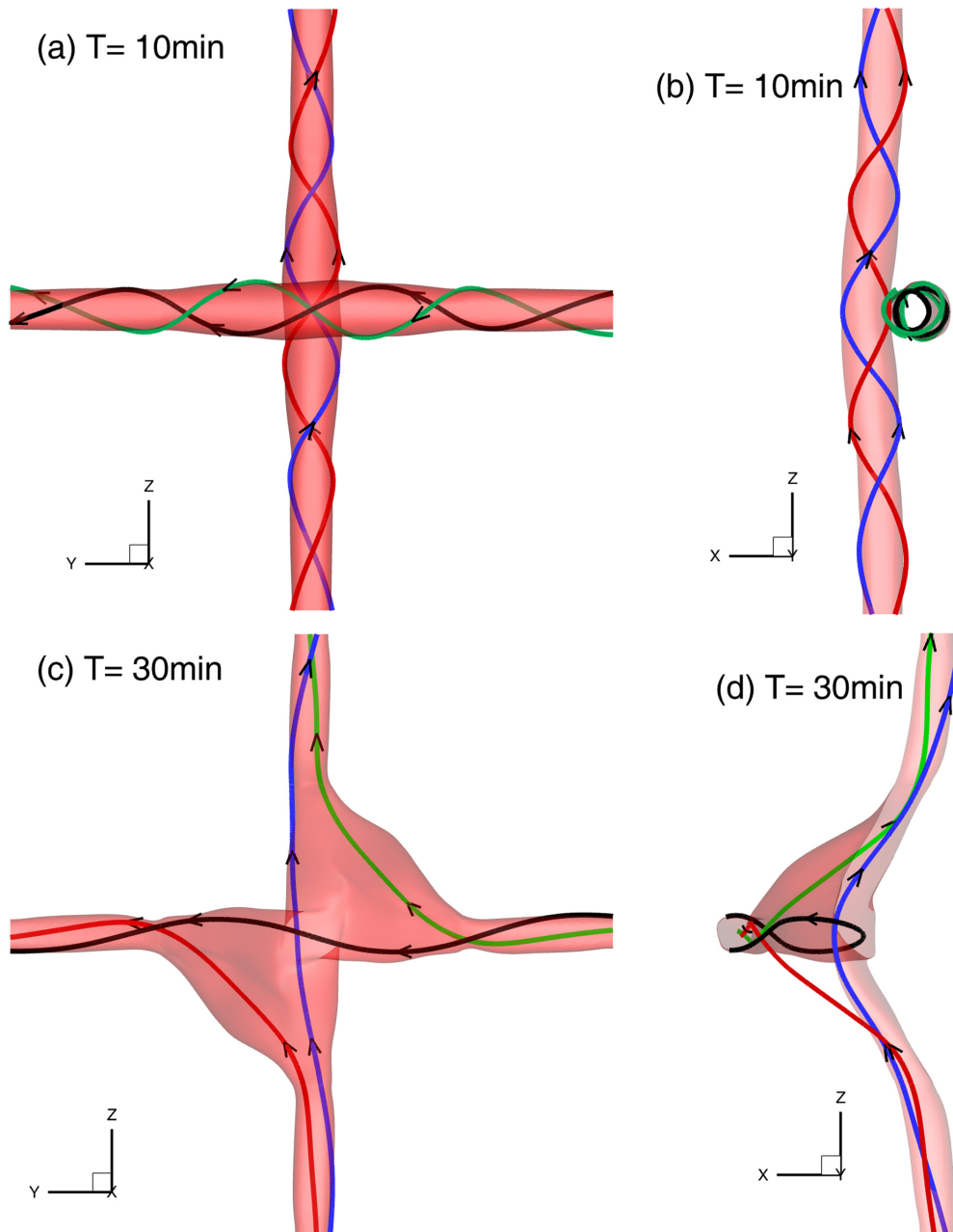
Figure 3.18: Case A1' results at early and late stages in 3-D plot from two different viewing angles. Top panels are taken 10 min after initiation, while bottom panels are at 30 min. All panels exhibit the entire 12.8×12.8 R_E domain. In right panels (b) and (d), the iso-surfaces are cut to show only the y < 0 half, while the field lines are traced in the full calculation domain. From top to bottom, the values of the iso-surfaces are 5 and 3 nT, respectively. Same as figures 3.16 and 3.17, perpendicular field lines originated from flux rope #1, horizontal field lines are from flux rope #2.

and expand the interaction region, making the system no longer symmetric. Compared with the stages at 10 min in Figure 3.18 and 20 min in Figure 3.18, the tubes are now in the late stage of reconnection, with more than half of the flux being reconnected and moving in diagonal directions.

To examine the diffusion region at the interface, the shape of the current sheet in the interaction region at T = 20 min (middle stage) is plotted in Figure 3.19. The current is concentrated in a saddle-shaped layer, which is the expected shape of the interface when the two cylinders merge into each other. In the right panel, viewing along the x-axis, the asymmetry of the saddle caused by the direction of the magnetic field is revealed. In both close up views, two types of magnetic field curvature could show up in this region, depending on the trajectory of detectors: The reconnected lines bend away from the interface, while the piling up field lines bend toward the interface.

Figure 3.20 shows the extracted values of density, plasma thermal pressure, normalized magnetic field intensity, magnetic B_z component, current intensity, as well as magnetic field curvature along the x-axis. Comparing panels a, c, and e, the thermal pressure variation follows well with the density, and anti-correlates with the variation of the magnetic field strength, indicating that the change in magnetic field is compensated by the plasma density.

Because the magnetic field is decreasing with time, to reveal the relative variation of the magnetic field, the field magnitude and B_z component are both normalized by the maximum value of B in the z = 2 plane at the same time. We choose the $z = 2$ plane to stay outside, but still as close as we can, to the compression region. In panel (e) of Figure 3.20, at T = 10 min, the normalized B shows two humps, marking the location of the two ropes, barely merging into each other. At T = 20 min, two ropes have merged significantly, and the normalized magnitude increased above 1 even in the central current sheet, indicating a compression of the magnetic field at this stage. At T = 30 min, the two structures have merged into one and shifted along the -x-axis.

In panel (b) of Figure 3.20, the magnetic field B_z component crossed its zero value only once, and it is asymmetric about the $x = 0$ point, even though the x-axis crosses two flux
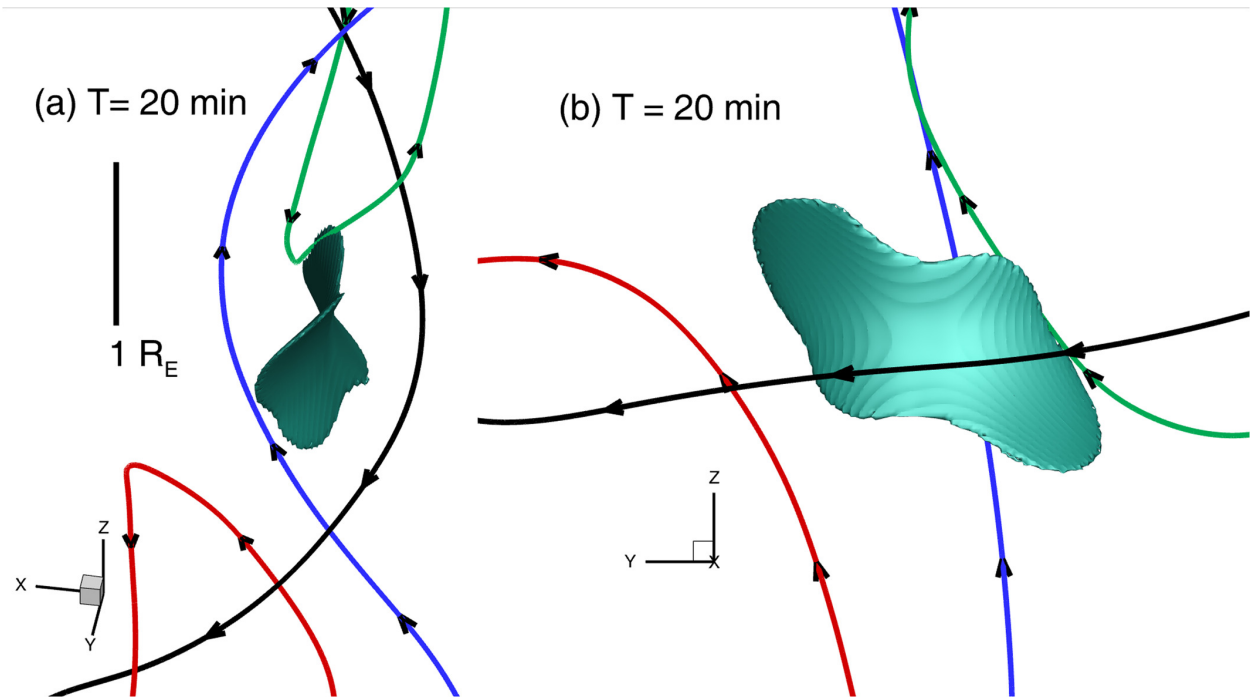
Figure 3.19: Case A1', a close up view of a same set of 3-D field lines from two different viewing angles at T = 20 min. The isosurface represents a current sheet with current density J = 0.004 $\mu A/m^2$. The vertical bar in panel a marks a scale of 1 R_E , and both panels share the same length scale.
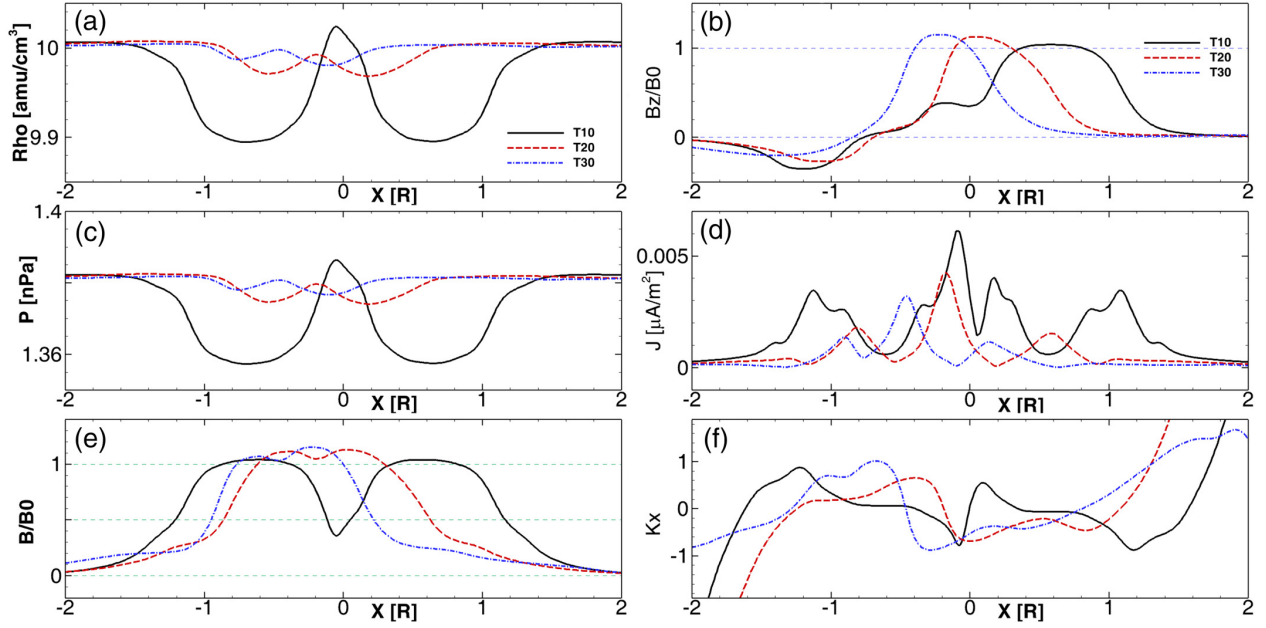
Figure 3.20: Case A1' result, variable values along the x-axis at three different times: 10 (solid lines), 20 (dashed lines), and 30 (dash-dotted lines) minutes after initiation. We note that scales for density and thermal pressure do not include zero, to exaggerate the variation. The magnetic B_{total} and B_z component are normalized by a constant B_0, which is the maximum value of B at $z = 2R_E$ at that instant. In panel (f), the 3-D curvature κ of the magnetic field is projected along the x-axis, which is approximately the normal of the central current sheet.

ropes. The negative trench marks the azimuthal field of the evolved form of flux rope 2 from the initial condition, while the positive hump is the axial field of an evolved form of flux rope 1 in the initial condition.

In panel (d) of Figure 3.20, at T = 10 min, five peaks of current density are seen. The center peak is in the central current sheet, which is the reconnecting current sheet. The four smaller ones on both sides are the flux rope surface current associated with the core field. At T = 20 min, two of the small peaks merge into the central current sheet, while the other two fold toward the center. At T = 30 min, the flux ropes are reconstructed, while the current perturbations move anti-parallel to the x-axis. In general, the state variables do show the merging of two flux ropes, but the values depend highly on the trajectory.

The curvature of magnetic field lines is defined as $\kappa = \mathbf{b} \cdot \nabla \mathbf{b}$, where $\mathbf{b} = \mathbf{B}/B$ is a unit vector along the magnetic field. As shown in Figure 3.19, the current sheet normal is mainly along the x-axis, so we choose κ_x to show the magnetic field curvature in panel (f) of 3.20. At T = 10 min, the curvature shows two pairs of bipolar signatures, consistent with the transverse crossing of the two unmerged flux ropes. Later at T = 20 and 30 min, as is plotted in 3-D in Figures 3.18 and 3.19, and observed by Qi et al. (2020), the field lines, instead of curving toward the individual flux rope axes, curve toward the central current sheet, consistent with the picture that the two ropes are actively pulling against each other.

To further investigate the conditions for reconnection, the following tests have been performed but are not plotted here: By removing the Hall terms from the Hall-MHD Equations 3.3–3.7, and setting $\eta = 0.005$ (Birn et al., 2001), the reconnection process is similar to that shown in Figure 3.17, consistent with this high beta condition that flow drives the magnetic field reconnection. Even with no Hall terms or constant resistivity, the reconnection still occurred via numerical diffusion. To accurately evaluate the influence of numerical diffusion, it is necessary to experiment varying grid size with the same initial setup and we will include this into future work. To confirm the effect of beta, we launched test Case A1b, with the only difference from the Case A1 condition being the plasma temperature of 105 K, which is the interplanetary solar wind condition instead of the nominal magnetosheath value. Not

shown here, the two tubes remain entangled after 50 min from release, indicating that even with Hall MHD, the reconnection rate is insufficient to reconnect the amount of flux in such low beta conditions. We note that for the cases compared, applying the Hall term or not does not change the conclusion.

3.4.5 Magnetic Flux Tube Reconnection Driven by Dynamic Pressure (Case A2)

With the case A boundary conditions and the Case 2 initial conditions, Case A2 is modeled in the same grid system as that of Case A1. As shown in Figure 3.21, the reconnection of flux tubes is complete after 40 min, comparable with that of Case A1. In addition, compared with Case A1, both initial conditions result in a small magnetic $B_{\phi'}$ component, so the observed helicity in the flux ropes may come from other processes.

For this type 2 initial condition, both flux tubes are tilted by an artificial angle of 16.7°. We have launched two test runs to investigate the effect of this angle: Case B10, with this tilting being 0 °, the reconnection still occurs with a similar process. Case B13, with the tilt being -16.7°, the reconnection evolves more slowly, because it took the two tubes, defined by the magnitude of the magnetic field, over 50 min to become mostly reconnected and separated. Earlier, using the same BATS-R-US code but not including the Hall terms nor uniform resistivity, Jia et al. (2007) have found no significant reconnection when two regions with magnetic field perpendicular to each other are merging in a nominal solar wind condition. Together with Case A1b, we speculate that the difference in the effectiveness of reconnection at different guide field percentages relies on the plasma conditions, scale lengths, wave speed, and plasma β, as has been extensively studied (e.g. work by Phan et al. (2010) and Scurry et al. (1994)).

3.4.6 Interactions Driven Only by Magnetic Tension Force (Cases B1, and B2)

The time evolution of initial conditions type 1 and 2 are simulated again by pairing with the type B boundary condition. The results are shown in Figure 3.22. Even after 2 h, neither
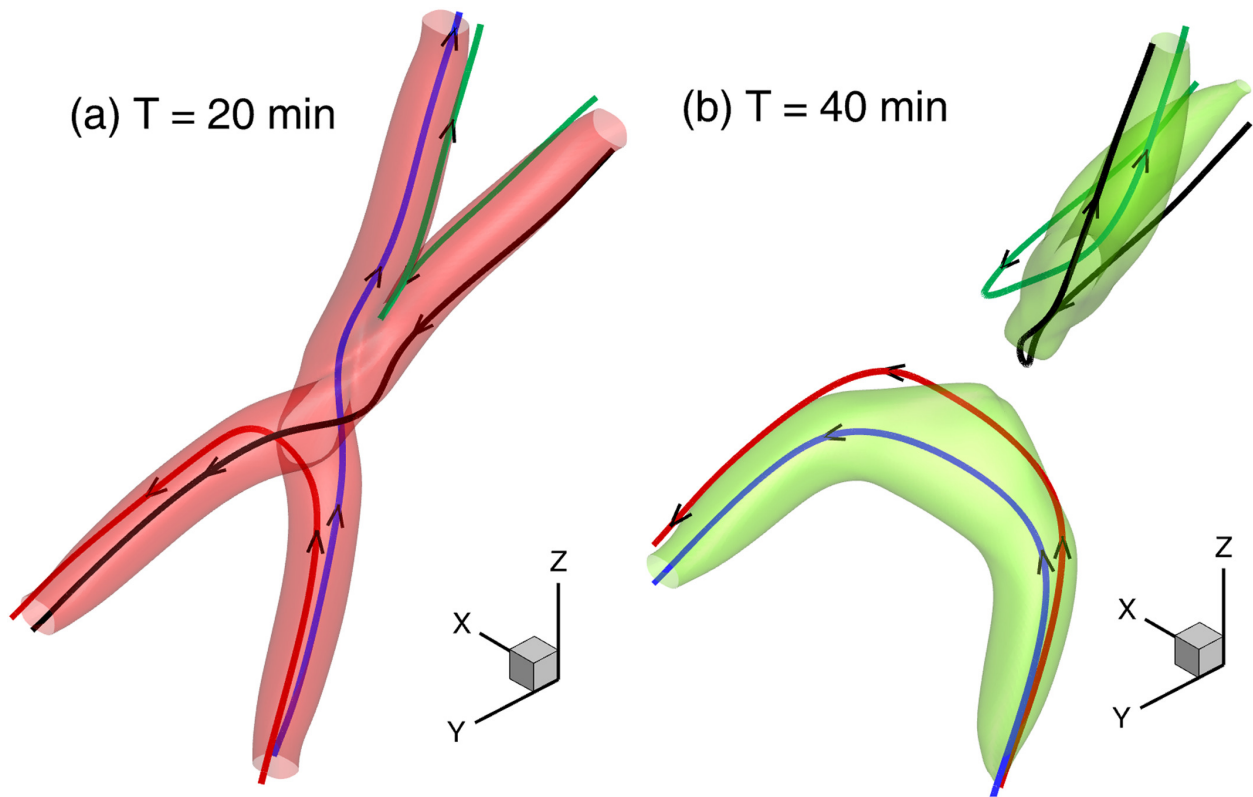
Figure 3.21: Case A2, interaction of two flux tubes driven by the flow. Shown are 3-D plots at the same viewing angle as that of Figure 3.17, with a surface marking the region with a non-negligible magnetic field. Four representative magnetic field lines are traced in 3-D to show the topology of the magnetic field during the interaction. Left panel: Iso-surface at B = 4 nT at 20 min after initiation. Right panel: Iso-surface of B = 1.6 nT at 40 min after release. In the positive y sector, the bottom two field lines belong to the initial flux rope #1, while the two higher field lines that touch the $+y$ boundary belong to initial rope #2.

ropes or tubes are fully reconstructed. For both cases, the drag from the side boundaries is insufficient to reconnect the flux ropes/tubes, even though weak reconnection occurred in weak field regions surrounding the flux ropes/tubes. The spherical structures shown in iso-surfaces close to the boundaries are footpoints of the flux tubes, driven by the boundary conditions. They appear disconnected from the central segment of the iso-surface at T = 2 h, indicating the diffusion mainly happened here close to the boundaries. Even in this highly diffusive plasma, the reconnection rate driven by the tension force passed along the flux tubes from the boundaries, is not fast enough for the two tubes to reform before the two ends pulled by the boundaries travel too far. Thus most of the energy is lost close to the boundaries, instead of reconnecting in the center.

3.4.7 Discussion and Conclusions

Comparing Cases A1 and A2, we have found that the reconnection is fast enough for the two tubes, whether originally with or without twist, to reconnect in 40 min. In reality, this is close to the amount of time for a magnetic flux tube to travel from the day side to the night side, so an upper limit of 40 min is a good estimate of whether the reconnection of flux tubes will occur in our model or not.

We admit that the selection of the velocity of 13 km/s is arbitrary. In contrast, the flow vortex around FTEs is usually on the same order (Zhang et al., 2011), while the flow speed that carries this entangled structure is one order of magnitude greater during the November 07 event. The flow fluctuations during this event are also about 100 km/s, giving an upper limit to the relative velocity between two flux tubes. Our test shows that this relative speed will affect the speed of evolution; a relative speed of 26 km/s results in a completion of reconnection in 20 min. Hence, for a speed at this magnitude, the plasma condition is sufficient for a reconnection to occur, and fast enough to reconnect the magnetic flux in tens of minutes.

During reconnection, the peak magnetic field strength drops to about 3 nT. Although actually a 50 nT field is measured, the total flux enclosed in a 50 nT flux rope of 0.1 R_E

radius is comparable to the total flux in our 3 nT flux rope with a 0.4 R_E radius, indicating that our result is applicable to real flux tube/rope reconnections interpreted from MMS observations. On the other hand, such field diffusion may be constrained by tweaking the thermal pressure balance across the tubes, and we leave this study to future modelers.

On the other hand, by comparing the results from type A and type B boundary conditions, despite the diffusion of this high-β plasma in our simplified simulation, we find that this reconnection, if it happens, would be driven by the dynamic pressure of the ambient flow, instead of tension from distant locations, due to diffusion of the magnetic field stress in the magnetosheath.

Our Case B results in two different types of plasma, one with temperature 10^7 K and the other 10^5 K, suggest that propagation of magnetic tension relies on the plasma condition, or plasma β. We note that this case B scenario is comparable to the driving of flux tubes/ropes in the corona, where the dense and turbulent photospheric plasma dictates the motion of the footpoint of coronal magnetic field (Jokipii & Parker, 1968), causing shearing, twisting that leads to eventual mass and energy release of various scale (e.g. Ballegooijen et al. (2014)).

For cases with type A boundaries, the disturbance stays within ± 5 R_E , which is the region in which we are assuming uniformity. Nonetheless, a more complicated real situation may exist at this scale, i.e., the flux tubes could be bent, both the field strength and helicity of the flux tubes may vary along their axis, and the entangled flux tubes may undergo other processes when they move through the plasma in the magnetosheath before they collide with each other.

In Equation 3.2, we adopted a parameter H to represent the sign of helicity of the flux ropes in our initial conditions, and it was set to 1 in all flux rope cases. We run case A1 again with $H_2 = -1$ in flux rope #2, and the evolution process is comparable to the Case A1 result. The relative polarity of the axial field also does not matter to the timing of reformation: We have reversed the axial field of flux rope #2 by setting $p_2 = -1$, the flux ropes rematch to form new pairs, and the asymmetric extended interaction region has changed accordingly, but the general process evolves with similar timing. In addition, the distribution of twisted

field and core field in the flux ropes may also affect the general reconnection of these tubes, more modeling work is needed to probe these parameters. Further, in all cases, we have assumed symmetric entanglement, where the magnetic fields in the two flux tubes share the same magnitude. From our model result, we would expect the stronger one to cut through the weaker one, but more simulations are needed to confirm our speculation. We have also assumed symmetry between the two ends of a flux tube. They may not only be bent, but also sitting in plasmas of different states, and moving at different speeds. In contrast to the guide field study with case A2, for case A1 we have assumed perpendicular interaction between two ropes. Combined with chirality and polarity of the flux ropes, how does this angle affect the result? These above possibilities call for more local models, to probe with more conditions and wider range of parameters, as well as global models with resolution sufficiently fine and self-consistently generating such interactions.

Flux rope interactions have been studied for decades in the solar corona, as recently reviewed for models by Keppens et al. (2019), and for observations by Liu et al. (2020). Such interactions are ubiquitous in solar eruptions, including filaments, prominences, and the release of coronal mass ejections. For flux rope interactions in a typical low-beta solar corona, a related study has been performed using a 3-D resistive MHD model. When investigating the interaction of two flux ropes of various relative angle, helicity, and polarity, Linton et al. (2001) used a solenoidal velocity field to find many different interaction modes, among which, their "slingshot mode" that reconnects into two new ropes is the most comparable with our case A1 result, also supporting the feasibility of flux rope reconnection in general. Our Hall MHD model, on the other hand, after changes in parameters and conditions, may apply to the coronal environment for flux rope interactions, and more sophisticated arch twisting evolutions (e.g. work done by Török & Kliem (2005)).

In addition to the slingshot mode, Linton et al. (2001) have also found three more possible fundamental modes of rope-rope interactions: Bouncing, merging, and tunneling, depending on the relative handedness, and angle of impact. Among these, merging is commonly studied as coalescence in the Earth magnetosphere, when the two flux ropes are parallel at the

interface (e.g. Zhou et al. (2017)). We note that the foot points of the flux ropes in the Linton model are not moving, while in contrast, those of the terrestrial flux ropes are often free to move across each other, so bouncing is not allowed in our current simulation. On the other hand, the reason that we did not observe tunneling interactions is due to our loss of helicity during the interactions, i.e., the flux ropes are stretched almost to flux tubes in the interaction region. More detailed studies on such different interaction channels, conditions, and that links rope-rope interactions in the solar corona and magnetospheres is a necessary next step in such simulations. Last, the real solar wind-magnetosphere interaction might be patchy and sporadic at this sub-R_E scale. As stated in the introduction, despite the large amount of literature that envisions such entanglement of flux tubes from both theory and observations, there also exists a considerable amount of literature explaining FTEs otherwise, including the events observed by MMS (Qi et al., 2020).

In summary, our study presents a reconnection process of two flux ropes/tubes in the Hall MHD regime, driven by ambient plasma flow of the magnetic sheath conditions. Our model visualizes the evolution of the interaction region, and predicts the encountering of opposite magnetic curvature along different trajectories. Based on model results, we recommend surveys in the MMS magnetic field data to reconstruct the 3-D shape of early and late stages of the flux rope/tube entanglement, using the plasma data as an indication of connectivity to confirm the stages. Finally, we emphasize that application of our idealized model should apply not only to magnetospheric reconnection, but also to flux rope interactions in the solar corona.

(a) T = 20 min

(b) T = 2 Hrs

(c) T=00:20m

(d) T=02h:00
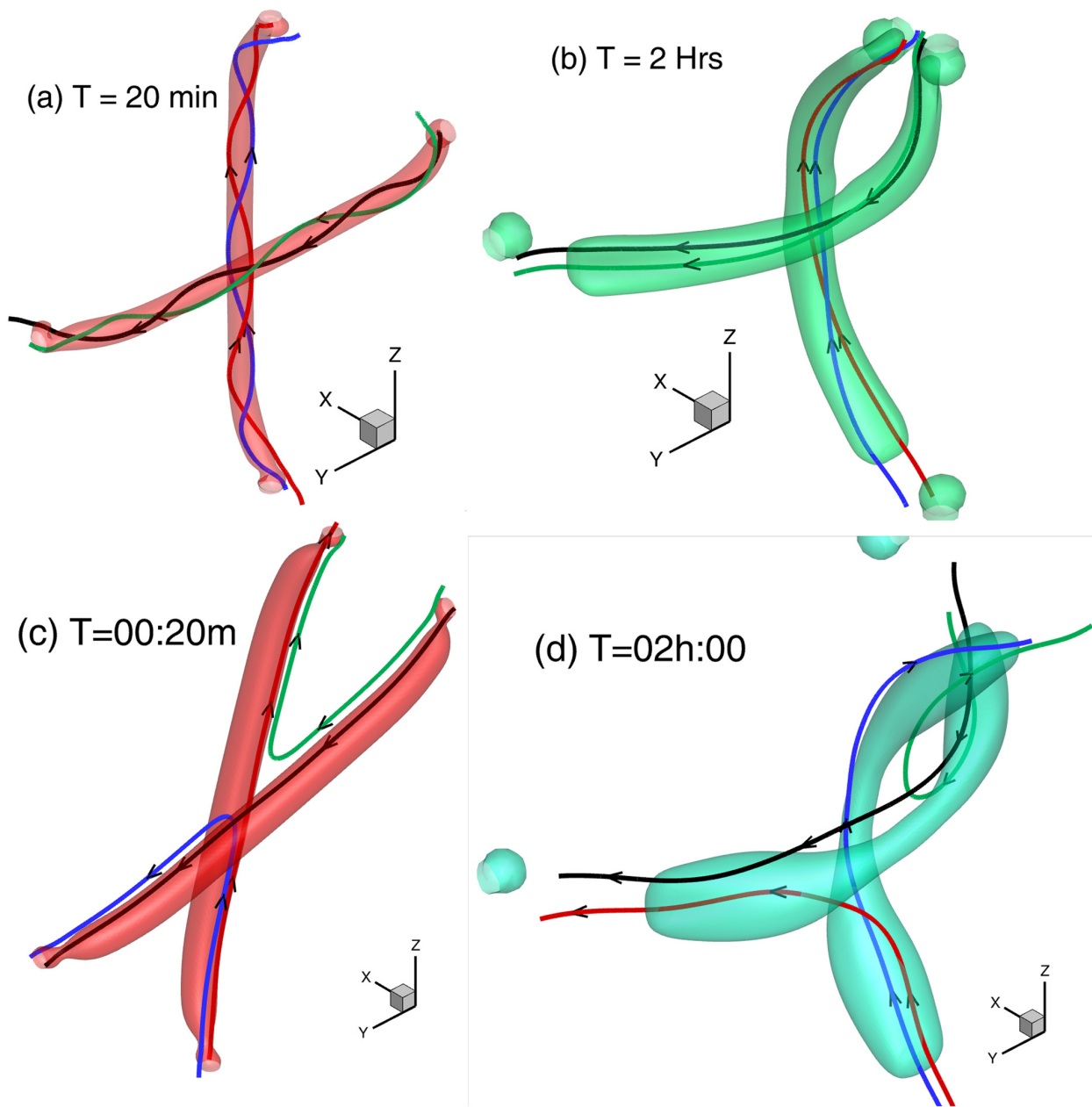
Figure 3.22: 3-D plot of Cases B1 and B2 results in the same viewing angle as used in figures 3.17 and 3.4.5. Top panels show the results of case B1, while the results of case B2 are shown at the bottom. Left panels show 20 min with iso-surface of magnetic field magnitude B = 3 nT, while right panels show time = 2 h, with iso-surface B = 1 nT.

CHAPTER 4

Conclusion and Future Work

The concept of reconnection was proposed decades ago but there are still numerous questions in relation to magnetic reconnection that are under open discussion. One challenge is to locate the reconnection site both accurately and efficiently. With our growing understanding of magnetic reconnection and the complexity of the diffusion region, we can investigate various methods to improve the identification of active reconnection. In this dissertation we presented the results of utilizing magnetic curvature analysis and developing Magnetic Flux Transport (MFT) technique to assist or advance identifying active reconnection.

Another related problem is how the reconnected magnetic flux joins the terrestrial magnetic field. The Flux Transfer Events (FTEs) based on the ideas that flux ropes generated by reconnection carry the flux away with their motion provides us with a clear and straightforward picture of how the flux convection occurs. However, the real process could be more complicated. We explored the magnetic entanglement which can happen when field lines of different polarity encounter and pull against each other, during which reconnection could happen at the interface to modify the field line's connectivity and simplify the entanglement.

In Chapter 1, We focused on the identification of magnetic reconnection. In Section 2.2, we explained the theory of magnetic curvature analysis and the reason why the radius of curvature could be used to demonstrate how strongly a species of particle are magnetized. By comparing the spatial scales of the particle's motion and the magnetic field's variation (here are the gyro-radius and the radius of magnetic field curvature), we can define this scalar parameter κ to quantitatively indicate whether electrons and ions are diffusive. We tested this analysis in two previously reported EDR crossings and confirmed that the curvature

parameter can demonstrate the desired characteristics. The curvature analysis is more useful in identifying thin current sheets regardless of the existence of active reconnection.

Phan et al. (2018) reported MMS observations of electron-only reconnection where electrons are energized while ions are not coupled in turbulent magnetosheath. Later similar electron-only events were discovered in the magnetotail (Wang et al., 2018; Hubbert et al., 2021) and it was proposed that the electron-only reconnection is the early phase of traditional ion-coupled reconnection when reconnection is still developing in the electron scale currents (Lu et al., 2020b). Moreover, in turbulent plasma, the role of magnetic reconnection is still not completely understood, as well as how much dissipation is contributed by magnetic reconnection. Statistical studies on electron-scale currents have been carried out in magnetosheath and suggest the prevalence of electron-scale current sheets favorable for electron reconnection (Stawarz et al., 2019). With the MMS tetrahedron we can investigate the magnetic curvature signatures in these thin current sheets and further examine the correlation between κ parameter and the particle's velocity phase space distribution. In addition, we can use curvature signatures as a tool to search for sub-ion scale current sheets. Similar study has been done in the night side but not on the dayside (Rogers et al., 2019). It will be much faster to use a scalar parameter to filter data initially than to analyze each current sheet manually. And measuring the spatial scale of field variation could be correlated with particle kinetics more easily than simply compute the current density profile's full width at half maximum. With a more comprehensive thin current sheet survey and the corresponding solar wind parameters, it is possible to answer whether there is any preference in location of reconnection onset under certain circumstances and how the occurrence of reconnection is in control of solar wind conditions.

The second technique we used to identify active reconnection was the Magnetic Flux Transport (MFT) analysis. In Chapter 2 Section 2.3 we examined the MFT signatures in two-dimensional gyrokinetic simulations. We observed simultaneous magnetic flux ($\mathbf{U}_\psi$)) inflow and outflow jets in both symmetric and asymmetric reconnection sites. The divergence of the flux transport ($\nabla \cdot \mathbf{U}_\psi$) demonstrates quadrupolar pattern. Compared with traditional

parameters like plasma bulk flow jets and energy conversion rate ($\mathbf{j} \cdot \mathbf{E}'$), the MFT signatures are more localized and less affected by the upstream conditions. This method has the potential to replace the plasma outflow jet reversal signature for reconnection. Applications to 3D simulations and heliospheric observations from spacecraft missions will present new opportunities to study the role of reconnections and identify new types of reconnection in turbulence. In Section 2.4, we applied the MFT analysis in MMS observations. We chose 37 active reconnection-line/EDR crossings that were previously studied and under various plasma conditions. We found that the MFT method successfully identified all reconnection events. In our experiment, it also had a higher rate of success compared to plasma bulk flow characteristics.

In the future the MFT method can be used to search for new active reconnection crossings. Adding the magnetic flux transport analysis can also help reduce the ambiguity when the energy conversion is observed in a thin current sheet but it is hard to distinguish whether it is due to magnetic reconnection or other diffusive process like wave-particle interactions. In addition, like we mentioned earlier, the discovery of electron-only reconnection has shed new light on the reconnection model and added new challenges to our understanding of the microscopic characteristics of reconnection. In this case, the accurate and efficient identification of reconnection is becoming more and more important. To better understand the electron-only reconnection and reconnection in turbulent plasma (e.g., (Gingell et al., 2019, 2020)), we can use MFT analysis to gain more information about the motion of magnetic flux during these processes. The divergence of MFT can indicate the net flux gain/loss rate in the volume confined by the spacecraft constellation. The current MMS separation is small enough to study the microscopic aspects of magnetic reconnection, but it is sensible to expect when we raise the separation we will be able to investigate this signature at larger scales. Correlating this with solar wind observations, we can measure the local magnetic flux variation in different regions of the magnetosphere and compare it with the global magnetic flux convection picture.

In Chapter 3, we present studies on the flux transfer events (FTEs) and magnetic en-

tanglement process. In Section 3.2 we explored the flux tubes on the Earth's dayside magnetopause and proposed the hypothesis that the flux ropes can be born in pairs through magnetic entanglement during which magnetic reconnection takes place at the interface of entangled flux tubes of different polarities and releases the entanglement by modifying the connectivity of the field lines. In Section 3.3 identified three temporal evolutionary stages of magnetic entanglement that can be characterized by the rate of magnetic field build-up and the curvature signatures at the interface. Later, in Section 3.4 we reproduced the magnetic entanglement process under different initial and boundary conditions in three-dimensional Hall MHD simulation. We tested flux tubes with and without magnetic azimuthal components and for both initial conditions magnetic reconnection successfully occur at the entanglement interface. We found the converging plasma flow as an external driver that pushed the two tubes together is important for reconnection to fully disentangle the tubes in the simulation.

To examine the importance of external driver, we will survey the MMS magnetopause observations and extend the time period to the latest dayside phases (2020-2021 winter). In addition to flux tubes that are undergoing the entanglement process, we will also collect closely located flux tube pairs to better understand the pre- and post-entanglement evolution. Another important question that can be answered by a comprehensive survey is the spatial distribution of the magnetic entanglement events as well the distribution of their size. Since the entanglement adds complexity to the magnetic flux convection after the initial magnetic reconnection on the magnetopause, we will also combine MMS observations with ground-based observation to trace any potential global reactions.

Similar interaction between flux tubes has been studied in solar corona (e.g. (Linton et al., 2001)). Recently it is also reported in the solar wind observations by Parker Solar Probe (Fargette et al., 2020b). The magnetic entanglement process seems to be ubiquitous and it is important to compare the similarities and differences of in different plasma conditions. Thus, we will use the 3D Hall MHD simulation to conduct experiments under the magnetopause environment with varying helicities and axis angles between the two flux ropes. Then it is

possible we can expand our study to other planets' magnetosphere to gain a deeper insight into the interactions of magnetic flux tubes and their impacts.

CHAPTER 5

List of Type A and Type B FTEs

Table 5.1: Type A FTE: energetic electrons present

Start time	End time	Center time
2015_1003_10:45:37.385	2015_1003_10:46:52.193	2015_1003_10:46: 9.988
2015_1003_13:27: 8.780	2015_1003_13:27:46.914	2015_1003_13:27:28.215
2015_1003_13:29: 1.581	2015_1003_13:30: 8.516	2015_1003_13:29:37.582
2015_1004_13:41:34.823	2015_1004_13:41:53.480	2015_1004_13:41:42.061
2015_1003_13:44: 9.193	2015_1003_13:46: 5.994	2015_1003_13:44:58.794
2015_1006_09:30:50.931	2015_1006_09:31:18.399	2015_1006_09:31: 1.198
2015_1006_16:02:40.825	2015_1006_16:03:20.672	2015_1006_16:02:59.216
2015_1006_17:28: 9.346	2015_1006_17:28:17.342	2015_1006_17:28:12.811
2015_1008_14:49:41.199	2015_1008_14:50:21.178	2015_1008_14:50: 3.054
2015_1011_10:50:10.819	2015_1011_10:51:11.988	2015_1011_10:50:43.602
2015_1011_12:20:21.344	2015_1011_12:21:43.457	2015_1011_12:20:54.669
2015_1017_12:22:30.811	2015_1017_12:23: 2.245	2015_1017_12:22:49.192
2015_1017_12:32: 0.808	2015_1017_12:33:31.378	2015_1017_12:32:58.189
2015_1019_09:34:39.849	2015_1019_09:34:52.630	2015_1019_09:34:45.412
2015_1019_09:51:21.274	2015_1019_09:51:25.272	2015_1019_09:51:23.245
2015_1020_15:46:27.978	2015_1020_15:49: 7.713	2015_1020_15:47:27.337
2015_1022_13:40:18.712	2015_1022_13:40:47.108	2015_1022_13:40:31.820
2015_1023_12:49:13.847	2015_1023_12:50:21.301	2015_1023_12:49:52.592
2015_1101_03:40:22.144	2015_1101_03:40:50.585	2015_1101_03:40:37.260

2015_1102_14:51:52.988	2015_1102_14:53:33.635	2015_1102_14:52:18.649
2015_1105_14:07: 5.646	2015_1105_14:07:44.231	2015_1105_14:07:25.734
2015_1105_14:47: 8.202	2015_1105_14:47:31.870	2015_1105_14:47:21.328
2015_1111_03:56:30.908	2015_1111_03:57:22.375	2015_1111_03:56:54.108
2015_1117_02:15:30.827	2015_1117_02:16:52.067	2015_1117_02:16:12.509
2015_1117_02:45:59.054	2015_1117_02:46:34.878	2015_1117_02:46:19.367
2015_1117_12:49:14.993	2015_1117_12:49:58.535	2015_1117_12:49:37.062
2015_1202_01:14:47.089	2015_1202_01:14:49.675	2015_1202_01:14:48.121
2015_1205_23:44:54.515	2015_1205_23:46:41.494	2015_1205_23:45:46.396
2015_1209_23:51:40.119	2015_1209_23:51:49.232	2015_1209_23:51:44.313
2015_1214_00:58:57.005	2015_1214_00:59: 0.674	2015_1214_00:58:59.038
2015_1214_06:10:17.590	2015_1214_06:10:46.928	2015_1214_06:10:30.541
2015_1229_09:14:47.905	2015_1229_09:15: 3.300	2015_1229_09:14:52.672
2016_0106_22:27:13.330	2016_0106_22:27:17.339	2016_0106_22:27:15.313
2016_0109_08:43:36.136	2016_0109_08:43:47.811	2016_0109_08:43:43.988
2016_0110_09:01: 4.394	2016_0110_09:01: 6.248	2016_0110_09:01: 5.104
2016_0110_09:05: 3.617	2016_0110_09:05:17.921	2016_0110_09:05:11.933
2016_0111_21:30:40.088	2016_0111_21:30:52.262	2016_0111_21:30:47.239
2016_0128_01:45:39.626	2016_0128_01:46:52.389	2016_0128_01:46:13.475
2016_0131_06:32: 8.295	2016_0131_06:32:33.930	2016_0131_06:32:21.612
2016_0203_05:37:27.688	2016_0203_05:38: 2.077	2016_0203_05:37:46.190
2016_0204_03:11:49.931	2016_0204_03:12:27.605	2016_0204_03:12:10.517
2016_0216_20:34:50.730	2016_0216_20:34:58.731	2016_0216_20:34:54.236
2016_0219_18:40:45.147	2016_0219_18:41:28.738	2016_0219_18:41: 4.153
2016_0220_23:18:39.201	2016_0220_23:22: 4.803	2016_0220_23:19:53.202
2016_0226_01:38:12.527	2016_0226_01:38:43.542	2016_0226_01:38:29.142
2016_0226_01:41:39.542	2016_0226_01:41:50.010	2016_0226_01:41:44.403

2016_0308_01:32:26.004	2016_0308_01:35:30.809	2016_0308_01:33:50.406

Table 5.2: Type B FTE: energetic electrons absent

Start time	End time	Center time
2015_0914_10:17: 3.050	2015_0914_10:17:15.368	2015_0914_10:17: 9.581
2015_0918_08:48:22.136	2015_0918_08:48:24.863	2015_0918_08:48:23.527
2015_0918_08:48:56.265	2015_0918_08:49: 8.825	2015_0918_08:49: 1.332
2015_0925_11:44:15.077	2015_0925_11:44:24.006	2015_0925_11:44:20.008
2015_0927_11:44: 4.206	2015_0927_11:45:22.379	2015_0927_11:44:38.994
2015_1006_16:28:57.118	2015_1006_16:29:37.742	2015_1006_16:29:12.402
2015_1011_12:48:52.593	2015_1011_12:49:30.795	2015_1011_12:49:13.794
2015_1016_13:04:32.387	2015_1016_13:04:36.294	2015_1016_13:04:33.807
2015_1017_15:58:28.114	2015_1017_15:58:54.892	2015_1017_15:58:43.559
2015_1018_15:12:33.365	2015_1018_15:12:37.415	2015_1018_15:12:36.014
2015_1020_05:59: 6.468	2015_1020_05:59:14.223	2015_1020_05:59:10.778
2015_1021_04:40:43.732	2015_1021_04:40:49.691	2015_1021_04:40:46.416
2015_1022_13:39:16.517	2015_1022_13:39:38.655	2015_1022_13:39:28.955
2015_1209_01:06:13.689	2015_1209_01:06:18.368	2015_1209_01:06:16.472
2015_1024_05:05: 9.877	2015_1024_05:05:14.961	2015_1024_05:05:11.971
2015_1024_05:04:36.972	2015_1024_05:04:55.170	2015_1024_05:04:43.812
2015_1027_12:34:28.560	2015_1027_12:35: 7.042	2015_1027_12:34:44.605
2015_1105_04:58:41.796	2015_1105_04:58:49.941	2015_1105_04:58:44.784
2015_1112_07:06: 2.426	2015_1112_07:06: 5.139	2015_1112_07:06: 3.632
2015_1112_07:20:21.107	2015_1112_07:20:34.309	2015_1112_07:20:27.984
2015_1113_04:54:17.009	2015_1113_04:54:22.199	2015_1113_04:54:19.709
2015_1116_14:19:50.234	2015_1116_14:19:59.848	2015_1116_14:19:56.599
2015_1117_08:49:43.078	2015_1117_08:50:31.187	2015_1117_08:50: 1.468

2015_1117_14:20:57.450	2015_1117_14:21: 3.663	2015_1117_14:21: 0.205
2015_1126_13:17:51.555	2015_1126_13:18: 1.035	2015_1126_13:17:56.544
2015_1201_01:39:56.077	2015_1201_01:40: 3.495	2015_1201_01:40: 0.435
2015_1202_10:21:44.784	2015_1202_10:22: 0.821	2015_1202_10:21:53.280
2015_1205_00:40:35.092	2015_1205_00:40:41.025	2015_1205_00:40:37.728
2015_1208_10:21:16.957	2015_1208_10:21:29.172	2015_1208_10:21:22.781
2015_1208_10:27:44.138	2015_1208_10:28: 1.516	2015_1208_10:27:52.674
2015_1208_11:20:16.356	2015_1208_11:20:22.132	2015_1208_11:20:18.829
2015_1209_00:52:37.103	2015_1209_00:52:39.938	2015_1209_00:52:38.075
2015_1214_00:58:38.641	2015_1214_00:58:39.704	2015_1214_00:58:39.082
2015_1208_11:20:32.213	2015_1208_11:20:36.764	2015_1208_11:20:33.573
2016_0110_09:01:16.200	2016_0110_09:01:21.793	2016_0110_09:01:19.270
2016_0110_09:11:50.934	2016_0110_09:12: 1.939	2016_0110_09:11:55.815
2016_0115_02:33:34.643	2016_0115_02:34:12.337	2016_0115_02:33:57.885
2016_0116_01:12:31.755	2016_0116_01:13:14.000	2016_0116_01:12:56.409
2016_0127_22:12:29.728	2016_0127_22:12:31.745	2016_0127_22:12:30.700
2016_0127_23:15: 2.239	2016_0127_23:15: 5.317	2016_0127_23:15: 3.833
2016_0205_19:03: 8.556	2016_0205_19:03:10.457	2016_0205_19:03: 9.600
2016_0211_01:57: 6.963	2016_0211_01:57:16.243	2016_0211_01:57:10.755
2016_0211_02:46:25.604	2016_0211_02:46:54.984	2016_0211_02:46:40.094
2016_0211_02:46:53.685	2016_0211_02:47: 5.477	2016_0211_02:46:59.381
2016_0214_03:04:15.665	2016_0214_03:04:47.033	2016_0214_03:04:28.518
2016_0215_00:40:42.597	2016_0215_00:41: 0.198	2016_0215_00:40:49.397
2016_0215_01:28:58.021	2016_0215_01:29:52.260	2016_0215_01:29:32.137
2016_0215_02:23: 0.402	2016_0215_02:24:12.632	2016_0215_02:23:30.786
2016_0215_19:14:37.162	2016_0215_19:14:57.486	2016_0215_19:14:46.525
2016_0221_21:11:12.871	2016_0221_21:11:50.860	2016_0221_21:11:32.206

2016_0226_02:29: 1.309   2016_0226_02:29:45.405   2016_0226_02:29:25.642

Bibliography

Abel, I. G., Barnes, M., Cowley, S. C., Dorland, W., & Schekochihin, A. A. 2008, Physics of Plasmas, 15, 122509, doi: 10.1063/1.3046067

Alexandrova, O., Lacombe, C., & Mangeney, A. 2008, Annales Geophysicae, doi: 10.5194/angeo-26-3585-2008

Alexandrova, O., Saur, J., Lacombe, C., et al. 2009, Physical Review Letters, 103, 165003, doi: 10.1103/physrevlett.103.165003

Ballegooijen, A. A. v., Asgari-Targhi, M., & Berger, M. A. 2014, The Astrophysical Journal, 787, 87, doi: 10.1088/0004-637x/787/1/87

Barnes, M., Abel, I. G., Dorland, W., et al. 2009, Physics of Plasmas, 16, 072107, doi: 10.1063/1.3155085

Bessho, N., Chen, L., Shuster, J. R., & Wang, S. 2014, Geophysical Research Letters, 41, 8688, doi: 10.1002/2014gl062034

Bessho, N., Chen, L. J., Wang, S., & Hesse, M. 2019, Physics of Plasmas, 26, 082310, doi: 10.1063/1.5092809

Bessho, N., Chen, L.-J., Wang, S., et al. 2020, Physics of Plasmas, 27, 092901, doi: 10.1063/5.0012443

Birn, J., Drake, J. F., Shay, M. A., et al. 2001, Journal of Geophysical Research: Space Physics, 106, 3715, doi: 10.1029/1999ja900449

Bogdanova, Y. V., Owen, C. J., Dunlop, M. W., et al. 2008, Journal of Geophysical Research: Space Physics, 113, n/a, doi: 10.1029/2007ja012762

Boldyrev, S., & Loureiro, N. F. 2017, The Astrophysical Journal, 844, 125, doi: 10.3847/1538-4357/aa7d02

Borovsky, J. E. 2008, Journal of Geophysical Research: Space Physics (1978–2012), 113, n/a, doi: 10.1029/2007ja012684

Broll, J. M., Fuselier, S. A., & Trattner, K. J. 2017, Journal of Geophysical Research: Space Physics, 122, 5105, doi: 10.1002/2016ja023590

Bruno, R., Carbone, V., Veltri, P., Pietropaolo, E., & Bavassano, B. 2001, Planetary and Space Science, 49, 1201, doi: 10.1016/s0032-0633(01)00061-7

Burch, J. L., Moore, T. E., Torbert, R. B., & Giles, B. L. 2015, Space Science Reviews, 199, 5, doi: 10.1007/s11214-015-0164-9

Burch, J. L., & Phan, T. D. 2016, Geophysical Research Letters, 43, 8327, doi: 10.1002/2016gl069787

Burch, J. L., Torbert, R. B., Phan, T. D., et al. 2016, Science, 352, aaf2939, doi: 10.1126/science.aaf2939

Burch, J. L., Ergun, R. E., Cassak, P. A., et al. 2018, Geophysical Research Letters, 45, 1237, doi: 10.1002/2017gl076809

Büchner, J., & Zelenyi, L. M. 1989, Journal of Geophysical Research: Space Physics, 94, 11821, doi: 10.1029/ja094ia09p11821

Cassak, P. A., & Shay, M. A. 2007, Physics of Plasmas, 14, 102114, doi: 10.1063/1.2795630

Chanteur, G. 1998, ISSI Scientific Reports Series, 1, 349

Chen, L., Hesse, M., Wang, S., Bessho, N., & Daughton, W. 2016, Geophysical Research Letters, 43, 2405, doi: 10.1002/2016gl068243

Chen, L., Hesse, M., Wang, S., et al. 2017, Journal of Geophysical Research: Space Physics, 122, 5235, doi: 10.1002/2017ja024004

Chen, L., Wang, S., Hesse, M., et al. 2019, Geophysical Research Letters, 46, 6230, doi: 10.1029/2019gl082393

Chen, L.-J., Wang, S., Contel, O. L., et al. 2020, Physical Review Letters, 125, 025103, doi: 10.1103/physrevlett.125.025103

Cho, J., & Lazarian, A. 2004, The Astrophysical Journal, 615, L41, doi: 10.1086/425215

Cowley, S. W. H. 1982, Reviews of Geophysics, 20, 531, doi: 10.1029/rg020i003p00531

Cranmer, S. R., & Winebarger, A. R. 2019, Annual Review of Astronomy and Astrophysics, 57, 157, doi: 10.1146/annurev-astro-091918-104416

Dahlburg, R. B., & Picone, J. M. 1989, Physics of Fluids B: Plasma Physics, 1, 2153, doi: 10.1063/1.859081

Dmitruk, P., Matthaeus, W. H., & Seenu, N. 2004, The Astrophysical Journal, 617, 667, doi: 10.1086/425301

Dorelli, J. C., & Bhattacharjee, A. 2009, Journal of Geophysical Research: Space Physics (1978–2012), 114, n/a, doi: 10.1029/2008ja013410

Dorfman, S., Ji, H., Yamada, M., et al. 2013, Geophysical Research Letters, 40, 233, doi: 10.1029/2012gl054574

Dungey, J. W. 1961, Physical Review Letters, 6, 47, doi: 10.1103/physrevlett.6.47

Eastwood, J. P., Lucek, E. A., Mazelle, C., et al. 2005, Space Science Reviews, 118, 41, doi: 10.1007/s11214-005-3824-3

Egedal, J., Le, A., Daughton, W., et al. 2016, Physical Review Letters, 117, 185101, doi: 10.1103/physrevlett.117.185101

Eriksson, E., Vaivads, A., Graham, D. B., et al. 2018, Geophysical Research Letters, 45, 8081, doi: 10.1029/2018gl078660

Fargette, N., Lavraud, B., Øieroset, M., et al. 2020a, Geophysical Research Letters, doi: 10.1029/2019gl086726

Fargette, N., Lavraud, B., Rouillard, A., et al. 2020b, Astronomy & Astrophysics, doi: 10.1051/0004-6361/202039191

Farrugia, C. J., Chen, L., Torbert, R. B., et al. 2011, Journal of Geophysical Research: Space Physics (1978–2012), 116, n/a, doi: 10.1029/2010ja015495

Fear, R. C., Milan, S. E., Fazakerley, A. N., et al. 2008, Annales Geophysicae, 26, 2353, doi: 10.5194/angeo-26-2353-2008

Fedder, J. A., Slinker, S. P., Lyon, J. G., & Russell, C. T. 2002, Journal of Geophysical Research: Space Physics (1978–2012), 107, SMP 1, doi: 10.1029/2001ja000025

Franci, L., Cerri, S. S., Califano, F., et al. 2017, The Astrophysical Journal, 850, L16, doi: 10.3847/2041-8213/aa93fb

Frazier, E. N., & Stenflo, J. O. 1972, Solar Physics, 27, 330, doi: 10.1007/bf00153105

Freed, A. J., & Russell, C. T. 2014, Geophysical Research Letters, 41, 6590, doi: 10.1002/2014gl061353

Frieman, E. A., & Chen, L. 1982, Physics of Fluids (1958-1988), 25, 502, doi: 10.1063/1.863762

Fuselier, S. A., Lewis, W. S., Schiff, C., et al. 2016, Space Science Reviews, 199, 77, doi: 10.1007/s11214-014-0087-x

Genestreti, K. J., Phan, T. D., Denton, R. E., et al. 2020, arXiv

Gingell, I., Schwartz, S. J., Eastwood, J. P., et al. 2019, Geophysical Research Letters, 46, 1177, doi: 10.1029/2018gl081804

—. 2020, Journal of Geophysical Research: Space Physics, 125, doi: 10.1029/2019ja027119

Graham, D. B., Khotyaintsev, Y. V., Vaivads, A., & André, M. 2016, Journal of Geophysical Research: Space Physics, 121, 3069, doi: 10.1002/2015ja021527

Grauer, R., & Marliani, C. 2000, Physical Review Letters, 84, 4850, doi: 10.1103/physrevlett.84.4850

Haggerty, C. C., Parashar, T. N., Matthaeus, W. H., et al. 2017, Physics of Plasmas, 24, 102308, doi: 10.1063/1.5001722

Haggerty, C. C., Shay, M. A., Chasapis, A., et al. 2018, Physics of Plasmas, 25, 102120, doi: 10.1063/1.5050530

Hasegawa, H., Denton, R., Genestreti, K., et al. 2020, doi: 10.21203/rs.3.rs-40743/v1

Hesse, M., Birn, J., & Schindler, K. 1990, Journal of Geophysical Research, 95, 6549, doi: 10.1029/ja095ia05p06549

Hesse, M., & Cassak, P. A. 2020, Journal of Geophysical Research: Space Physics, 125, doi: 10.1029/2018ja025935

Hesse, M., Liu, Y., Chen, L., et al. 2016, Geophysical Research Letters, 43, 2359, doi: 10.1002/2016gl068373

Hesse, M., & Winske, D. 1993, Geophysical Research Letters, 20, 1207, doi: 10.1029/93gl01250

Howes, G. G. 2016, The Astrophysical Journal, 827, L28, doi: 10.3847/2041-8205/827/2/l28

Howes, G. G., Cowley, S. C., Dorland, W., et al. 2006, The Astrophysical Journal, 651, 590, doi: 10.1086/506172

Howes, G. G., Dorland, W., Cowley, S. C., et al. 2008, Physical Review Letters, 100, 065004, doi: 10.1103/physrevlett.100.065004

Howes, G. G., McCubbin, A. J., & Klein, K. G. 2018, Journal of Plasma Physics, 84, 905840105, doi: 10.1017/s0022377818000053

134

Howes, G. G., TenBarge, J. M., Dorland, W., et al. 2011, Physical Review Letters, 107, 035004, doi: 10.1103/physrevlett.107.035004

Huang, K., Liu, Y., Lu, Q., & Hesse, M. 2020, Geophysical Research Letters, 47, doi: 10.1029/2020gl088147

Hubbert, M., Qi, Y., Russell, C., et al. 2021, Geophysical Research Letters, doi: 10.1029/2020gl091364

Hudson, P. 1970, Planetary and Space Science, 18, 1611, doi: 10.1016/0032-0633(70)90036-x

Hwang, K. J., Choi, E., Dokgo, K., et al. 2019, Geophysical Research Letters, 46, 6287, doi: 10.1029/2019gl082710

Hwang, K. J., Dokgo, K., Choi, E., et al. 2020, Journal of Geophysical Research: Space Physics, 125, doi: 10.1029/2019ja027665

Illing, R. M. E., & Hundhausen, A. J. 1985, Journal of Geophysical Research: Space Physics, 90, 275, doi: 10.1029/ja090ia01p00275

Imada, S., Nakamura, R., Daly, P. W., et al. 2007, Journal of Geophysical Research: Space Physics (1978–2012), 112, n/a, doi: 10.1029/2006ja011847

Imber, S. M., Slavin, J. A., Boardsen, S. A., et al. 2014, Journal of Geophysical Research: Space Physics, 119, 5613, doi: 10.1002/2014ja019884

Ji, H., Yamada, M., Hsu, S., & Kulsrud, R. 1998, Physical Review Letters, 80, 3256, doi: 10.1103/physrevlett.80.3256

Jia, Y., Combi, M. R., Hansen, K. C., & Gombosi, T. I. 2007, Journal of Geophysical Research: Space Physics (1978–2012), 112, n/a, doi: 10.1029/2006ja012175

Jia, Y., Qi, Y., Lu, S., & Russell, C. T. 2021, Journal of Geophysical Research: Space Physics, doi: 10.1029/2020ja028698

135

Jokipii, J. R., & Parker, E. N. 1968, Physical Review Letters, 21, 44, doi: 10.1103/physrevlett.21.44

Kacem, I., Jacquey, C., Génot, V., et al. 2018, Journal of Geophysical Research: Space Physics, 123, 1779, doi: 10.1002/2017ja024537

Kan, J. R. 1988, Journal of Geophysical Research, 93, 5613, doi: 10.1029/ja093ia06p05613

Karimabadi, H., Roytershteyn, V., Wan, M., et al. 2013, Physics of Plasmas, 20, 012303, doi: 10.1063/1.4773205

Keppens, R., Guo, Y., Makwana, K., et al. 2019, Reviews of Modern Plasma Physics, 3, 14, doi: 10.1007/s41614-019-0035-z

Khotyaintsev, Y. V., Cully, C. M., Vaivads, A., André, M., & Owen, C. J. 2010, Physical Review Letters, 106, 165001, doi: 10.1103/physrevlett.106.165001

Khotyaintsev, Y. V., Graham, D. B., Norgren, C., et al. 2016, Geophysical Research Letters, 43, 5571, doi: 10.1002/2016gl069064

Kieokaew, R., Lavraud, B., Foullon, C., et al. 2020, Journal of Geophysical Research: Space Physics, 125, doi: 10.1029/2019ja027527

King, J. H., & Papitashvili, N. E. 2005, Journal of Geophysical Research, 110, doi: 10.1029/2004ja010649

Kivelson, M. G., & Russell, C. T. 1995, Introduction to Space Physics

Kobayashi, S., Rogers, B. N., & Numata, R. 2014, Physics of Plasmas, 21, 040704, doi: 10.1063/1.4873703

Lapenta, G., Berchem, J., Zhou, M., et al. 2017, Journal of Geophysical Research: Space Physics, 122, 2024

Lau, Y.-T., & Finn, J. M. 1990, The Astrophysical Journal, 350, 672, doi: 10.1086/168419

Lavraud, B., Zhang, Y. C., Vernisse, Y., et al. 2016, Geophysical Research Letters, 43, 3042, doi: 10.1002/2016gl068359

Le, A., Egedal, J., Ohia, O., et al. 2013, Physical Review Letters, 110, 135004, doi: 10.1103/physrevlett.110.135004

Lee, L. C., & Fu, Z. F. 1985, Geophysical Research Letters, 12, 105, doi: 10.1029/gl012i002p00105

Lee, L. C., Ma, Z. W., Fu, Z. F., & Otto, A. 1993, Journal of Geophysical Research: Space Physics, 98, 3943, doi: 10.1029/92ja02203

Levy, R. H., Petschek, H. E., & Siscoe, G. L. 2012, AIAA Journal, 2, 2065, doi: 10.2514/3.2745

Li, T. C., Howes, G. G., Klein, K. G., Liu, Y.-H., & TenBarge, J. M. 2019, Journal of Plasma Physics, 85, 905850406, doi: 10.1017/s0022377819000515

Li, T. C., Howes, G. G., Klein, K. G., & TenBarge, J. M. 2016, The Astrophysical Journal, 832, L24, doi: 10.3847/2041-8205/832/2/l24

Li, T. C., Liu, Y., Hesse, M., & Zou, Y. 2020, Journal of Geophysical Research: Space Physics, 125, doi: 10.1029/2019ja027094

Li, T. C., Liu, Y.-H., & Qi, Y. 2021, The Astrophysical Journal Letters, 909, L28, doi: 10.3847/2041-8213/abea0b

Linton, M. G., Dahlburg, R. B., & Antiochos, S. K. 2001, The Astrophysical Journal, 553, 905, doi: 10.1086/320974

Liu, C. M., Fu, H. S., Liu, Y. Y., et al. 2020, Journal of Geophysical Research: Space Physics, 125, doi: 10.1029/2020ja027777

Liu, Y., Li, T. C., Hesse, M., et al. 2019, Journal of Geophysical Research: Space Physics, 124, 2819, doi: 10.1029/2019ja026539

Liu, Y.-H., Drake, J. F., & Swisdak, M. 2012, Physics of Plasmas, 19, 022110, doi: 10.1063/1.3685755

Liu, Y.-H., & Hesse, M. 2016, Physics of Plasmas (1994-present), 23, 060704, doi: 10.1063/1.4954818

Liu, Y.-H., Hesse, M., Guo, F., Li, H., & Nakamura, T. K. M. 2018, Physics of Plasmas, 25, 080701, doi: 10.1063/1.5042539

Liu, Z. X., & Hu, Y. D. 1988, Geophysical Research Letters, 15, 752, doi: 10.1029/gl015i008p00752

Loureiro, N. F., & Boldyrev, S. 2017, The Astrophysical Journal, 850, 182, doi: 10.3847/1538-4357/aa9754

Lu, S., Angelopoulos, V., Artemyev, A. V., et al. 2020a, The Astrophysical Journal, 900, 145, doi: 10.3847/1538-4357/abaa44

Lu, S., Wang, R., Lu, Q., et al. 2020b, Nature Communications, 11, 5049, doi: 10.1038/s41467-020-18787-w

Lundquist, S. 1950, Ark. Fys., 2, 361. https://ci.nii.ac.jp/naid/10003639556/en/

Lv, L., Pu, Z., & Xie, L. 2016, Science China Technological Sciences, 59, 1283, doi: 10.1007/s11431-016-6071-9

Lyatsky, W., & Goldstein, M. L. 2013, Nonlinear Processes in Geophysics, 20, 365, doi: 10.5194/npg-20-365-2013

Lyons, L. R., & Pridmore-Brown, D. C. 1990, Journal of Geophysical Research: Space Physics (1978–2012), 95, 20903, doi: 10.1029/ja095ia12p20903

Mallet, A., Schekochihin, A. A., & Chandran, B. D. G. 2017, Journal of Plasma Physics, 83, 905830609, doi: 10.1017/s0022377817000812

Marcowith, A., Ferrand, G., Grech, M., et al. 2020, Living Reviews in Computational Astrophysics, 6, 1, doi: 10.1007/s41115-020-0007-6

Markovskii, S. A., & Vasquez, B. J. 2011, The Astrophysical Journal, 739, 22, doi: 10.1088/0004-637x/739/1/22

Mininni, P. D., Pouquet, A. G., & Montgomery, D. C. 2006, Physical Review Letters, 97, 244503, doi: 10.1103/physrevlett.97.244503

Moore, T. E., Burch, J. L., Daughton, W. S., et al. 2013, Journal of Atmospheric and Solar-Terrestrial Physics, 99, 32, doi: 10.1016/j.jastp.2012.10.004

Ng, J., Egedal, J., Le, A., Daughton, W., & Chen, L.-J. 2011, Physical Review Letters, 106, 065002, doi: 10.1103/physrevlett.106.065002

Nielson, K. D., Howes, G. G., & Dorland, W. 2013, Physics of Plasmas, 20, 072303, doi: 10.1063/1.4812807

Nishida, A. 1989, Geophysical Research Letters, 16, 227, doi: 10.1029/gl016i003p00227

Nishida, H., Ogawa, H., & Inatani, Y. 2009, 765, doi: 10.1007/978-3-540-92779-2_120

Numata, R., Dorland, W., Howes, G. G., et al. 2011, Physics of Plasmas, 18, 112106, doi: 10.1063/1.3659035

Numata, R., Howes, G. G., Tatsuno, T., Barnes, M., & Dorland, W. 2010, Journal of Computational Physics, 229, 9347, doi: 10.1016/j.jcp.2010.09.006

Numata, R., & Loureiro, N. F. 2015, Journal of Plasma Physics, 81, 305810201, doi: 10.1017/s002237781400107x

Osman, K. T., Matthaeus, W. H., Greco, A., & Servidio, S. 2011, The Astrophysical Journal Letters, 727, L11, doi: 10.1088/2041-8205/727/1/l11

Osman, K. T., Matthaeus, W. H., Wan, M., & Rappazzo, A. F. 2012, Physical Review Letters, 108, 261102, doi: 10.1103/physrevlett.108.261102

Otto, A. 1991, Geophysical & Astrophysical Fluid Dynamics, 62, 69, doi: 10.1080/03091929108229126

Parashar, T. N., Shay, M. A., Cassak, P. A., & Matthaeus, W. H. 2009, Physics of Plasmas, 16, 032310, doi: 10.1063/1.3094062

Parashar, T. N., Vasquez, B. J., & Markovskii, S. A. 2014, Physics of Plasmas, 21, 022301, doi: 10.1063/1.4863422

Parker, E. N. 1957, Journal of Geophysical Research, 62, 509, doi: 10.1029/jz062i004p00509

Paschmann, G., Papamastorakis, I., Baumjohann, W., et al. 1986, Journal of Geophysical Research: Space Physics, 91, 11099, doi: 10.1029/ja091ia10p11099

Paschmann, G., Øieroset, M., & Phan, T. 2013, Space Science Reviews, 178, 385, doi: 10.1007/s11214-012-9957-2

Perri, S., Goldstein, M. L., Dorelli, J. C., & Sahraoui, F. 2012, Physical Review Letters, 109, 191101, doi: 10.1103/physrevlett.109.191101

Petschek, H. E. 1964, The Physics of Solar Flares, Proceedings of the AAS-NASA Symposium held 28-30 October, 1963 at the Goddard Space Flight Center, Greenbelt, MD. Edited by Wilmot N. Hess. Washington, DC: National Aeronautics and Space Administration, Science and Technical Information Division, 1964., p.425

Phan, T., Paschmann, G., & Sonnerup, B. U. O. 1996

Phan, T. D., Paschmann, G., Gosling, J. T., et al. 2013, Geophysical Research Letters, 40, 11, doi: 10.1029/2012gl054528

Phan, T. D., Kistler, L. M., Klecker, B., et al. 2000, Nature, 404, 848, doi: 10.1038/35009050

Phan, T. D., Gosling, J. T., Paschmann, G., et al. 2010, The Astrophysical Journal, 719, L199, doi: 10.1088/2041-8205/719/2/l199

Phan, T. D., Eastwood, J. P., Shay, M. A., et al. 2018, Nature, 557, 202, doi: 10.1038/s41586-018-0091-5

Phan, T. D., Bale, S. D., Eastwood, J. P., et al. 2020, The Astrophysical Journal Supplement Series, 246, 34, doi: 10.3847/1538-4365/ab55ee

Picone, J. M., & Dahlburg, R. B. 1991, Physics of Fluids B: Plasma Physics, 3, 29, doi: 10.1063/1.859953

Politano, H., Pouquet, A., & Sulem, P. L. 1989, Physics of Fluids B: Plasma Physics, 1, 2330, doi: 10.1063/1.859051

—. 1995, Physics of Plasmas, 2, 2931, doi: 10.1063/1.871473

Pollock, C., Moore, T., Jacques, A., et al. 2016, Space Science Reviews, 199, 331, doi: 10.1007/s11214-016-0245-4

Pu, Z. Y., Raeder, J., Zhong, J., et al. 2013, Geophysical Research Letters, 40, 3502, doi: 10.1002/grl.50714

Pyakurel, P. S., Shay, M. A., Phan, T. D., et al. 2019, Physics of Plasmas, 26, 082307, doi: 10.1063/1.5090403

Qi, Y., Russell, C. T., Jia, Y., & Hubbert, M. 2020, Geophysical Research Letters, 47, doi: 10.1029/2020gl090314

Raeder, J. 2006, Annales Geophysicae, 24, 381, doi: 10.5194/angeo-24-381-2006

Retinò, A., Sundkvist, D., Vaivads, A., et al. 2007, Nature Physics, 3, 235, doi: 10.1038/nphys574

Richardson, I. G. 2004, Space Science Reviews, 111, 267, doi: 10.1023/b:spac.0000032689.52830.3e

Rogers, A. J., Farrugia, C. J., & Torbert, R. B. 2019, Journal of Geophysical Research: Space Physics, 124, 6487, doi: 10.1029/2018ja026429

Russell, C. 2000, IEEE Transactions on Plasma Science, 28, 1818, doi: 10.1109/27.902211

Russell, C., Luhmann, J., & Strangeway, R. 2016, Space Physics: An Introduction (Cambridge University Press). https://books.google.com/books?id=0-C_sgEACAAJ

Russell, C. T., & Elphic, R. C. 1978, Space Science Reviews, 22, 681, doi: 10.1007/bf00212619

—. 1979, Geophysical Research Letters, 6, 33, doi: 10.1029/gl006i001p00033

Russell, C. T., Mellott, M. M., Smith, E. J., & King, J. H. 1983, Journal of Geophysical Research, 88, 4739, doi: 10.1029/ja088ia06p04739

Russell, C. T., & Qi, Y. 2020, Geophysical Research Letters, doi: 10.1029/2020gl087620

Russell, C. T., Anderson, B. J., Baumjohann, W., et al. 2014, Space Science Reviews, 199, 189, doi: 10.1007/s11214-014-0057-3

Russell, C. T., Strangeway, R. J., Zhao, C., et al. 2017, Science, 356, 960, doi: 10.1126/science.aag3112

Sahraoui, F., Huang, S. Y., Patoul, J. D., et al. 2013, The Astrophysical Journal, 777, 15, doi: 10.1088/0004-637x/777/1/15

Schekochihin, A. A., Cowley, S. C., Dorland, W., et al. 2009, The Astrophysical Journal Supplement Series, 182, 310, doi: 10.1088/0067-0049/182/1/310

Scholer, M. 1988, Geophysical Research Letters, 15, 291, doi: 10.1029/gl015i004p00291

Scurry, L., Russell, C. T., & Gosling, J. T. 1994, Journal of Geophysical Research: Space Physics, 99, 14811, doi: 10.1029/94ja00794

Servidio, S., Matthaeus, W. H., Shay, M. A., Cassak, P. A., & Dmitruk, P. 2008, Physical Review Letters, 102, 115003, doi: 10.1103/physrevlett.102.115003

Servidio, S., Matthaeus, W. H., Shay, M. A., et al. 2010, Physics of Plasmas, 17, 032315, doi: 10.1063/1.3368798

Shay, M. A., Haggerty, C. C., Matthaeus, W. H., et al. 2018, Physics of Plasmas, 25, 012304, doi: 10.1063/1.4993423

Shay, M. A., Phan, T. D., Haggerty, C. C., et al. 2016, Geophysical Research Letters, 43, 4145, doi: 10.1002/2016gl069034

Smartt, R. N., Zhang, Z., & Smutko, M. F. 1993, Solar Physics, 148, 139, doi: 10.1007/bf00675540

Smith, E. J. 2001, Journal of Geophysical Research: Space Physics, 106, 15819, doi: 10.1029/2000ja000120

Sonnerup, B. U. Ö. 1979, Magnetic field reconnection, Vol. 3, 45–108

Sonnerup, B. U. O., & Cahill, L. J. 1967, Journal of Geophysical Research, 72, 171, doi: 10.1029/jz072i001p00171

Southwood, D. J., Farrugia, C. J., & Saunders, M. A. 1988, Planetary and Space Science, 36, 503, doi: 10.1016/0032-0633(88)90109-2

Stawarz, J. E., Eastwood, J. P., Phan, T. D., et al. 2019, The Astrophysical Journal, 877, L37, doi: 10.3847/2041-8213/ab21c8

Sundkvist, D., Retinò, A., Vaivads, A., & Bale, S. D. 2007, Physical Review Letters, 99, 025004, doi: 10.1103/physrevlett.99.025004

Sweet, P. A. 1958, Symposium - International Astronomical Union, 6, 123, doi: 10.1017/s0074180900237704

Tan, B., Lin, Y., Perez, J. D., & Wang, X. Y. 2011, Journal of Geophysical Research: Space Physics (1978–2012), 116, n/a, doi: 10.1029/2010ja015580

Tang, B. B., Li, W. Y., Graham, D. B., et al. 2019, Geophysical Research Letters, 46, 3024, doi: 10.1029/2019gl082231

Tatsuno, T., Dorland, W., Schekochihin, A. A., et al. 2009, Physical Review Letters, 103, 015003, doi: 10.1103/physrevlett.103.015003

TenBarge, J. M., Daughton, W., Karimabadi, H., Howes, G. G., & Dorland, W. 2014, Physics of Plasmas, 21, 020708, doi: 10.1063/1.4867068

TenBarge, J. M., & Howes, G. G. 2012, Physics of Plasmas, 19, 055901, doi: 10.1063/1.3693974

—. 2013, The Astrophysical Journal Letters, 771, L27, doi: 10.1088/2041-8205/771/2/l27

TenBarge, J. M., Howes, G. G., & Dorland, W. 2013, The Astrophysical Journal, 774, 139, doi: 10.1088/0004-637x/774/2/139

Torbert, R. B., Burch, J. L., Phan, T. D., et al. 2018, Science, 362, eaat2998, doi: 10.1126/science.aat2998

Trenchi, L., Coxon, J. C., Fear, R. C., et al. 2019, Journal of Geophysical Research: Space Physics, 124, 8600, doi: 10.1029/2018ja026126

Treumann, R., Jaroschek, C., Nakamura, R., Runov, A., & Scholer, M. 2006, Advances in Space Research, 38, 101, doi: 10.1016/j.asr.2004.11.045

Treumann, R. A., & Baumjohann, W. 2013, Frontiers in Physics, 1, 31, doi: 10.3389/fphy.2013.00031

Tóth, G., Ma, Y., & Gombosi, T. I. 2008, Journal of Computational Physics, 227, 6967, doi: 10.1016/j.jcp.2008.04.010

Tóth, G., Holst, B. v. d., Sokolov, I. V., et al. 2012, Journal of Computational Physics, 231, 870, doi: 10.1016/j.jcp.2011.02.006

Török, T., & Kliem, B. 2005, The Astrophysical Journal, 630, L97, doi: 10.1086/462412

Vasyliunas, V. M. 1975, Reviews of Geophysics, 13, 303, doi: 10.1029/rg013i001p00303

Vech, D., Mallet, A., Klein, K. G., & Kasper, J. C. 2018, The Astrophysical Journal, 855, L27, doi: 10.3847/2041-8213/aab351

Verscharen, D., Wicks, R. T., Alexandrova, O., et al. 2021, Experimental Astronomy, 1, doi: 10.1007/s10686-021-09761-5

Vörös, Z., Yordanova, E., Varsani, A., et al. 2017, Journal of Geophysical Research: Space Physics, 122, 11,442, doi: 10.1002/2017ja024535

Walsh, B. M. 2017, Geophysical Monograph Series, 29, doi: 10.1002/9781119216346.ch3

Wan, M., Matthaeus, W. H., Servidio, S., & Oughton, S. 2013, Physics of Plasmas, 20, 042307, doi: 10.1063/1.4802985

Wan, M., Matthaeus, W. H., Karimabadi, H., et al. 2012, Physical Review Letters, 109, 195001, doi: 10.1103/physrevlett.109.195001

Wang, R., Lu, Q., Nakamura, R., et al. 2018, Geophysical Research Letters, 45, 4542, doi: 10.1002/2017gl076330

Wang, S., Chen, L., Bessho, N., et al. 2019, Geophysical Research Letters, 46, 562, doi: 10.1029/2018gl080944

Webb, D. F., & Howard, T. A. 2012, Living Reviews in Solar Physics, 9, 3, doi: 10.12942/lrsp-2012-3

Webster, J. M., Burch, J. L., Reiff, P. H., et al. 2018, Journal of Geophysical Research: Space Physics, 123, 4858, doi: 10.1029/2018ja025245

Wilder, F. D., Ergun, R. E., Burch, J. L., et al. 2018, Journal of Geophysical Research: Space Physics, 123, 6533, doi: 10.1029/2018ja025529

Wu, P., Perri, S., Osman, K., et al. 2013, The Astrophysical Journal, 763, L30, doi: 10.1088/2041-8205/763/2/l30

Xue, Z., Yan, X., Cheng, X., et al. 2016, Nature Communications, 7, 11837, doi: 10.1038/ncomms11837

Yamada, M., Ono, Y., Hayakawa, A., Katsurai, M., & Perkins, F. W. 1990, Physical Review Letters, 65, 721, doi: 10.1103/physrevlett.65.721

Yordanova, E., Vörös, Z., Varsani, A., et al. 2016, Geophysical Research Letters, 43, 5969, doi: 10.1002/2016gl069191

Zenitani, S., Hesse, M., Klimas, A., & Kuznetsova, M. 2011, Physical Review Letters, 106, 195003, doi: 10.1103/physrevlett.106.195003

Zhang, H., Kivelson, M. G., Angelopoulos, V., et al. 2011, Journal of Geophysical Research: Space Physics (1978–2012), 116, n/a, doi: 10.1029/2011ja016500

Zhao, C. 2019, PhD thesis, University of California Los Angeles

Zhdankin, V., Uzdensky, D. A., Perez, J. C., & Boldyrev, S. 2013, The Astrophysical Journal, 771, 124, doi: 10.1088/0004-637x/771/2/124

Zhou, M., Berchem, J., Walker, R. J., et al. 2017, Physical Review Letters, 119, 055101, doi: 10.1103/physrevlett.119.055101

Zhou, M., Deng, X. H., Zhong, Z. H., et al. 2019, The Astrophysical Journal, 870, 34, doi: 10.3847/1538-4357/aaf16f

Zurbuchen, T. H., & Richardson, I. G. 2005, Space Sciences Series of ISSI, 31, doi: 10.1007/978-0-387-45088-9_3

Øieroset, M., Lin, R. P., Phan, T. D., Larson, D. E., & Bale, S. D. 2002, Physical Review Letters, 89, 195001, doi: 10.1103/physrevlett.89.195001

Øieroset, M., Phan, T. D., Haggerty, C., et al. 2016, Geophysical Research Letters, 43, 5536, doi: 10.1002/2016gl069166

Øieroset, M., Phan, T. D., Drake, J. F., et al. 2019, Geophysical Research Letters, 46, 1937, doi: 10.1029/2018gl080994